Non–Gaussian information in Cosmology with Weak Gravitational Lensing

Andrea Petri

Submitted in partial fulfillment of the
requirements for the degree
of Doctor of Philosophy
in the Graduate School of Arts and Sciences

COLUMBIA UNIVERSITY

2017

©2017
Andrea Petri
All Rights Reserved

Abstract

Non–Gaussian information in Cosmology with Weak Gravitational Lensing

Andrea Petri

The Standard Model of cosmology successfully describes the observable Universe requiring only a small number of free parameters. The model has been validated by a wide range of observable probes such as Supernovae IA, the CMB, Baryonic Acoustic Oscillations and galaxy clusters. Weak Gravitational Lensing (WL) is becoming a popular observational technique to constrain parameters in the Standard Model and is particularly appealing to the scientific community because the tracers it relies on, image distortions, are unbiased probes of density fluctuations in the fabric of the cosmos. The WL effect is sensitive to the late time evolution of the Universe, in which structures are non–linear. Because of this, WL observations cannot be treated as Gaussian random fields and statistical information on cosmology leaks from quadratic correlations into more complicated, higher order, image features. The goal of this dissertation is to analyze the efficiency of some of these higher order features in constraining Standard Model parameters. We approach the investigation

from a practical point of view, examining the analytical, computational and numerical accuracy issues that are involved in carrying a complete analysis from observational data to parameter constraints using these higher order statistics. This work is organized as follows:

- In Chapter 1 we review the fundamentals of the ΛCDM Standard Model of cosmology, focusing particularly on the Friedmann picture and on the physics of large scale density fluctuations.

- In Chapter 2 we give an outline of the Gravitational Lensing effect in the context of cosmology, and we introduce the basic WL observables from an analytical point of view.

- In Chapter 3 we review the relevant numerical techniques used in the modeling of WL observables, focusing in particular on the algorithms used in ray–tracing simulations. These simulations constitute the base of our modeling efforts.

- In Chapter 4 we discuss feature extraction techniques from WL observations: we treat both quadratic statistics, such as the angular shear–shear power spectrum, and higher order statistics for which analytical treatment is not possible.

- In Chapter 5 we review the Bayesian formalism behind the inference of ΛCDM parameters from image features. We place particular emphasis on physical and numerical effects that degrade parameter constraints and discuss possible mitigations.

- In Chapter 6 we apply the previously described techniques to the Canada France Hawaii LenS galaxy survey, showing how the use of higher order image statistics can improve inferences on the ΛCDM parameters that describe density fluctuations.

- In Chapter 7 we discuss some of the issues that arise in the analysis of a large scale WL survey such as the Large Scale Synoptic Survey: we focus on systematic effects caused by sensors imperfections, the atmosphere, redshift errors and approximate theoretical modeling.
- In Chapter 8 we draw our conclusions and discuss possible future developments.

Contents

List of symbols and abbreviations **iv**

1 The ΛCDM cosmological model **1**

1.1 The Friedmann-Robertson-Walker model 1

1.2 Matter density perturbations 7

1.3 ΛCDM cosmological parameters 15

2 Gravitational Lensing **20**

2.1 Light ray geodesics 20

2.2 Weak Gravitational Lensing 25

3 Numerical Weak Lensing **36**

3.1 Cosmological simulations 36

3.2 The multi–lens–plane algorithm 41

3.3 Approximate methods 50

3.4 The `LensTools` software package 53

4 Shear image features **57**

4.1 Local expectation values in real space 58

4.2 Minkowski Functionals . . . 61
4.3 Peak counts . . . 70
4.4 Angular power spectrum . . . 72
4.5 Convergence moments . . . 79
4.6 Summary . . . 83

5 Cosmological parameter inference **85**
5.1 Bayesian formalism . . . 85
5.2 Error degradation induced by noise in the covariance matrix . . . 90
5.3 Pseudo–independence of realizations . . . 99
5.4 Dimensionality reduction . . . 103
5.5 Constraints from Weak Lensing . . . 108

6 An application to data: the CFHTLenS galaxy survey **109**
6.1 CFHTLenS catalogs . . . 109
6.2 Emulator . . . 111
6.3 Parameter inference . . . 117

7 Applications to the LSST survey: systematic challenges **126**
7.1 Atmospheric/PSF spurious shear . . . 127
7.2 CCD sensor effects . . . 134
7.3 Photometric redshift errors . . . 138
7.4 Born approximation . . . 143
7.5 Other systematic effects . . . 146

8 Conclusions **149**

8.1 Overview of the results 149
8.2 Future prospects 152

Bibliography **155**

Appendix **163**

List of symbols and abbreviations

$\mathbf{A}$	Lensing Jacobian
$\mathbf{C}, \mathbf{\Psi}$	Feature–feature covariance matrix and its inverse
$\mathbf{F}$	Fisher information matrix
$\mathbf{T}^{\Phi}$	Tidal tensor $\nabla_{\perp}\nabla_{\perp}^{T}\Phi$
χ	Longitudinal comoving distance
δ	Cold Matter density contrast
δ^{D}	Dirac delta function
δ_{ij}	Kronecker delta symbol
$\dot{f}$	Time derivative of f
γ^{i}	i-th component of WL shear
$\hat{x}$	Estimator of a quantity x
κ	WL convergence
$\langle\hat{x}\rangle$	Expectation value of $\hat{x}$
$\mathcal{L}(a\|b)$	Likelihood of a given prior information b
$\mathcal{N}(\boldsymbol{\mu}, \mathbf{C})$	Normal distribution with mean $\boldsymbol{\mu}$ and covariance $\mathbf{C}$
$\mathbb{1}_{n\times n}$	$n \times n$ identity matrix
∇	Spatial gradient
$\nabla_{\perp}$	Spatial transverse gradient

ω	WL rotation
Φ	Gravitational 3D lensing potential
$\boldsymbol{\varepsilon}$	Antisymmetric tensor $\varepsilon_{ij} = -\varepsilon_{ji}$, $\varepsilon_{xy} = 1$
$\boldsymbol{\theta}$	Earth observer angular coordinates
$\Re z, \Im z$	Real and imaginary parts of z
ρ_Λ	Dark Energy mass density
ρ_m	Cold Matter spatially averaged mass density
Θ	Step function, $\Theta(x) = 0$ for $x < 0$ and $\Theta(x) = 1$ for $x > 0$
$\tilde{f}(\mathbf{k})$	Spatial Fourier transform of f at wavevector $\mathbf{k}$
$\tilde{f}(\boldsymbol{\ell})$	Angular Fourier transform of f at multipole $\boldsymbol{\ell}$
$\mathrm{Tr}\mathbf{M}$	Trace of the square matrix $\mathbf{M}$
$\lvert\mathbf{M}\rvert$	Determinant of the square matrix $\mathbf{M}$
$\mathbf{x}_\perp$	Transverse comoving coordinate
a	Scale factor of the universe
c	Speed of light
G	Newton's gravitational constant
$g_{\mu\nu}$	Metric tensor
N_π	Dimensionality of the ΛCDM parameter sub–space
N_d	Dimensionality of the feature space
N_r	Number of pseudo-independent realizations of one WL field of view
N_s	Number of independent N–body simulations in one cosmology
P^μ	4–momentum
x^μ	Coordinate 4–vector
z^*	Complex conjugate of z

API Application Program Interface

CCD Charge–coupled device

CMB Cosmic Microwave Background

FFT Fast Fourier Transform

FRW Friedmann Robertson Walker

GL Gravitational Lensing

KS Kaiser–Squires

LHS Left hand side

MFs Minkowski functionals

ODE Ordinary Differential Equation

PCA Principal Component Analysis

PDF Probability Distribution Function

PN Post–Newtonian

PSF Point Spread Function

RHS Right hand side

SVD Singular Value Decomposition

WL Weak Lensing

"Viandante, il sentiero non è altro che le orme dei tuoi passi
Viandante, non c'è sentiero, il sentiero si apre camminando"

Antonio Machado, impresso sulla felpa della Compagnia Atacama

"Infinite possibilities in infinite combinations"

On the Kol-Ut-Shan donated to T'Pol from her mother T'Dal, Vulcan, 2154

Remember the Cant

Acknowledgments

At the end of this wonderful 6 years journey, during which I learned a lot, I want to thank my advisors Zoltán and Morgan for guiding me along the road. I also want to thank my fiancé Mary and my parents Marco and Eva for continued, invaluable and unconditioned support.

I deeply believe that science is a mean for peace, and I hope that looking at the stars will give us the inspiration we need to face the many challenges that lie ahead, today especially.

The Ancients launched the Destiny to investigate a coherent structure in the CMB, which they believed to be a hint of an intelligence greater than humans could comprehend. As Dr. Rush rightfully stated, "the mission was never about going home, but it's about getting us to where we're going".

That is
the mission.

Dedicated to all immigrants

Chapter 1

The ΛCDM cosmological model

In this Chapter we discuss the main features of the Standard Model of cosmology. We first approximate the Universe as a homogeneous and isotropic system, following the guidelines of the Friedmann model [1]. We then study the physics of the large scale density fluctuations that are present on top of the uniform background. We list and define the free parameters in the Standard Model.

1.1 The Friedmann-Robertson-Walker model

In the course of this work, we assume the Universe to be described by a flat Friedmann-Robertson-Walker (FRW) model with time dependent scale factor $a(t)$ and Hubble parameter $H(t) = \dot{a}(t)/a(t)$. We introduce comoving spatial coordinates $\mathbf{x}$, centered on an Earth–based observer, and we define a spacetime 4–vector $dx^\mu = (cdt, d\mathbf{x})$. We can define a 4–momentum associated with the x^μ coordinates as $P^\mu = dx^\mu/ds$, with $ds = cd\tau$ (this definition states that τ can be identified as proper time for massive particles. For the case of photons we identify τ as a geodesic line parameter). Assuming an homogeneous and

isotropic Universe, the line element can be written as

$$ds^2 = g_{\mu\nu} dx^\mu dx^\nu = -c^2 dt^2 + a(t)^2 d\mathbf{x}^2 \tag{1.1.1}$$

We introduced the diagonal metric tensor $g_{\mu\nu}$, defined as

$$g_{\mu\nu}(\mathbf{x}, t) = \begin{pmatrix} -1 & 0 & 0 & 0 \\ 0 & a(t)^2 & 0 & 0 \\ 0 & 0 & a(t)^2 & 0 \\ 0 & 0 & 0 & a(t)^2 \end{pmatrix} \tag{1.1.2}$$

In the remainder of the Chapter we will use the notation $g \equiv -|\mathbf{g}|$ and we will use the metric to raise and lower indexes, i.e. we define $V_\mu = g_{\mu\nu} V^\nu$ for a generic 4–vector V^μ. We also define $g^{\mu\nu} = (\mathbf{g}^{-1})_{\mu\nu}$. The contents of the FRW universe are assumed to be perfect fluids, described by spatially uniform mass densities $\rho_{(i)}$ and pressures $\mathcal{P}_{(i)}$. We consider the reference frame of a fundamental observer, in which the stress–energy tensor for species i assumes the form

$$\mathcal{T}^{\mu\nu}_{(i)} = \left(\rho_{(i)} c^2 + \mathcal{P}_{(i)}\right) U^\mu U^\nu + \mathcal{P}_{(i)} g^{\mu\nu} \tag{1.1.3}$$

Here U^μ is the 4–velocity of a fluid element centered at x^μ. Note that, for a fundamental observer, in absence of perturbations the fluid elements 4–velocity must be consistent with the homogeneity assumption

$$U^\mu = (1, 0, 0, 0) \tag{1.1.4}$$

Note also that the stress–energy tensor must obey the covariant conservation law

$$\nabla_\mu \mathcal{T}^{\mu\nu}_{(i)} = \partial_\mu \mathcal{T}^{\mu\nu}_{(i)} + \Gamma^\mu_{\mu\alpha}\mathcal{T}^{\alpha\nu}_{(i)} + \Gamma^\nu_{\mu\alpha}\mathcal{T}^{\mu\alpha}_{(i)} = 0 \tag{1.1.5}$$

The only non zero components of the affine connection Γ for the FRW metric (1.1.1) are

$$\Gamma^i_{j0} = \Gamma^0_{ij}a^2 = \frac{H}{c}\delta_{ij} \tag{1.1.6}$$

Combining (1.1.6) with (1.1.3), the 0–th component of the conservation condition (1.1.5) reads

$$\dot{\rho}_{(i)} + 3H\left(\rho_{(i)} + \mathcal{P}_{(i)}/c^2\right) = 0 \tag{1.1.7}$$

The metric $g_{\mu\nu}$ has to satisfy Einstein equation with source terms $\mathcal{T}_{\mu\nu}$

$$\mathcal{R}^{\mu\nu} - \frac{1}{2}\mathcal{R}g^{\mu\nu} = \frac{8\pi G}{c^4}\sum_i \mathcal{T}^{\mu\nu}_{(i)} \tag{1.1.8}$$

In (1.1.8) we indicated the Ricci tensor as $\mathcal{R}^{\mu\nu}$ and the Ricci scalar as $\mathcal{R} = g_{\mu\nu}\mathcal{R}^{\mu\nu}$. It can be shown (see for example [2]) that the components of the Ricci tensor for the metric (1.1.1) are

$$\mathcal{R}_{00} = -\frac{3\ddot{a}}{ac^2} \quad ; \quad \mathcal{R}_{ij} = \left(\frac{a\ddot{a} + 2a^2H^2}{c^2}\right)\delta_{ij} \quad ; \quad \mathcal{R} = \frac{6}{c^2}\left(\frac{\ddot{a}}{a} + H^2\right) \tag{1.1.9}$$

With the symmetries in the metric (1.1.1), the Einstein equations (1.1.8) have two independent components, which take the name of Friedmann equations

$$H^2 = \frac{8\pi G}{3} \sum_i \rho_{(i)} \tag{1.1.10}$$

$$\frac{\ddot{a}}{a} = -\frac{4\pi G}{3} \sum_i \left(\rho_{(i)} + \frac{3\mathcal{P}_{(i)}}{c^2} \right) \tag{1.1.11}$$

Once relations between the components pressures and densities are specified, the conservation equation (1.1.7) and the Friedmann equations (1.1.10), (1.1.11) can be solved explicitly to obtain the time dependencies of $a, \rho_{(i)}, \mathcal{P}_{(i)}$. Later in the Chapter, we will derive these solutions explicitly for the cases relevant to this work.

1.1.1 Distance-redshift relation

In this section we summarize the basics of the cosmological redshift effect, which is a direct consequence of the FRW geometry. Consider a source (for example a galaxy) at a comoving distance χ_s from the observer on Earth, which emits light at a frequency ν_s. Due to the expansion of the Universe, which is described by the scale factor a, the wavelength of the light gets stretched as photons travel from the source to the observer. Indicating the observed frequency on Earth as ν_0, we can define a redshift parameter associated with the source

$$z_s = \frac{\nu_s}{\nu_0} - 1 \tag{1.1.12}$$

It can be shown that there is a one–to–one correspondence between redshift and scale factor, defined by

$$z_s = \frac{1}{a(t_s)} - 1 \tag{1.1.13}$$

where t_s is the emission time of a photon that reaches Earth at the present time t_0, for which we assumed $a(t_0) = 1$. The FRW metric (1.1.1) establishes correspondences between the source redshift z_s, the photon emission time t_s and the source distance χ_s. Using the fact that $ds^2 = 0$ along a photon spacetime trajectory, we can write

$$\chi_s = -c \int_{t_0}^{t_s} \frac{dt}{a} = -c \int_{a(t_0)}^{a(t_s)} \frac{da}{a^2 H} \tag{1.1.14}$$

$$t_s = \int_0^{\chi_s} \frac{a d\chi}{c} = -\int_{a(t_0)}^{a(t_s)} \frac{da}{aH} \tag{1.1.15}$$

Note that, using (1.1.13), the relations (1.1.14), (1.1.15) can be rewritten as

$$\chi_s = c \int_0^{z_s} \frac{dz}{H(z)} \tag{1.1.16}$$

$$t_s = \int_0^{z_s} \frac{dz}{(1+z)H(z)} \tag{1.1.17}$$

In practical observations, source redshifts z_s are measured using photometric [3] or spectroscopic [4] techniques and χ_s, t_s are then inferred from equations (1.1.16), (1.1.17) with the help of Friedmann equation (1.1.10), which sets the time dependence of the Hubble parameter H. The late universe ($z \ll 3000$) is well described in terms of two components, namely cold matter and Dark Energy (hence the ΛCDM denomination), which effects we explore in the next sections.

1.1.2 Cold Dark Matter

In this work we model Dark Matter at late times as a non–relativistic species of particles with mass m. When the equilibrium temperature T is much smaller than mc^2/k_B, we can

neglect the pressure term in (1.1.7) and obtain a scaling relation for the dark matter mass density ρ_m with a

$$\rho_m(a) = \rho_m(a_0)\left(\frac{a(t_0)}{a}\right)^3 = \rho_m(a_0)(1+z)^3 \tag{1.1.18}$$

Substituting (1.1.18) in the Friedmann equation (1.1.10) we can get the time dependence of a for a pure Dark Matter Universe

$$a(t) = a(t_0)\left(\frac{t}{t_0}\right)^{2/3} \tag{1.1.19}$$

1.1.3 Dark energy

The existence of Dark Energy was postulated after observational evidence of the accelerated expansion of the Universe. Suppose that Dark Energy is described by a perfect fluid with density ρ_Λ and pressure $\mathcal{P}_\Lambda$ which are related by

$$\mathcal{P}_\Lambda = w\rho_\Lambda c^2 \tag{1.1.20}$$

w takes the name of Dark Energy *equation of state*. Looking at equation (1.1.11), we note that a necessary condition for Dark Energy to cause $\ddot{a} > 0$ is $w < -1/3$. Because of the challenges posed by modeling a fluid with negative w from first principles, Dark Energy is usually described by a phenomenological, a dependent, equation of state in the form

$$w(a) = w_0 + w_a(1-a) \tag{1.1.21}$$

with w_0, w_a constant [5]. With the assumption (1.1.21), the conservation equation (1.1.7) can be solved for the scale dependency of ρ_Λ

$$\rho_\Lambda(a) = \rho_\Lambda(a_0) \left(\frac{a_0}{a}\right)^{3(1+w_0+w_a)} e^{3w_a(a-a(t_0))} \tag{1.1.22}$$

We can consider a few limit cases of (1.1.22). For $w_0 = -1, w_a = 0$ the Dark Energy density ρ_Λ does not depend on a and behaves as a cosmological constant. If $w_0 = -1$ and $w_a \neq 0$, on the other hand, there is a non–trivial scaling of ρ_Λ with a. In order for this scaling relation to reproduce the observational fact that ρ_Λ is negligible at recombination time ($z \sim 1100$), w_a must be negative or zero. Figure 1.1 shows the alteration of the distance–redshift relation (1.1.16) due to the presence of Dark Energy. Using Supernovae IA as standard candles, [6] have measured the $\chi(z)$ relation with sufficient precision to establish Dark Energy as the dominant component in the present Universe, earning the Nobel Prize in 2011.

1.2 Matter density perturbations

In this section we study the deviations from the homogeneous FRW Universe and describe how scalar density perturbations evolve under the effect of gravity. This will be particularly relevant when studying the Gravitational Lensing (GL) effect in the next Chapter, as light ray geodesics deviate from straight lines in the presence of density inhomogeneities. These geodesic deflections have a tangible effect in observations of distant sources, as observed galaxy shapes show apparent distortions that trace the metric perturbations. We review the basic model that describes density perturbations of collision–free Cold Dark Matter in an expanding Universe. Scalar perturbations to the FRW metric (1.1.1) can be parametrized

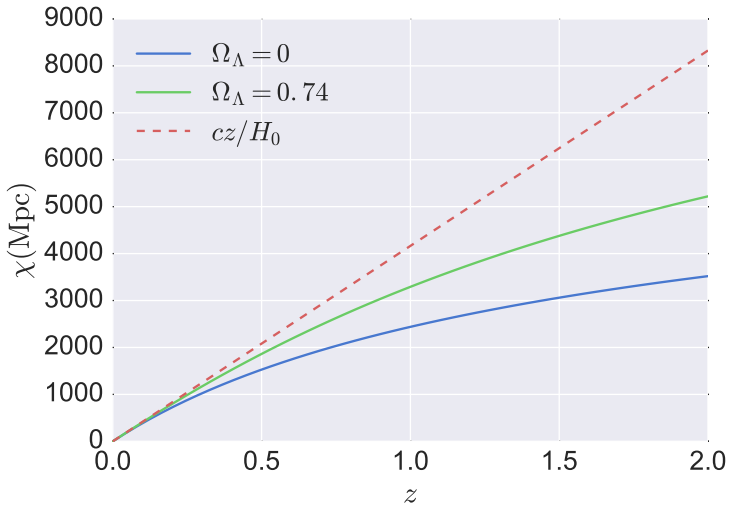

Figure 1.1: Distance–redshift relation for two different Universe models, with and without Dark Energy

in the conformal Newtonian gauge [7] by two scalar potentials Φ, Ψ in the time–time and space–space components of the metric as

$$ds^2 = -c^2dt^2(1 + 2\Psi(\mathbf{x}, t)) + a(t)^2d\mathbf{x}^2(1 + 2\Phi(\mathbf{x}, t)) \tag{1.2.1}$$

For the scope of the present work we can safely ignore vector and tensor perturbations to the FRW metric as their effects are negligible in WL observations. The phase space distribution of Dark Matter is described in terms of a distribution function $f_m(x^\mu, \mathbf{P})$. In this description, $f_m(x^\mu, \mathbf{P})gd^3xd^3P$ is the number of particles contained in a phase space volume d^3xd^3P. We used the notations $P^\mu = (P^0, \mathbf{P})$, $d^3P = dP^xdP^ydP^z$. Note that the momentum dependence of f_m can be expressed in terms of $\mathbf{P}$ only, since the Dark Matter 4–momentum has to satisfy the constraint

$$g_{\mu\nu}P^{\mu}P^{\nu} = -1 \tag{1.2.2}$$

Because the phase space volume element gd^3xd^3P is invariant under coordinate transformations, f_m too must be invariant for the number of particles to be conserved. If we assume f_m to describe a Dark Matter fluid in local equilibrium, we know that f_m depends on the invariant energy e only. Following [8], e is defined defined by

$$e = g_{\mu\nu}P^{\mu}U^{\nu} \tag{1.2.3}$$

The fluid bulk 4–velocity $U^{\mu} = (U^0, \mathbf{U})$ obeys the usual constraint $U^{\mu}U_{\mu} = -1$. We can relate the distribution function to the Dark Matter 4–velocity and stress–energy tensor [8] as

$$\int \frac{d^3P}{P_0}\sqrt{g}P^{\mu}f_m = \rho_m U^{\mu} \tag{1.2.4}$$

$$\int \frac{d^3P}{P_0}\sqrt{g}P^{\mu}P^{\nu}f_m = \mathcal{T}^{\mu\nu} \tag{1.2.5}$$

where, for notational simplicity, we set $\mathcal{T} \equiv \mathcal{T}_m$. Note that equations (1.1.3) and (1.2.5) can be manipulated to obtain expressions for the matter density and pressure in terms of f_m

$$\rho_m = \int \frac{d^3P}{P_0}\sqrt{g}e^2 f_m \tag{1.2.6}$$

$$\mathcal{P}_m = \frac{1}{3}\int \frac{d^3P}{P_0}\sqrt{g}(e^2 - 1)f_m \tag{1.2.7}$$

Using expression (1.2.7), it is easy to show that $\mathcal{P}_m = O(\mathbf{U}^2)$ and that the pressure term can be neglected in the non–relativistic limit, as expected. We parametrize the Dark Matter

density as

$$\rho_m(\mathbf{x}, t) = \bar{\rho}_m(t)(1 + \delta(\mathbf{x}, t)) \tag{1.2.8}$$

where $\bar{\rho}_m(t)$ is the spatially averaged density and $\delta(\mathbf{x}, t)$ is the spatially dependent density contrast. In the next sub–section, we will use the Boltzmann equation for f_m to relate the evolution of δ and $\mathbf{U}$ in the non–relativistic limit.

1.2.1 Collision–free Boltzmann equation

In the absence of collisions between Dark Matter particles, the phase space volume is preserved in the system evolution, and the distribution function satisfies the source–free Boltzmann equation

$$\frac{df_m(x^\mu, \mathbf{P})}{ds} = P^\mu \frac{\partial f_m(x^\mu, \mathbf{P})}{\partial x^\mu} + \frac{dP^i}{ds}\frac{\partial f_m(x^\mu, \mathbf{P})}{\partial P^i} = 0 \tag{1.2.9}$$

The 4–momentum variation rate dP^i/ds can be calculated from the equations of motion, i.e. the geodesic equations for the metric (1.2.1)

$$\frac{dP^\mu}{ds} = -\Gamma^\mu_{\alpha\beta} P^\alpha P^\beta \tag{1.2.10}$$

The collision–free Boltzmann equation (1.2.9) then becomes

$$P^0\partial_0 f_m + P^i\partial_i f_m - \frac{\partial f_m}{\partial P^i}\left(P^0P^0\Gamma^i_{00} + 2\Gamma^i_{0j}P^0P^j + \Gamma^i_{jk}P^jP^k\right) = 0 \tag{1.2.11}$$

Equations for ρ_m, U^μ can be obtained from the P–moments of the Boltzmann equation (1.2.11). We can integrate (1.2.11) in d^3P directly, or we can multiply it by P^j and then integrate. To perform the calculations, we make use of the expressions

$$\int d^3P P^\mu f_m = \frac{\mathcal{T}_0^\mu}{\sqrt{g}} \tag{1.2.12}$$

$$\int d^3P P^0 P^i \frac{\partial f_m}{\partial P^j} = \frac{\mathcal{T}_j^i - \delta_{ij}\mathcal{T}_0^0}{\sqrt{g}} \tag{1.2.13}$$

$$\int d^3P P^0 P^0 \frac{\partial f_m}{\partial P^i} = \frac{2\rho_m U_i}{\sqrt{g}} \tag{1.2.14}$$

$$\int d^3P P^i P^j f_m = O(\mathbf{U}^2) \tag{1.2.15}$$

$$\int d^3P P^0 P^i f_m = \frac{\rho_m U^i}{\sqrt{g}} + O(\mathbf{U}^2) \tag{1.2.16}$$

$$\int d^3P P^i P^j \frac{\partial f_m}{\partial P^k} = -\frac{\delta_{ki}U^j + \delta_{kj}U^i}{\sqrt{g}} + O(\mathbf{U}^2) \tag{1.2.17}$$

$$\int d^3P P^0 P^i P^j \frac{\partial f_m}{\partial P^k} = -\frac{\delta_{ki}U^j + \delta_{kj}U^i}{\sqrt{g}} + O(\mathbf{U}^2) \tag{1.2.18}$$

$$\int d^3P P^0 P^0 P^i \frac{\partial f_m}{\partial P^j} = -\frac{\rho_m \delta_{ij}}{\sqrt{g}} + O(\mathbf{U}^2) \tag{1.2.19}$$

In addition to the above results, we use the approximate expressions for the stress–energy tensor

$$\mathcal{T}_0^0 = -\rho_m + O(\mathbf{U}^2) \quad ; \quad \mathcal{T}_0^i = -(1+2\Psi)\rho_m U^i + O(\mathbf{U}^2) \quad ; \quad \mathcal{T}_j^i = O(\mathbf{U}^2) \tag{1.2.20}$$

We can now perform an integration of equation (1.2.11) in d^3P, taking the non–relativistic limit to discard all $O(\mathbf{U}^2)$ terms. We obtain

$$\frac{\dot{\rho}_m}{c} + \nabla \cdot [(1+2\Psi)\rho_m \mathbf{U}] - \rho_m[\partial_t \log\sqrt{g} + 2(U_i\Gamma^i_{00} - 2\Gamma^i_{0i}) + (1+2\Psi)U^i(\Gamma^j_{ij} + \Gamma^i_{jj})] = 0 \tag{1.2.21}$$

We can also multiply (1.2.11) by P^j and integrate, taking again the non–relativistic limit. The integration yields

$$\partial_t(\rho_m U^j) - \rho_m(U^j\partial_t \log\sqrt{g} - c\Gamma^j_{00} - 8c\Gamma^j_{0i}U^i) = 0 \tag{1.2.22}$$

Although the system of equations (1.2.21) and (1.2.22) can be closed with the help of the Einstein equation (1.1.8), its exact solution is complicated to calculate because of the non–linearity of the system, and usually involves numerical methods [9] or heuristics based on the halo model [10]. In the limit in which the perturbations are still at linear stage, i.e. when the density contrast δ is small, we can trust the linearized version of (1.2.21), (1.2.22). We make use of the linear expression for the affine connection Γ

$$\begin{aligned} \Gamma^0_{00} = \dot{\Psi}/c \quad &; \quad \Gamma^0_{0i} = \Gamma^0_{i0} = \partial_i\Psi \\ \Gamma^0_{ij} = [H + 2H(\Phi-\Psi) + \dot{\Phi}]a^2\delta_{ij}/c \quad &; \quad \Gamma^i_{00} = \partial_i\Psi/a^2 \\ \Gamma^i_{j0} = \Gamma^i_{0j} = (H+\dot{\Phi})\delta_{ij}/c \quad &; \quad \Gamma^i_{jk} = (\delta_{ij}\partial_k + \delta_{ik}\partial_j - \delta_{jk}\partial_i)\Phi \end{aligned} \tag{1.2.23}$$

which, when plugged in (1.2.21), (1.2.22) leads to

$$\dot{\delta} + c\nabla\cdot\mathbf{U} + 3\dot{\Phi} - \dot{\Psi} = 0 \tag{1.2.24}$$

$$\partial_t(\bar{\rho}_m \mathbf{U}) + 5H\bar{\rho}_m \mathbf{U} + \frac{c\nabla\Psi}{a^2} = 0 \tag{1.2.25}$$

In this derivation we used the fact that, in the non–relativistic limit, $\partial_t\bar{\rho}_m + 3H\bar{\rho}_m = 0$ (this relation can also be deducted from the $O(1)$ terms in equation (1.2.21)). We observe that, if one ignores the Φ, Ψ terms in (1.2.24), this relation is a continuity equation which describes mass conservation. In this fashion, $\mathbf{v} = c\mathbf{U}$ can be identified as the peculiar velocity $\dot{\mathbf{x}}$ of a fluid element, on top of the Universe expansion.

1.2.2 Einstein equation

The system composed by the linear equations for δ and $\mathbf{U}$ (1.2.24), (1.2.25) can be closed with the Einstein equation, which relates the potentials Φ, Ψ to the components of the stress–energy tensor. Since we limit our study to scalar perturbations, there are only two independent components of the Einstein equation that need to be considered. WL physics is dominated by the late time behavior of density perturbations, and hence we can ignore relativistic particles and focus on cold matter only. Under this assumption, the $00, 0i$ and ij components of the linearized Einstein equation (1.1.8) become respectively (see [11])

$$\nabla^2\Phi + \frac{3a^2}{c^2}(H^2\Psi - H\dot{\Phi}) = -\frac{4\pi G a^2 \bar{\rho}_m \delta}{c^2} \tag{1.2.26}$$

$$\nabla(\dot{\Phi} - H\Psi) = \frac{4\pi G a^2 \bar{\rho}_m \mathbf{v}}{c^2} \tag{1.2.27}$$

$$\nabla^2(\Phi + \Psi) = 0 \tag{1.2.28}$$

A few considerations are in order here. First of all, the terms in (1.2.26) which contain powers of aH are sub–dominant for the WL case of interest, as the laplacian term is dominant for modes with wavenumber k well inside the Hubble horizon $kc \gg aH$ (see [12] for a discussion of higher order Post Newtonian terms). We can hence drop these terms from (1.2.26), which then reduces to a Poisson–like equation

$$\nabla^2\Phi(\mathbf{x},t) = -\frac{4\pi G a(t)^2}{c^2}\bar{\rho}_m(t)\delta(\mathbf{x},t). \tag{1.2.29}$$

Equation (1.2.28) comes from the traceless part of the spatial Einstein equation and its source term corresponds to anisotropic stresses in the matter components. Because such stresses are proportional to the momentum quadrupole of the their phase space distributions, which is negligible in the non–relativistic limit, anisotropic stresses can be safely neglected when studying WL. We will then use (1.2.28) to conclude $\Psi = -\Phi$, since we assume no singularities in the spatial profiles of Ψ, Φ.

1.2.3 Linear growth factor

The Poisson equation (1.2.29) leads to an equation for the density contrast which is linear in δ. We combine the time derivative of (1.2.24) with the divergence of (1.2.25) and we ignore terms proportional to $\dot{\Psi}, \dot{\Phi}$ (which give rise to PN corrections). After a few algebraic manipulations we get

$$\ddot{\delta} + 2H\dot{\delta} - 4\pi G\bar{\rho}_m\delta = 0 \tag{1.2.30}$$

Because of the linearity of equations (1.2.24) and (1.2.25), each Fourier mode $\tilde{\delta}(\mathbf{k},t)$ evolves independently in time. Moreover, in absence of pressure terms (which would con-

tribute with terms proportional to $\nabla^2\delta$), the density contrast δ evolves in a self–similar fashion

$$\tilde{\delta}(\mathbf{k}, t) = D(t)\tilde{\delta}(\mathbf{k}, 0) \tag{1.2.31}$$

with the linear growth factor D that does not depend on the wavenumber k. Equation (1.2.30) can be converted in a relation for the linear growth factor D with the use of the time–redshift relation (1.1.17) and the Friedmann equations (1.1.10), (1.1.11). After a few algebraic manipulations we obtain

$$\frac{d^2D(z)}{dz^2} + \frac{4\pi G}{3}\left(\frac{\bar{\rho}_m(z) + \rho_\Lambda(z)[1+3w(z)]}{(1+z)H(z)^2}\right)\frac{dD(z)}{dz} - \frac{8\pi G\Omega_m(z)}{H(z)^2(1+z)^2}D(z) = 0 \tag{1.2.32}$$

In the limiting case of a pure Dark Matter universe ($\rho_\Lambda = 0$), (1.2.32) reduces to

$$\frac{d^2D(z)}{dz^2} + \frac{1}{2(1+z)}\frac{dD(z)}{dz} - \frac{3D(z)}{(1+z)^2} = 0 \tag{1.2.33}$$

which admits a solution $D(z) \propto (1+z)^{-1} = a$. Figure 1.2 shows the evolution of the linear growth factor D with redshift for different combinations of the ΛCDM parameters.

1.3 ΛCDM cosmological parameters

One of the main goals of the research presented in this work is to study how WL observations can be used to constrain some of the free parameters that describe the ΛCDM universe. In the conclusion of this Chapter we present a parametrization which will be consistently used throughout the dissertation writeup. The present day Hubble parameter

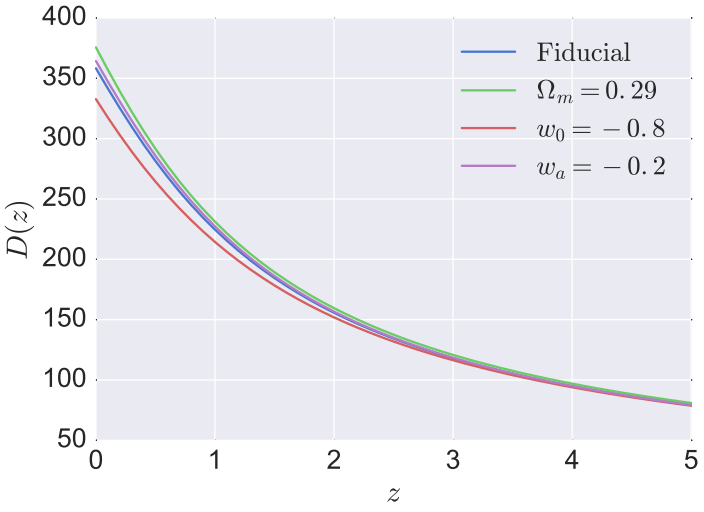

Figure 1.2: Linear growth factor $D(z)$ calculated solving (1.2.32) for 4 different ΛCDM cosmologies. The initial condition has been set for a unit density perturbation at $z = 1000$, namely $D(1000) = 1, \dot{D}(1000) = 0$. Observe the fact that the growth of perturbations is suppressed by the presence of Dark Energy, which accelerates the expansion of the Universe and makes it harder for over–densities to grow.

$H_0 \equiv H(t_0)$ is expressed in terms of the dimensionless number h as

$$H_0 = 100h\,\mathrm{km\,s^{-1}\,Mpc^{-1}} \tag{1.3.1}$$

The densities of the components that source the Einstein equation are usually quoted in the literature in terms of their ratios with the present critical density $\rho_c = 3H_0^2/8\pi G$. We use the notation

$$\Omega_i = \frac{8\pi G\rho_i(t_0)}{3H_0^2} \tag{1.3.2}$$

In addition to Dark Matter and Dark Energy, the present universe contains a significant fraction of baryons ($\Omega_b \approx \Omega_m/6$), whose physics is more complicated to model with respect to the one that controls cold matter, as the Boltzmann equation for baryons contains pressure terms and collisional terms. In this work we ignore baryon physics, although its investigation in cosmology and WL is currently an active area of research. The initial conditions for the density inhomogeneities described in § 1.2 are believed to be set at early times by quantum perturbations, which are present during an epoch of accelerated expansion called *inflation* ([13]). Inflation is believed to generate Gaussian random initial conditions, which are statistically isotropic and nearly scale invariant

$$\langle\tilde{\delta}(\mathbf{k}, z_{\rm in})\tilde{\delta}^*(\mathbf{k}', z_{\rm in})\rangle = (2\pi)^3 P_\delta(k, z_{\rm in})\delta^D(\mathbf{k}-\mathbf{k}') \tag{1.3.3}$$

$$P_\delta(k, z_{\rm in}) = \frac{A_s^2}{k^3}\left(\frac{k}{k_0}\right)^{n_s-1} \tag{1.3.4}$$

In this notation, $n_s = d\log(k^3P_\delta)/d\log k$ is a parameter that describes the deviation from scale invariance ($n_s = 1$ corresponds to scale invariant initial conditions). The overall

normalization of the initial density perturbations A_s is usually expressed in terms of an equivalent parameter, σ_8, defined as

$$\sigma_8 = \int \frac{d^3k}{(2\pi)^3} P_\delta^{\rm lin}(k, z=0) \left| \tilde{W}_{\rm TH}(kr_8) \right|^2 \tag{1.3.5}$$

The meaning if the notation in equation (1.3.5) is that $P_\delta^{\rm lin}$ is obtained from $\tilde{\delta}(\mathbf{k}, z=0)$ calculated with the linear evolution equation (1.2.30). σ_8 is defined as the spatial variance of the present linearly evolved density contrast smoothed with a top hat window of size $r_8 = 8\,{\rm Mpc}/h$. In equation (1.3.5), $\tilde{W}_{\rm TH}$ is the Fourier Transform of the real space top hat window

$$W_{\rm TH}(\mathbf{x}) = \frac{3}{4\pi}\Theta(1 - |\mathbf{x}|) \tag{1.3.6}$$

The randomness of the initial conditions, which is a consequence of the quantum mechanical nature of inflation, is at the base of a phenomenon called *cosmic variance*, which states that cosmological observable quantities are essentially random variables. As a consequence, ΛCDM parameter inferences from observations have to be related to the statistical properties of the observables (i.e. ensemble averages), rather than to the observables themselves. Table 1.1 shows a list of cosmological parameters measured from the Planck experiment [14], as well as the fiducial values used throughout this work. The Dark Energy equation of state parameters w_0, w_a are essentially left unconstrained by CMB experiments, as they are sensitive to early Universe physics in which the Dark Energy density is negligible. WL observations, on the other hand, trace density fluctuations at late times, when the effects of Dark Energy are tangible. In the next Chapter, we will review the Gravitational Lensing effect and show how it can be used as a tracer for Dark Matter density fluctuations.

Parameter	**Planck 2015**	**Fiducial**
h	0.6731 ± 0.0096	0.72
Ω_m	0.315 ± 0.013	0.26
Ω_Λ	0.685 ± 0.013	0.74
Ω_b	0.0490 ± 0.0019	0.046
w_0	-	-1
w_a	-	0
σ_8	0.829 ± 0.014	0.8
n_s	0.9655 ± 0.0062	0.96

Table 1.1: ΛCDM cosmological parameters from the Planck 2015 [14] data best fit (middle column), with 68% confidence level errors, and the fiducial values used in this work (right column).

Chapter 2

Gravitational Lensing

In this Chapter we illustrate the basic concepts of the Gravitational Lensing (GL) effect. GL is a prediction of General Relativity and states that light rays which travel through space–time inhomogeneities experience trajectory deflections. We start by deriving an equation for light ray geodesics in a non homogeneous background, following the derivation in [15]. We then adapt the geodesic solution to the Weak Lensing (WL) case of interest, exploring also approximate approaches such as the Born approximation. We introduce the basic observables of WL, which relate density fluctuations to galaxy shape distortions.

2.1 Light ray geodesics

2.1.1 Geodesic equation

A light ray space–time trajectory $x^\mu(\tau)$ is parametrized with a continuous real parameter τ, which plays the same role as proper time for massive particles. The geodesic equation (1.2.10) can be rewritten as

$$\frac{d^2x^\mu(\tau)}{d\tau^2} = -\Gamma^\mu_{\alpha\beta}(x^\mu(\tau))\frac{dx^\alpha(\tau)}{d\tau}\frac{dx^\beta(\tau)}{d\tau} \tag{2.1.1}$$

For the sake of expressing WL observables at first order in the potentials Φ, Ψ which appear in (1.2.1), it is sufficient to use the linear expressions (1.2.23) for the affine connection $\Gamma^\mu_{\alpha\beta}$. Later in the Chapter we will make an argument for higher order Post Newtonian (PN) corrections to be negligible in the scope of this work, following the conclusions of [12]. We introduce a system of coordinates centered on a fundamental observer on Earth, as illustrated in Figure 2.1

$$x^\mu = (ct, \chi, \mathbf{x}_\perp) \tag{2.1.2}$$

We indicated the transverse coordinates (with respect of the observer) corresponding to an angle $\boldsymbol{\theta}$ on the sky as $\mathbf{x}_\perp = \chi\boldsymbol{\theta}$. We adopt the so called *flat sky* approximation, in which the range of the angles $\boldsymbol{\theta}$ is assumed to be small. Since photons travel along null geodesics, their 4–momentum $P^\mu = dx^\mu/d\tau = (p^0, \mathbf{p})$ satisfies $g_{\mu\nu}P^\mu P^\nu = 0$, which gives the constraint (at first order in Ψ)

$$p^0 = c\frac{dt}{d\tau} = p(1-\Psi) \tag{2.1.3}$$

with $p = |\mathbf{p}|$. Using the fact that $d\chi/dt = -c/a$, we can replace the τ derivatives in (2.1.1) with χ derivatives using the prescription

$$\frac{d}{d\tau} = \frac{dt}{d\tau}\frac{d\chi}{dt}\frac{d}{d\chi} = -\frac{p(1-\Psi)}{a}\frac{d}{d\chi} \tag{2.1.4}$$

If we focus on the transverse components, the LHS of (2.1.1) becomes

$$\frac{d^2\mathbf{x}_\perp}{d\tau^2} = \frac{p}{a}\frac{d}{d\chi}\left(\frac{p}{a}\frac{d\mathbf{x}_\perp}{d\chi}\right) \tag{2.1.5}$$

In (2.1.5) we dropped small terms of order $\Psi d\mathbf{x}_\perp$, following [15]. At dominant order the photon momentum p redshifts as $1/a$, and hence we can pull the product pa out of the differentiation, obtaining

$$\frac{d^2\mathbf{x}_\perp}{d\tau^2} = p^2\frac{d}{d\chi}\left(\frac{1}{a^2}\frac{d\mathbf{x}_\perp}{d\chi}\right) \tag{2.1.6}$$

Now we can focus on the RHS of (2.1.1) which reads, in the transverse spatial components

$$\Gamma^i_{\alpha\beta}\frac{dx^\alpha}{d\tau}\frac{dx^\beta}{d\tau} = \frac{p^2}{a^2}\Gamma^i_{\alpha\beta}\frac{dx^\alpha}{d\chi}\frac{dx^\beta}{d\chi} \tag{2.1.7}$$

If we expand the products in (2.1.7), using the affine connection (1.2.23) at first order in the potentials, we obtain

$$\Gamma^i_{\alpha\beta}\frac{dx^\alpha}{d\tau}\frac{dx^\beta}{d\tau} = \frac{p^2}{a^2}\left[\partial_i\Psi - \frac{2aH}{c}\frac{dx_{\perp,i}}{d\chi} - \partial_i\Phi\right] \tag{2.1.8}$$

The complete geodesic equation now becomes

$$\frac{d}{d\chi}\left(\frac{1}{a^2}\frac{d\mathbf{x}_\perp}{d\chi}\right) = -\frac{1}{a^2}\left[\nabla_\perp(\Psi-\Phi) - \frac{2aH}{c}\frac{d\mathbf{x}_\perp}{d\chi}\right] \tag{2.1.9}$$

After a few simplifications this assumes the form

$$\frac{d^2\mathbf{x}_\perp(\chi)}{d\chi^2} = \nabla_\perp(\Phi(\chi,\mathbf{x}_\perp) - \Psi(\chi,\mathbf{x}_\perp)) \tag{2.1.10}$$

Using the relation (1.2.28) between the gravitational potentials, which allows us to substi-

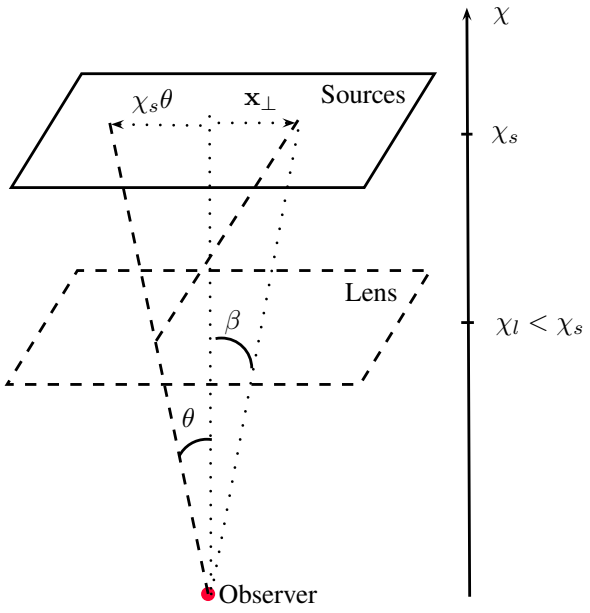

Figure 2.1: Coordinate system centered on a fundamental observer on Earth

tute $\Psi = -\Phi$, equation (2.1.10) becomes

$$\frac{d^2\mathbf{x}_\perp(\chi)}{d\chi^2} = 2\nabla_\perp\Phi(\chi, \mathbf{x}_\perp(\chi)) \tag{2.1.11}$$

The potential Φ satisfies the Poisson equation (1.2.29), which we can rewrite in our coordinate system (2.1.2) as

$$\nabla^2\Phi(\chi, \mathbf{x}_\perp) = -\frac{4\pi G a(\chi)^2}{c^2}\rho_m(\chi)\delta(\chi, \mathbf{x}_\perp) \tag{2.1.12}$$

We substituted the time dependency with a χ dependency using the time–redshift relation (1.1.17).

2.1.2 Solution to the geodesic equation

The geodesic equation (2.1.11) is a second order differential equation which can be solved once suitable initial conditions are specified. If we indicate with $\boldsymbol{\theta}$ the angular position of the light ray as it is detected by the observer, we have $\mathbf{x}_\perp(0) = 0$ and $d\mathbf{x}_\perp(0)/d\chi = \boldsymbol{\theta}$. Equation (2.1.11) can then be solved by a double integration

$$\mathbf{x}_\perp(\chi, \boldsymbol{\theta}) = \chi\boldsymbol{\theta} + 2\int_0^\chi d\chi' \int_0^{\chi'} d\chi'' \nabla_\perp \Phi(\chi, \mathbf{x}_\perp(\chi'', \boldsymbol{\theta})) \tag{2.1.13}$$

We can exchange the order of the integration in χ' and χ'' by taking advantage of the triangular shape of the integration domain, and we can perform one of the integrations analytically to get

$$\mathbf{x}_\perp(\chi, \boldsymbol{\theta}) = \chi\boldsymbol{\theta} + 2\int_0^\chi d\chi' (\chi - \chi') \nabla_\perp \Phi(\chi', \mathbf{x}_\perp(\chi', \boldsymbol{\theta})) \tag{2.1.14}$$

We expressed the solution (2.1.14) to (2.1.11) in implicit form, as the RHS contains $\mathbf{x}_\perp(\chi, \boldsymbol{\theta})$ itself. An implicit expression like (2.1.14) however, present some advantages. First of all, in order to know the solution at some χ_s, we only need knowledge of $\mathbf{x}_\perp$ for $\chi < \chi_s$, making (2.1.14) numerically computable via dynamic programming. Moreover, because the potential Φ appears in the RHS, in the limit in which Φ is small, the implicit form of the solution suggests a straightforward perturbative approximation in powers of Φ[16], which will be explored later in the Chapter. In the next section we connect the light ray geodesic (2.1.14) to the main WL observables.

2.2 Weak Gravitational Lensing

2.2.1 Weak Lensing observables

Gravitational Lensing produces apparent distortions in the observed shapes of background sources. Following the notation introduced in Figure 2.1, a light ray captured by the observer at a position $\boldsymbol{\theta}$, in reality originated from a point that, on the sky, corresponds to an angle $\boldsymbol{\beta}$. Overall shifts in the relation $\boldsymbol{\beta}(\boldsymbol{\theta})$ do not alter the source (that we assume distributed on a plane at $\chi = \chi_s$) observed shape, but only cause unobservable image displacements. The lowest order image distortions come from the differential position shifts $\partial\beta_i/\partial\theta_j$, which alter the observed source ellipticity. Higher order flexion corrections to source shapes have been investigated in the literature [16], but will not be investigated in this work. Elliptical deformations in the shape of background sources are parametrized in terms of the deflection Jacobian matrix $\mathbf{A}$

$$A_{ij}(\chi_s, \boldsymbol{\theta}) = \frac{\partial \beta_i(\chi_s, \boldsymbol{\theta})}{\partial \theta_j} \equiv \begin{pmatrix} 1 - \kappa(\boldsymbol{\theta}) - \gamma^1(\boldsymbol{\theta}) & -\gamma^2(\boldsymbol{\theta}) + \omega(\boldsymbol{\theta}) \\ -\gamma^2(\boldsymbol{\theta}) - \omega(\boldsymbol{\theta}) & 1 - \kappa(\boldsymbol{\theta}) + \gamma^1(\boldsymbol{\theta}) \end{pmatrix} \tag{2.2.1}$$

In this parametrization, κ is called the WL convergence, $\boldsymbol{\gamma} = (\gamma^1, \gamma^2)$ is the WL cosmic shear and ω is the WL rotation angle. Inverting equation (2.2.1) we obtain the relations

$$\begin{aligned} \kappa = 1 - \mathrm{Tr}\mathbf{A}/2 \quad &; \quad \gamma^1 = (A_{yy} - A_{xx})/2 \\ \gamma^2 = -(A_{xy} + A_{yx})/2 \quad &; \quad \omega = \mathrm{Tr}(\mathbf{A}\boldsymbol{\varepsilon})/2 \end{aligned} \tag{2.2.2}$$

Figure 2.2 shows a physical interpretation of these different types of distortions, for an non–lensed circular image. The convergence is related to the background source apparent

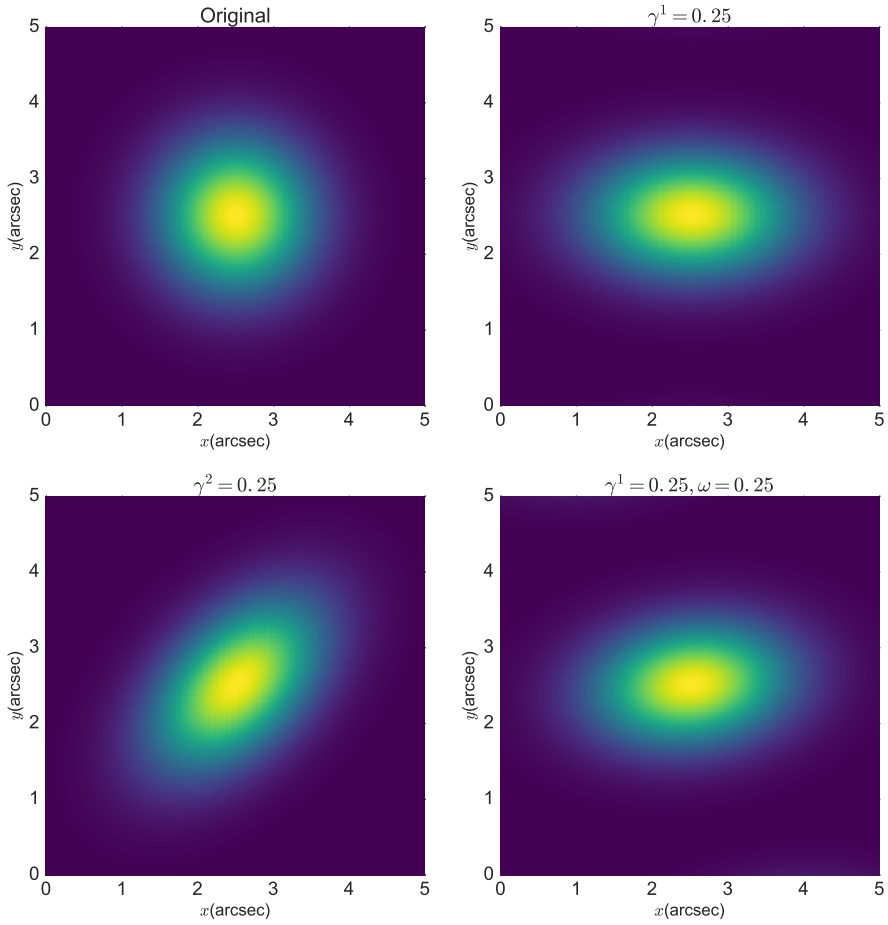

Figure 2.2: Effect of differential distortions due to $\boldsymbol{\gamma}, \omega$ on a background circular image

magnifications, and is not directly observable unless the non–lensed size of the source is known in advance. The cosmic shear $\boldsymbol{\gamma}$ encodes the ellipticity of the distortion and the rotation ω is connected to the angular tilt of the distorted image shape. Calling $I(\boldsymbol{\beta})$ and $I_{\rm obs}(\boldsymbol{\theta})$ the emitted and observed source intensity profiles respectively, we can define the observed ellipticity $\boldsymbol{\epsilon}$ of the distorted image in terms of the quadrupole moment of the intensity

$$\epsilon^1 = \frac{q_{xx} - q_{yy}}{\mathrm{Tr}\mathbf{q} + 2\sqrt{|\mathbf{q}|}} \quad ; \quad \epsilon^2 = \frac{2q_{xy}}{\mathrm{Tr}\mathbf{q} + 2\sqrt{|\mathbf{q}|}} \tag{2.2.3}$$

The quadrupole moment q_{ij} is defined by

$$q_{ij} = \int d\boldsymbol{\theta}\theta_i\theta_j I_{\rm obs}(\boldsymbol{\theta}) = \int d\boldsymbol{\beta}(\mathbf{A}^{-1}\boldsymbol{\beta})_i(\mathbf{A}^{-1}\boldsymbol{\beta})_j I(\boldsymbol{\beta}) \tag{2.2.4}$$

Flexion corrections have been ignored in the last equality. Provided that the image is small enough so that $\kappa, \boldsymbol{\gamma}$ are constant over its profile, equation (2.2.4) can be used to relate the observed quadrupole moment $\mathbf{q}$ to the the non–lensed quadrupole $\mathbf{q}^s$ as

$$\mathbf{q} = \mathbf{A}^{-1}\mathbf{q}^s\left(\mathbf{A}^T\right)^{-1} \tag{2.2.5}$$

If the non–lensed image is a circle, we can use $\mathbf{q}^s = \mathbb{1}_{2\times 2}$ to get, ignoring ω terms

$$\epsilon^1 = \frac{(A^{-1}_{xx})^2 - (A^{-1}_{yy})^2}{\mathrm{Tr}\left(\mathbf{A}^{-1}(\mathbf{A}^T)^{-1}\right) + 2|\mathbf{A}^{-1}|} \quad ; \quad \epsilon^2 = \frac{2A^{-1}_{xy}\mathrm{Tr}\left(\mathbf{A}^{-1}\right)}{\mathrm{Tr}\left(\mathbf{A}^{-1}(\mathbf{A}^T)^{-1}\right) + 2|\mathbf{A}^{-1}|} \tag{2.2.6}$$

After some algebra, we obtain a relation between the ellipticity of the distorted image and the components of $\mathbf{A}$

$$\boldsymbol{\epsilon} = \mathbf{g} \equiv \frac{\boldsymbol{\gamma}}{1-\kappa} \tag{2.2.7}$$

which shows that the source ellipticity and shear are proportional to each other and hence $\boldsymbol{\epsilon}$ be used to estimate $\boldsymbol{\gamma}$. Even if the real observable quantity is the reduced shear $\mathbf{g} \equiv \boldsymbol{\gamma}/(1-\kappa)$, when $\kappa \ll 1$ (which is often the case in WL), one can approximate $\boldsymbol{\epsilon} \approx \boldsymbol{\gamma}$. In the next section we will show how to relate the WL quantities $\kappa, \boldsymbol{\gamma}, \omega$ to the gravitational lensing potential Φ.

2.2.2 Ray–tracing

Relating observable WL quantities such as the source ellipticity $\boldsymbol{\epsilon}$ and the cosmic shear $\boldsymbol{\gamma}$ to the potential Φ can be done by the means of equation (2.1.14), which relates light geodesics to the matter density fluctuations. We can convert the transverse physical coordinates $\mathbf{x}_\perp$ into angles dividing by the longitudinal distance χ

$$\boldsymbol{\beta}(\chi, \boldsymbol{\theta}) = \boldsymbol{\theta} + 2\int_0^\chi d\chi' \left(1 - \frac{\chi'}{\chi}\right) \nabla_\perp \Phi(\chi', \chi'\boldsymbol{\beta}(\chi', \boldsymbol{\theta})) \tag{2.2.8}$$

Differentiating (2.2.8) with respect to $\boldsymbol{\theta}$ we can obtain a similar relation for the Jacobian $\mathbf{A}$

$$A_{ij}(\chi, \boldsymbol{\theta}) = \delta_{ij} + 2\int_0^\chi d\chi'\chi' \left(1 - \frac{\chi'}{\chi}\right) T^\Phi_{ik}(\chi', \chi'\boldsymbol{\beta}(\chi', \boldsymbol{\theta}))A_{kj}(\chi', \boldsymbol{\theta}) \tag{2.2.9}$$

In equation (2.2.9) we introduced the tidal tensor $T^\Phi_{ij} = \partial_i\partial_j\Phi$. Much like (2.1.14), equation (2.2.9) is an implicit relation which allows to calculate $\mathbf{A}(\chi_s, \boldsymbol{\theta})$ at an arbitrary χ_s once all values $\mathbf{A}(\chi, \boldsymbol{\theta})$ are known for $\chi < \chi_s$. A numerical solution to this problem which makes

use of the multi–lens–plane algorithm [17, 18] will be explored in the next Chapter. The fact that the potential Φ appears on the RHS of (2.2.9) suggests the possibility of a perturbative expansion of $\mathbf{A}$ in powers of Φ, which is expected to be valid when Φ is small. If we focus on the perturbation terms which are at most quadratic in Φ, we can write

$$A_{ij}(\chi, \boldsymbol{\theta}) = \delta_{ij} + A^{(1)}_{ij}(\chi, \boldsymbol{\theta}) + A^{(2)}_{ij}(\chi, \boldsymbol{\theta}) + O(\Phi^3) \tag{2.2.10}$$

To obtain an expression for the linear term, we can replace Jacobian on the RHS of (2.2.9) with the identity matrix and the spatial argument of Φ with the unperturbed $\chi\boldsymbol{\theta}$. This approach is analogous to the Born approximation commonly used in Quantum Mechanics when computing scattering amplitudes at first order in the interaction potential. The linear term in (2.2.10) reads

$$A^{(1)}_{ij}(\chi, \boldsymbol{\theta}) = 2 \int_0^\chi d\chi' \chi' \left(1 - \frac{\chi'}{\chi}\right) T^{\Phi}_{ij}(\chi', \chi'\boldsymbol{\theta}) \tag{2.2.11}$$

Equation (2.2.11) essentially says that, at lowest perturbative order, the lensing Jacobian is a line integral of the tidal field T^{Φ}_{ij} along the unperturbed geodesic trajectory $\chi\boldsymbol{\theta}$, weighted with a lensing kernel W defined by

$$W(\chi', \chi) = \chi' \left(1 - \frac{\chi'}{\chi}\right) \tag{2.2.12}$$

With the use of (2.2.2), we can express the convergence at first order in the lensing potential as

$$\kappa^{(1)}(\chi, \boldsymbol{\theta}) = \int_0^\chi d\chi' W(\chi', \chi) \delta_L(\chi', \chi'\boldsymbol{\theta}) \tag{2.2.13}$$

where the lensing density δ_L is

$$\delta_L(\chi, \mathbf{x}_\perp) = -\nabla_\perp^2 \Phi(\chi, \mathbf{x}_\perp) \tag{2.2.14}$$

The meaning of equation (2.2.13) is that the WL convergence κ is the integrated column density contrast δ on the line of sight between the observer and the source. Note that because the first order WL quantities are proportional to the integrated tidal field, which is symmetric, the WL rotation ω vanishes at linear order, as can be seen in equation (2.2.2). Quadratic corrections to the linear relation (2.2.11) between $\mathbf{A}$ and Φ come from two different terms in equation (2.2.9): one term is generated by replacing the Jacobian in the RHS of (2.2.9) with its first order approximation $A_{ij}^{(1)}$, the other comes from the transverse argument of the tidal field T_{ij}^{Φ}, which contains the perturbations to the ray geodesics. Using the approximation

$$T_{ij}^{\Phi}(\chi, \chi\boldsymbol{\beta}(\chi, \boldsymbol{\theta})) = T_{ij}^{\Phi}(\chi, \chi\boldsymbol{\theta}) + \chi \partial_k T_{ij}^{\Phi}(\chi, \chi\boldsymbol{\theta})[\beta_k^{(1)}(\chi, \boldsymbol{\theta}) - \theta_k] + O(\Phi^3) \tag{2.2.15}$$

we can write a second order expression for $\mathbf{A}$

$$\mathbf{A}^{(2)}(\chi, \boldsymbol{\theta}) = \mathbf{A}^{(2-\mathrm{ll})}(\chi, \boldsymbol{\theta}) + \mathbf{A}^{(2-\mathrm{gp})}(\chi, \boldsymbol{\theta}) \tag{2.2.16}$$

$$A_{ij}^{(2-\mathrm{ll})}(\chi, \boldsymbol{\theta}) = 4 \int_0^{\chi} d\chi' \int_0^{\chi'} d\chi'' W_2(\chi'', \chi', \chi) T_{ik}^{\Phi}(\chi', \chi'\boldsymbol{\theta}) T_{kj}^{\Phi}(\chi'', \chi''\boldsymbol{\theta}) \tag{2.2.17}$$

$$A_{ij}^{(2-\mathrm{gp})}(\chi, \boldsymbol{\theta}) = 4 \int_0^{\chi} d\chi' \int_0^{\chi'} d\chi'' W_2(\chi'', \chi', \chi) \frac{\chi'}{\chi''} \partial_k T_{ij}^{\Phi}(\chi', \chi'\boldsymbol{\theta}) \partial_k \Phi(\chi'', \chi''\boldsymbol{\theta}) \tag{2.2.18}$$

with $W_2(t,u,v) = W(t,u)W(u,v)$. The term (2.2.17) originates from the lens–lens coupling between the tidal field at different distances χ, while the term (2.2.18) has to do with the first order perturbations in the light ray geodesics due to the density fluctuations. Equations (2.2.17) and (2.2.18) can be easily translated into second order expressions for κ

$$\kappa^{(2-\mathrm{ll})}(\chi,\boldsymbol{\theta}) = -2\int_0^{\chi} d\chi' \int_0^{\chi'} d\chi'' W_2(\chi'',\chi',\chi)\mathrm{Tr}[\mathbf{T}^{\Phi}(\chi',\chi'\boldsymbol{\theta})\mathbf{T}^{\Phi}(\chi'',\chi''\boldsymbol{\theta})] \quad (2.2.19)$$

$$\kappa^{(2-\mathrm{gp})}(\chi,\boldsymbol{\theta}) = 2\int_0^{\chi} d\chi' \int_0^{\chi'} d\chi'' \frac{\chi' W_2(\chi'',\chi',\chi)}{\chi''} \nabla_{\perp}\delta_L(\chi',\chi'\boldsymbol{\theta}) \cdot \nabla_{\perp}\Phi(\chi'',\chi''\boldsymbol{\theta}) \quad (2.2.20)$$

For the sake of completeness, we should note that the quadratic terms (2.2.19),(2.2.20) are not the only ones that contribute to the WL convergence, as they ignore PN corrections. If one includes the PN corrections to (2.1.11), as shown in [12], additional quadratic contributions $\kappa^{(2-\mathrm{PN})}$ appear according to the expression

$$\kappa^{(2-\mathrm{PN})}(\chi,\boldsymbol{\theta}) = \int_0^{\chi} d\chi' W(\chi',\chi)\left[|\nabla_{\perp}\Phi(\chi',\chi'\boldsymbol{\theta})|^2 + \Phi(\chi',\chi'\boldsymbol{\theta})\nabla_{\perp}^2\Phi(\chi',\chi'\boldsymbol{\theta})\right] \quad (2.2.21)$$

Comparing equation (2.2.21) with (2.2.19) and (2.2.20), we can easily observe that PN corrections to κ are suppressed by a factor of order $\lambda_m H/c$, with λ_m indicating a characteristic coherence scale for the matter density perturbations. [12] suggest that this suppression factor can be safely estimated to be of the order of $\sim 10^{-2}$ at the location where the lensing kernel W usually peaks, making PN corrections suppressed by a factor of order of $\sim 10^{-4}$. Throughout this work, we will neglect these PN corrections to κ. We can also derive an

expression for the dominant contribution to the rotation ω by looking the antisymmetric part of $\mathbf{A}$, which comes from lens–lens couplings

$$\omega^{(2)}(\chi,\boldsymbol{\theta}) = 2\int_0^{\chi} d\chi' \int_0^{\chi'} d\chi'' W_2(\chi'',\chi',\chi)\mathrm{Tr}[\mathbf{T}^{\Phi}(\chi',\chi'\boldsymbol{\theta})\boldsymbol{\varepsilon}\mathbf{T}^{\Phi}(\chi'',\chi''\boldsymbol{\theta})] \tag{2.2.22}$$

In the conclusion of the Chapter we show an approximate relation between the WL convergence and shear that proves particularly useful when analyzing survey data.

2.2.3 E/B mode decomposition of the shear

The convergence κ and cosmic shear $\boldsymbol{\gamma}$ can be approximately related to each other if one focuses on their $O(\Phi)$ expressions. This relation proves useful in reconstructing the non observable κ profile from ellipticity observations, which directly probe the shear field. Equation (2.2.11) clearly states that, at linear order in Φ, the differential distortion $\mathbf{A}$ is the Hessian matrix of the longitudinally projected gravitational potential potential

$$A_{ij}^{(1)}(\chi,\boldsymbol{\theta}) = \partial_i\partial_j\Phi_2(\chi,\boldsymbol{\theta}) \tag{2.2.23}$$

$$\Phi_2(\chi,\boldsymbol{\theta}) = \int_0^{\chi} \frac{d\chi'}{\chi'^2} W(\chi',\chi)\Phi(\chi',\chi'\boldsymbol{\theta}) \tag{2.2.24}$$

Using the linear expression for the convergence

$$\kappa^{(1)}(\chi,\boldsymbol{\theta}) = -\frac{1}{2}\nabla_{\perp}^2\Phi_2(\chi,\boldsymbol{\theta}), \tag{2.2.25}$$

we can invert the Laplacian operator and get an approximate relation between convergence and shear

$$\gamma^1(\chi,\boldsymbol{\theta}) = \nabla_\perp^{-2}(\partial_x^2 - \partial_y^2)\kappa(\chi,\boldsymbol{\theta}) + O(\Phi^2)$$
$$\gamma^2(\chi,\boldsymbol{\theta}) = 2\nabla_\perp^{-2}\partial_x\partial_y\kappa(\chi,\boldsymbol{\theta}) + O(\Phi^2) \tag{2.2.26}$$

This relation can be written in a more compact way in Fourier space using the complex shear field $\gamma = \gamma^1 + i\gamma^2$

$$\tilde{\gamma}_{\rm KS}(\chi,\boldsymbol{\ell}) \equiv \left(\frac{\ell_x^2 - \ell_y^2 + 2i\ell_x\ell_y}{\ell_x^2 + \ell_y^2}\right)\tilde{\kappa}(\chi,\boldsymbol{\ell}) = e^{2i\phi_{\boldsymbol{\ell}}}\tilde{\kappa}(\chi,\boldsymbol{\ell}) \tag{2.2.27}$$

In equation (2.2.27), we introduced the Fourier angle $\phi_{\boldsymbol{\ell}}$ defined by $\cos\phi_{\boldsymbol{\ell}} = \ell_x/\ell$, $\sin\phi_{\boldsymbol{\ell}} = \ell_y/\ell$. Equation (2.2.27) takes the name of Kaiser–Squires (KS) relation between convergence and shear [19], and can be inverted for the sake of reconstructing the convergence profile from the cosmic shear at first order in Φ

$$\tilde{\kappa}_{\rm KS}(\chi,\boldsymbol{\ell}) = e^{-2i\phi_{\boldsymbol{\ell}}}\tilde{\gamma}(\chi,\boldsymbol{\ell}) = \tilde{\gamma}^E(\chi,\boldsymbol{\ell}) + i\tilde{\gamma}^B(\chi,\boldsymbol{\ell}) \tag{2.2.28}$$

The shear Fourier E and B modes are defined to be

$$\tilde{\gamma}^E(\chi,\boldsymbol{\ell}) = \tilde{\gamma}^1(\chi,\boldsymbol{\ell})\cos 2\phi_{\boldsymbol{\ell}} + \tilde{\gamma}^2(\chi,\boldsymbol{\ell})\sin 2\phi_{\boldsymbol{\ell}}$$
$$\tilde{\gamma}^B(\chi,\boldsymbol{\ell}) = -\tilde{\gamma}^1(\chi,\boldsymbol{\ell})\sin 2\phi_{\boldsymbol{\ell}} + \tilde{\gamma}^2(\chi,\boldsymbol{\ell})\cos 2\phi_{\boldsymbol{\ell}} \tag{2.2.29}$$

Note that, because of (2.2.26) and (2.2.29), we have that $\tilde{\gamma}^E = \tilde{\kappa} + O(\Phi^2)$ and $\tilde{\gamma}^B = O(\Phi^2)$. In practice one can estimate the convergence κ as the E–mode of the shear in the WL limit, and use the detection of a large B–mode as an indication of systematic effects [20]. Figure 2.3 shows the spatial pattern KS reconstructed shear field corresponding to positive

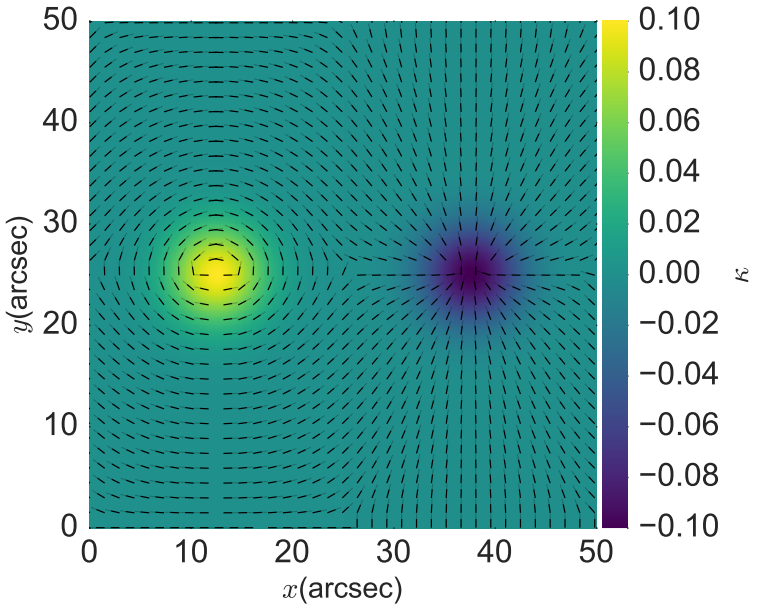

Figure 2.3: E–mode pattern for the shear around positive and negative κ peaks

and negative κ peaks. In real observations the convergence profile is reconstructed using (2.2.28) on the shear field estimated from the observed source ellipticities. Because the non–lensed shapes of typical galaxies are not circular, equation (2.2.7) cannot be directly used as an estimator for the shear, because of intrinsic shape contributions to the observed ellipticity. If the source has an intrinsic complex ellipticity ϵ^s, in the limit of $|g| < 1$, one can use (2.2.5) to calculate the observed ellipticity of the sheared image ϵ as (see [18])

$$\epsilon = \frac{g + \epsilon^s}{1 + g^* \epsilon^s} \tag{2.2.30}$$

Equation (2.2.30) still leads to an unbiased estimate of the WL reduced shear ($\langle \epsilon \rangle = g$), provided the intrinsic major axes of the sources are randomly oriented. This however causes an increase in the statistical error of the κ estimate, which is effectively modeled as an

additive noise term to the cosmic shear. Shape noise is usually modeled as a Gaussian, spatially uncorrelated stochastic contribution to each component of the shear [21]. As a net effect, shape noise acts as white noise $\kappa_{\rm SN}$ on top of the κ signal generated by lensing. In this work we will assume (see again [21]) for the shape noise

$$\langle \hat{\kappa}_{\rm SN}(z_s, \boldsymbol{\theta}) \hat{\kappa}_{\rm SN}(z_s, \boldsymbol{\theta}') \rangle = \frac{(0.15 + 0.035 z_s)^2}{n_g} \delta^D(\boldsymbol{\theta} - \boldsymbol{\theta}') \tag{2.2.31}$$

where n_g is the angular density of source galaxies. Note the $1/n_g$ scaling in the shape noise root–mean–square value, which is dictated by the Central Limit Theorem.

Chapter 3

Numerical Weak Lensing

In this Chapter we describe the relevant numerical methods for simulating WL observations. We use publicly available software to trace the non–linear time evolution of the matter density contrast $\delta(t)$. We then solve the geodesic equation numerically by adding the multiple deflections which light experiences when traveling from sources to observers. The solution of the geodesic equation for a sufficient number of light rays allows to reconstruct the spatial profiles of the WL observables $\kappa, \boldsymbol{\gamma}, \omega$. We conclude the Chapter by presenting our ray–tracing software `LensTools`, which we have publicly released for the use of the WL community.

3.1 Cosmological simulations

The evolution of the matter density contrast δ is controlled, at linear stage, by equation (1.2.30). For WL studies, however, δ becomes too big at the redshifts of interest ($z \sim 1$) for the linear approximation to still be valid and exact solutions of (1.2.21), (1.2.22) and (1.1.8) are required. A popular approach to solve Boltzmann's equation (1.2.9) for collision–free

Dark Matter is the N–body method, which proceeds in a discretization of phase space using a large but finite number N_p of particle tracers (see [9]). The particles are placed in a cubical periodic box of comoving size L_b and are assigned initial conditions which correspond to the density contrast at high z, for which the linear approximation is still valid. The particle system is then evolved with a Hamiltonian that mimics Newtonian gravitational interactions (PN corrections are neglected under the assumption $L_b \ll c/H$), described by the potential Φ.

3.1.1 Initial conditions

The starting step of an N–body simulation is a configuration of particle positions $\{\mathbf{x}_i\}$ and velocities $\{\mathbf{v}_i\}$ at some initial high redshift $z_{\rm in} \gg 1$. The starting particle configuration traces the linear density contrast δ. The particles are initially are arranged in a *glass* pattern and are given positions $\{\mathbf{x}_i^g\}$ which correspond to a uniform density profile ($\delta \approx 0$). The particles are displaced from their position in the glass by a small amount $\mathbf{d}(\mathbf{x}_i^g)$, which is chosen so that the new density profile matches an arbitrary input δ profile. Because mass is conserved by the displacement transformation, we can impose the condition

$$\rho_m d^3x^g = \rho_m(1+\delta)d^3x, \tag{3.1.1}$$

which relates the density contrast δ to the Jacobian of the displacement transformation, $\mathbf{x}(\mathbf{d}) = \mathbf{x}^g + \mathbf{d}$, as

$$1 + \delta = \left| \mathbb{1}_{3\times 3} + \frac{\partial \mathbf{d}}{\partial \mathbf{x}} \right|^{-1} \tag{3.1.2}$$

Using the matrix identity

$$|\mathbb{1} + \lambda \mathbf{M}| = 1 + \lambda \mathrm{Tr}\mathbf{M} + O(\lambda^2) \tag{3.1.3}$$

for a generic square matrix $\mathbf{M}$ and real λ, and noting that at high redshift we expect δ and $\mathbf{d}$ to be small, we obtain a linear relation between the density contrast and the displacement field, which reads

$$\delta = -\nabla \cdot \mathbf{d} \tag{3.1.4}$$

A possible solution to equation (3.1.4) is best expressed in Fourier space if we assume the displacement to be longitudinal (which is a good assumption since the peculiar velocity field is approximately curl–free)

$$\tilde{\mathbf{d}}(\mathbf{k}) = \frac{i\mathbf{k}}{k^2}\tilde{\delta}(\mathbf{k}) \tag{3.1.5}$$

Equation (3.1.5) takes the name of Zel'dovich approximation (see [22] for a review), and it essentially states that the displacement field that corresponds to the input δ profile is proportional to the gradient of the local gravitational potential. The Fourier coefficients $\tilde{\delta}(\mathbf{k})$ are random draws from a normal distribution with variance $P_\delta(k, z_{\rm in})$. The linear δ power spectrum $P_\delta(k, z_{\rm in})$ can be analytically computed with Einstein–Boltzmann software such as `CAMB` [23]. We assign the initial peculiar velocities $\mathbf{v} = \dot{\mathbf{d}}$ in the context of the Zel'dovich approximation using the time derivative of δ. Since we limit ourselves to Dark Matter density perturbations, we can assume a self–similar linear growth model described by the linear growth factor $D(z)$, which appears in equation (1.2.32). In order to imprint baryon physics in the initial conditions, we adopt a hybrid approach in which we use `CAMB` to compute the linear matter power spectrum $P_\delta^{\rm lin}(\mathbf{k}, 0)$ at the present time, with baryons

included. We then scale $P_\delta^{\rm lin}$ back to $z_{\rm in} = 100$ using the linear growth factor

$$P_\delta(\mathbf{k}, z_{\rm in}) = P_\delta^{\rm lin}(\mathbf{k}, 0) \left(\frac{D(z_{\rm in})}{D(0)} \right)^2 \tag{3.1.6}$$

This initial condition (which includes baryon effects) is then evolved according to Dark Matter only collision–free dynamics. Random realizations of $\tilde{\delta}$ are drawn from a normal distribution with variance $P_\delta^{\rm lin}$ and the peculiar particle velocities $\mathbf{v}$ are assigned according to

$$\tilde{\mathbf{v}}(\mathbf{k}) = \frac{i\mathbf{k}}{k^2} \tilde{\delta}(\mathbf{k}) \left(\frac{\dot{z}}{D(z)} \frac{dD(z)}{dz} \right)_{z=z_{\rm in}} \tag{3.1.7}$$

We used the `N-GenIC` software add–on to `Gadget2` [9] in order to generate random realizations of the $\mathbf{d}, \mathbf{v}$ initial conditions from the linear δ power spectrum $P_\delta^{\rm lin}(\mathbf{k}, 0)$.

3.1.2 Time evolution

Once generated, the initial conditions specified by equations (3.1.5) and (3.1.7) are evolved in time from $z = z_{\rm in}$ until the present redshift $z = 0$. Since we consider collision–free Dark Matter, which interacts only via gravitational forces, the Hamiltonian $\mathcal{H}$ of the particle system (ignoring PN corrections, since we are in the limit $L_b \ll c/H$) can be written as

$$\mathcal{H} = \sum_{i=1}^{N_p} \frac{\mathbf{p}_i^2}{2m_i a(t)^2} + \frac{1}{2} \sum_{i \neq j} m_i m_j \varphi(\mathbf{x}_i - \mathbf{x}_j) \tag{3.1.8}$$

We denoted the particle masses as m_i, the particle momenta conjugated to the comoving coordinates $\mathbf{x}_i$ as $\mathbf{p}_i$ and the pair interaction potential per unit mass as as φ. If periodic boundary conditions are imposed on the boundary of the simulation box, the interaction

potential satisfies the Poisson equation

$$\nabla^2\varphi(\mathbf{x}) = \frac{4\pi G}{a}\left(\sum_{\mathbf{n}\in\mathbb{Z}^3}\delta_{r_s}(\mathbf{x}-\mathbf{n}L_b) - \frac{1}{L_b^3}\right) \tag{3.1.9}$$

where δ_{r_s} is the Dirac delta function δ^D convolved with a softening kernel of scale r_s. The softening is introduced because the N–body particles are in reality extended objects and the Newtonian interaction potential needs to be smoothed out on interaction scales smaller than r_s. In our simulations r_s has been fixed to $r_s \approx 10\,\mathrm{kpc}/h$. Note that the summation can be dropped if we restrict $\mathbf{x}$ to be inside the box, but is important in order to enforce the periodic boundary conditions. We can relate φ to the gravitational potential in (1.2.29) by

$$\Phi(\mathbf{x},t) = -\frac{1}{c^2}\sum_{i=1}^{N_p} m_i\varphi(\mathbf{x}-\mathbf{x}_i(t)) \tag{3.1.10}$$

We can observe that, inside the simulation box, equation (3.1.10) leads to

$$\nabla^2\Phi(\mathbf{x},t) = -\frac{4\pi G a^2}{c^2}\left(\sum_{i=1}^{N_p} m_i\delta_{r_s}\left(a(\mathbf{x}-\mathbf{x}_i(t))\right) - \frac{1}{a^3L_b^3}\sum_{i=1}^{N_p} m_i\right) \tag{3.1.11}$$

Note that (3.1.11) is essentially the discretized version of (1.2.29) for a system made of N_p particles, where gravitational forces are softened on scales below r_s. The Hamiltonian equations of motion derived from (3.1.8) can be numerically integrated and yield a trajectory $\mathbf{x}_i(t)$ for each particle. To preserve the Hamiltonian nature of the time evolution, [9] suggest adopting a Kick–Drift–Kick (KDK) numerical integration scheme. The drift step updates the particle coordinates from their momenta, while the kick updates the momenta using the local force field. The force field calculation requires the solution of (3.1.9) and a

summation over all particle pairs, which leads to an $O(N_p^2)$ time complexity. In the limit of collision–free dynamics, approximate force field calculations can be performed with a significantly lower complexity using the hybrid Tree Particle Mesh (TreePM) approach. The details of the force field calculation, time integration and TreePM implementation can be found in the `Gadget2` paper [9]. We used the publicly available version of the `Gadget2` code to perform the N–body simulations on which our WL simulations are based. We stored the N–body simulation outputs $\{\mathbf{x}_i(t)\}$ at a discrete set of time steps $\{t_k\}$. We then used these outputs to estimate the potential Φ necessary from which WL observables $\kappa, \boldsymbol{\gamma}$ can be reconstructed. We describe the numerical details of the WL simulations in the next section.

3.2 The multi–lens–plane algorithm

3.2.1 Geodesic solver

In this section we review the algorithm used to solve the light geodesic equation (2.1.11). This algorithm allows us to compute the $\boldsymbol{\beta}$ (2.2.8) and $\mathbf{A}$ (2.2.9) integrals in an efficient and numerically stable fashion. In the remainder of the Chapter we will assume that source galaxies are positioned at fixed longitudinal comoving distance χ_s. A particular light ray is observed at an angular position $\boldsymbol{\theta}$ on the sky due to lensing, but its originating angular position is $\boldsymbol{\beta}(\chi_s, \boldsymbol{\theta})$. $\boldsymbol{\theta}$ and $\boldsymbol{\beta}$ are related through equation (2.1.11). Numerical integration of (2.2.8) is performed dividing the interval $\chi \in [0, \chi_s]$ in N_l equally spaced steps, each of size $\Delta = \chi_s / N_l$ and using a first order explicit method

$$\int_0^{\chi_s} f(\chi)d\chi = \Delta \sum_{i=1}^{N_l} f(\chi_k) + O\left(\frac{1}{N_l}\right) \tag{3.2.1}$$

$$\chi_k = k\Delta \tag{3.2.2}$$

In this notation, f is a generic function of χ and can be identified with either $\boldsymbol{\beta}$ or $\mathbf{A}$. Before applying the numerical integration method to (2.1.11), it is convenient to rewrite the geodesic equation as an equation for $\boldsymbol{\beta} = \mathbf{x}_\perp/\chi$

$$\frac{d^2}{d\chi^2}(\chi\boldsymbol{\beta}(\chi)) = \frac{2}{\chi}\nabla_{\boldsymbol{\beta}}\Phi(\chi, \boldsymbol{\beta}(\chi)) \tag{3.2.3}$$

We promoted the $\mathbf{x}_\perp$ dependency of Φ to a β dependency using $\Phi(\chi, \mathbf{x}_\perp = \chi\boldsymbol{\beta}) \to \Phi(\chi, \boldsymbol{\beta})$. Equation (3.2.3) is equivalent to

$$\frac{d^2\boldsymbol{\beta}(\chi)}{d\chi^2} + \frac{2}{\chi}\frac{d\boldsymbol{\beta}(\chi)}{d\chi} - \frac{2}{\chi^2}\nabla_{\boldsymbol{\beta}}\Phi(\chi, \boldsymbol{\beta}(\chi)) = 0 \tag{3.2.4}$$

Now let us consider an intermediate discrete step k and introduce the compact notation

$$f_k \equiv f(\chi_k) \quad ; \quad f'_k \equiv \left.\frac{df}{d\chi}\right|_{\chi=\chi_k} \quad ; \quad f''_k \equiv \left.\frac{d^2f}{d\chi^2}\right|_{\chi=\chi_k} \tag{3.2.5}$$

We define

$$\boldsymbol{\alpha}_k = \frac{2\Delta}{\chi_k}\nabla_{\boldsymbol{\beta}}\Phi(\chi_k, \boldsymbol{\beta}_k). \tag{3.2.6}$$

Using the first order finite difference approximations for the $\boldsymbol{\beta}$ derivatives

$$\boldsymbol{\beta}'_k = \frac{\boldsymbol{\beta}_{k+1} - \boldsymbol{\beta}_{k-1}}{2\Delta} + O(\Delta^2) \quad ; \quad \boldsymbol{\beta}''_k = \frac{\boldsymbol{\beta}_{k+1} + \boldsymbol{\beta}_{k-1} - 2\boldsymbol{\beta}_k}{\Delta^2} + O(\Delta^2), \tag{3.2.7}$$

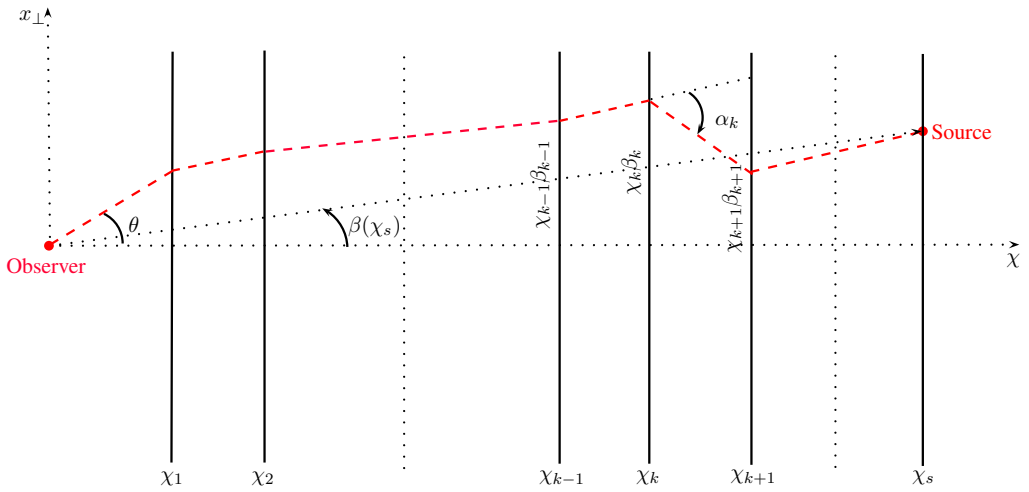

Figure 3.1: Multi–lens–plane algorithm schematics: the trajectory of a single light ray from the observer to the source at χ_s is shown in red as it undergoes the multiple deflections caused by the lensing effect.

we can rewrite equation (3.2.4) as

$$\frac{\boldsymbol{\beta}_{k+1} + \boldsymbol{\beta}_{k-1} - 2\boldsymbol{\beta}_k}{\Delta^2} + \frac{\boldsymbol{\beta}_{k+1} - \boldsymbol{\beta}_{k-1}}{\chi_k \Delta} - \frac{\boldsymbol{\alpha}_k}{\chi_k \Delta} = 0 \tag{3.2.8}$$

Once we solve (3.2.8) for $\boldsymbol{\beta}_{k+1}$, we immediately find

$$\boldsymbol{\beta}_{k+1} = \frac{2\boldsymbol{\beta}_k \chi_k - (\chi_k - \Delta)\boldsymbol{\beta}_{k-1} + \Delta \boldsymbol{\alpha}_k}{\chi_k + \Delta} \tag{3.2.9}$$

The expression (3.2.9) has a simple physical interpretation that we can understand by looking at the diagram in Figure 3.1. If we want to calculate the angular position of a light ray at the $k+1$-th step, we need to know its position at the two previous steps $k, k-1$. Simple geometric arguments, combined with the small deflection assumption, tell us that

$$\boldsymbol{\beta}_{k+1} = \frac{1}{\chi_{k+1}} \left[(\chi\boldsymbol{\beta})_k + \left(\frac{(\chi\boldsymbol{\beta})_k - (\chi\boldsymbol{\beta})_{k-1}}{\chi_k - \chi_{k-1}} + \boldsymbol{\alpha}_k \right) (\chi_{k+1} - \chi_k) \right] \tag{3.2.10}$$

Note that equations (3.2.9) and (3.2.10) are equivalent if the steps are equally spaced, which is the case in our integration scheme defined by $\chi_k = k\Delta$. This equivalence tells us that the quantity $\boldsymbol{\alpha}_k$, which is proportional to the gradient of the potential as stated in (3.2.6), is the deflection angle that a light ray experiences upon impact with a two dimensional lens plane of thickness Δ positioned at a longitudinal distance χ_k. This is why the procedure of solving (3.2.4) in discrete χ steps takes the name of multi–lens–plane algorithm [17, 18]. The solution is obtained by summing up a discrete set of trajectory deflections $\boldsymbol{\alpha}_k$ which are caused by a discrete set of two dimensional lens planes. Each plane is characterized by a lensing potential which is the three dimensional gravitational potential Φ projected along the longitudinal direction. We observe that equation (3.2.6) is essentially the discrete longitudinal integral of $\nabla_\perp \Phi$ performed with a step of size Δ. Using the initial conditions

$$\boldsymbol{\beta}_0 = \boldsymbol{\beta}_1 = \boldsymbol{\theta} \tag{3.2.11}$$

we can use the recurrence relation (3.2.9) to compute the light ray trajectory from the observed to the starting angle $\boldsymbol{\beta}_s$. It turns out that, because the coefficient that multiplies $\boldsymbol{\beta}_k$ in (3.2.9), $2\chi_k/(\chi_k + \Delta)$ is usually bigger than 1, this explicit method of solution leads to roundoff errors which blow up exponentially in k. To keep the accuracy of the geodesic solver under control we recast (3.2.9) in a slightly different form by defining $\delta\boldsymbol{\beta}_k \equiv \boldsymbol{\beta}_k - \boldsymbol{\beta}_{k-1}$. It is straightforward to show that

$$\boldsymbol{\beta}_k = \boldsymbol{\theta} + \sum_{i=1}^{k} \delta\boldsymbol{\beta}_i \tag{3.2.12}$$

$$\delta\boldsymbol{\beta}_{k+1} = \left(\frac{\chi_k - \Delta}{\chi_k + \Delta}\right)\delta\boldsymbol{\beta}_k + \left(\frac{\Delta}{\chi_k + \Delta}\right)\boldsymbol{\alpha}_k \tag{3.2.13}$$

It turns out that, because the coefficients that multiply $\delta\boldsymbol{\beta}, \boldsymbol{\alpha}$ are smaller than 1, (3.2.12) and (3.2.13) offer a more accurate numerical solution to the geodesic equation (3.2.4). We can solve the geodesic equation for light rays with different initial conditions $\boldsymbol{\theta}$, and study how the solution varies with $\boldsymbol{\theta}$. This allows to translate the recurrence relations (3.2.12), (3.2.13) into recurrence relations for the lensing Jacobian $\mathbf{A}$. Observing that

$$\frac{\partial(\alpha_i)_k}{\partial\theta_j} = \frac{2\Delta}{\chi_k}\partial_{\beta_i}\partial_{\beta_l}\Phi(\chi_k, \boldsymbol{\beta}_k)\frac{\partial(\beta_l)_k}{\partial\theta_j}, \tag{3.2.14}$$

we define the projected tidal field

$$\mathbf{T}_k = 2\chi_k\Delta\mathbf{T}^{\Phi}(\chi_k, \boldsymbol{\beta}_k). \tag{3.2.15}$$

The recurrence relations for the Jacobian $\mathbf{A}$ can then be written as

$$\mathbf{A}_k = \mathbb{1}_{2\times 2} + \sum_{i=1}^{k} \delta\mathbf{A}_i \tag{3.2.16}$$

$$\delta\mathbf{A}_{k+1} = \left(\frac{\chi_k - \Delta}{\chi_k + \Delta}\right)\delta\mathbf{A}_k + \left(\frac{\Delta}{\chi_k + \Delta}\right)\mathbf{T}_k\mathbf{A}_k \tag{3.2.17}$$

The recurrence relations (3.2.16),(3.2.17) are used to estimate the WL quantities $\kappa_s, \boldsymbol{\gamma}_s$ at an arbitrary angle $\boldsymbol{\theta}$ on the sky in $O(N_l)$ time. The set of discrete deflections $\boldsymbol{\alpha}_k$ and tidal distortions $\mathbf{T}_k$ are calculated from the potential Φ. In the next sub–section we will describe the numerical methods necessary to solve the Poisson equation (2.1.12) that relates the

potential Φ to the matter density contrast δ.

3.2.2 Poisson solver

The ray deflections and tidal distortions experienced after each lens crossing are determined by the density fluctuations which are responsible for the WL effect. We define the two–dimensional projected potential ψ for a lens plane centered at comoving distance χ with thickness Δ as

$$\psi(\chi, \boldsymbol{\beta}) = \frac{2}{\chi} \int_{\chi-\Delta/2}^{\chi+\Delta/2} d\chi' \Phi(\chi', \boldsymbol{\beta}) \tag{3.2.18}$$

Using the definition in (3.2.18), we obtain expressions for the deflections and tidal distortions in terms of ψ

$$\boldsymbol{\alpha}_k = \nabla_{\boldsymbol{\beta}} \psi(\chi_k, \boldsymbol{\beta}_k) \tag{3.2.19}$$

$$\mathbf{T}_k = \nabla_{\boldsymbol{\beta}} \nabla_{\boldsymbol{\beta}}^T \psi(\chi_k, \boldsymbol{\beta}_k) \tag{3.2.20}$$

Inserting (3.2.18) into the Poisson equation (2.1.12) we observe that ψ itself satisfies a Poisson–like equation

$$\nabla_{\boldsymbol{\beta}}^2 \psi(\chi, \boldsymbol{\beta}) = \frac{2}{\chi} \int_{\chi-\Delta/2}^{\chi+\Delta/2} d\chi' \chi'^2 \left(\nabla^2 - \frac{\partial^2}{\partial \chi'^2} \right) \Phi(\chi', \chi' \boldsymbol{\beta}) \tag{3.2.21}$$

In approximating $\nabla_{\boldsymbol{\beta}}^2 \approx \chi^2 (\nabla^2 - \partial_\chi^2)$ we made an assumption of small Δ, so that we can neglect the time evolution of Φ within the lens. If Δ is small we can also treat the ∂_χ^2 term in the integral as a boundary term, which vanishes when appropriate boundary conditions for the Poisson equation are imposed (we can choose periodic boundary conditions as an

example). With the help of (2.1.12) we obtain

$$\nabla^2_{\boldsymbol{\beta}}\psi(\chi,\boldsymbol{\beta}) = -\sigma(\chi,\boldsymbol{\beta}) \tag{3.2.22}$$

$$\sigma(\chi,\boldsymbol{\beta}) = \frac{8\pi G\chi a(\chi)^2\Delta}{c^2}\bar{\rho}_m(\chi)\delta(\chi,\chi\boldsymbol{\beta}) = \frac{3H_0^2\Omega_m\chi\Delta}{c^2 a(\chi)}\delta(\chi,\chi\boldsymbol{\beta}) \tag{3.2.23}$$

The dimensionless surface density σ which appears in (3.2.23) can be estimated from the outputs of N–body simulations using a particle number count histogram which measures the density contrast δ. The N–body outputs consist in a list of N_p particle positions $\{(x_p, y_p, z_p)\}$ computed at times $t(\chi_k)$. Let us assume without loss of generality that z is the longitudinal direction and (x, y) are the transverse coordinates. We divide the lens plane in a two–dimensional regularly spaced grid $\{(x_i, y_i)\}$ in the transverse direction. The grid has L_P pixels per side, each of comoving size size L_b/L_P. We assign to each pixel on the grid a particle number count

$$n(\chi,\boldsymbol{\beta}_i) = \sum_{p=1}^{N_p} w_n(\mathbf{x}_p,\chi,\boldsymbol{\beta}_i) \tag{3.2.24}$$

where

$$w_n(\mathbf{x}_p,\chi,\boldsymbol{\beta}_i) = \begin{cases} 1 \;\; \text{if} \;\; (x_p, y_p) \text{ in } \chi\boldsymbol{\beta}_i \,,\; z_p \in [\chi - \Delta/2, \chi + \Delta/2] \\ 0 \;\; \text{otherwise} \end{cases} \tag{3.2.25}$$

We then estimate the density contrast δ at each grid pixel from the histogram as

$$\delta(\chi, \chi\boldsymbol{\beta}_i) = \frac{n(\chi, \boldsymbol{\beta}_i) L_b L_P^2}{\Delta N_p} - 1 \tag{3.2.26}$$

We assigned the same mass $m = \Omega_m \rho_c L_b^3 / N_p$ to all the particles in the simulation. Once the density contrast is estimated from the N–body outputs, the two dimensional Poisson equation (3.2.22) can be solved on the regular transverse grid, at each of the discrete time steps χ_k. If we impose periodic boundary conditions on the edges of the lens plane, an efficient solution to (3.2.22) can be obtained using the FFTs of ψ and σ. Note that, because both of these quantities are real, a real FFT is sufficient. Inverting the laplacian operator in Fourier space yields the relation

$$\tilde{\psi}(\chi_k, \boldsymbol{\ell}) = \tilde{\sigma}(\chi_k, \boldsymbol{\ell}) \frac{e^{-\ell^2 \theta_G^2 / 2}}{\ell^2} \tag{3.2.27}$$

We applied a Gaussian smoothing smoothing factor $e^{-\ell^2 \theta_G^2 / 2}$ to the solution (3.2.27) in order to suppress sub–pixel particle shot noise. We chose θ_G to be the angular size of one lens pixel in real space. The time complexity of the potential calculation from the N–body outputs is dominated by the Poisson solver [24], which has a runtime of $O(L_P^2 \log L_P)$. Figure 3.2 shows an example lens (density and potential) plane based on equations (3.2.26), (3.2.27).

3.2.3 Cosmic variance sampling

The multi–lens–plane integration scheme for equation (2.2.9) suggests a way of producing multiple WL image realizations starting from a single N–body simulation. This is possible thanks to the fact that the size of the box L_b can be chosen to be big enough so that the field of view spanned by the observed ray positions $\boldsymbol{\theta}$ covers the simulation box only partially,

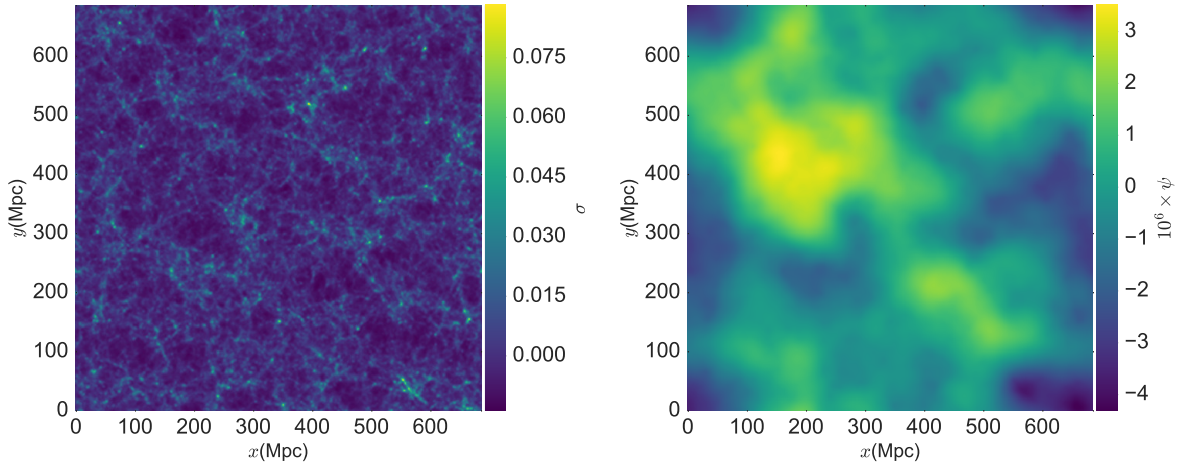

Figure 3.2: Dimensionless density σ (left) and corresponding potential ψ for a lens plane at $z_l = 0.7$, cut from a $N_p = 512^3, L_b = 240\,\mathrm{Mpc}/h$ N–body simulation.

$\chi_k\theta < L_b$. Periodic shifts of the lens planes along directions perpendicular to the line of sight yield different lenses with identical statistical properties, and lead to different realizations of $\kappa, \boldsymbol{\gamma}$ images. For each realization, the lens system is constructed according to the following procedure:

- Consider a discrete step χ_k and choose a random N–body simulation among a set of N_s independent simulations ($N_s = 1$ if only one N–body simulation has been run)
- Choose a random direction between $(\hat{x}, \hat{y}, \hat{z})$ to be the longitudinal direction. The other two directions will be the transverse coordinates $\mathbf{x}_\perp$
- Cut a random slice of size Δ from the N–body output at $t(\chi_k)$, along the chosen longitudinal direction
- Calculate the surface density contrast σ_k on the slice and solve the Poisson equation (3.2.22)

- Periodically shift the lens along the transverse directions by a random amount
- Repeat the steps for the next lens plane at distance χ_{k+1}

We follow this prescription to recycle the outputs of N_s independent N–body simulations and to produce $N_r \gg N_s$ realizations of WL observables. These simulated WL ensembles can be used to estimate the estimator scatters caused by cosmic variance, as well as estimator means. Because N_r is bigger than N_s, these WL realizations are pseudo–independent, but can be treated as effectively independent if N_r is not too large. This approximate independence issue, along with its implications on WL observation analysis, has been investigated in [25] and will be one of the topics in Chapter 5.

3.3 Approximate methods

In this section we describe the numerical implementation of the approximate methods shown in (2.2.13), (2.2.19) and (2.2.20). These methods provide us with a recipe to compute the Born contribution and first post–Born corrections to the convergence κ as line–of–sight integrals on the unperturbed ray trajectories.

3.3.1 Born approximation

The Born contribution to κ for sources at distance χ_s involves a single integral over χ and can be readily obtained using the first order method in (3.2.1). At $O(\Delta)$ precision we can write

$$\kappa_s^{(1)}(\boldsymbol{\theta}) = -\Delta \sum_{k=1}^{N_l} W_{ks}\chi_k \nabla_\perp^2 \Phi(\chi_k, \chi_k\boldsymbol{\theta}) \tag{3.3.1}$$

where we introduced the compact notation $W_{kk'} = 1 - \chi_k/\chi_{k'}$. Using the relations (3.2.18) and (3.2.22), we can relate the first order convergence $\kappa^{(1)}$ to the discrete set of dimensionless lens densities $\{\sigma_k \equiv \sigma(\chi_k, \chi_k\boldsymbol{\theta})\}$ as

$$\kappa_s^{(1)} = \frac{1}{2}\sum_{k=1}^{N_l} \sigma_k W_{ks} \tag{3.3.2}$$

Note that not only the Born–approximated convergence can be efficiently computed in $O(N_l)$ time, but such approximate approach does not even require knowledge of the solution to the Poisson equation (3.2.22). At linear order in the potential Φ, the shear field $\boldsymbol{\gamma}$ can be calculated from the Born–approximated κ via the use of the KS relation (2.2.27).

3.3.2 Post–Born corrections

The evaluation of the second order corrections to κ that appear in equations (2.2.19) and (2.2.20) involve two integrals over χ. This computation, if implemented naively, leads to an $O(N_l^2)$ runtime algorithm. When we apply the first order method in (3.2.1) twice we obtain

$$\kappa_s^{(2-\mathrm{ll})} = -\frac{1}{2}\sum_{k=1}^{N_l}\sum_{m=1}^{k} W_{ks} W_{mk} \mathrm{Tr}(\mathbf{T}_m \mathbf{T}_k) \tag{3.3.3}$$

$$\kappa_s^{(2-\mathrm{gp})} = \frac{1}{2}\sum_{k=1}^{N_l}\sum_{m=1}^{k} W_{ks} W_{mk} (\boldsymbol{\alpha}_m \cdot \nabla \sigma_k) \tag{3.3.4}$$

Note that, since we are performing the integrals along unperturbed trajectories, the angular arguments of $\sigma_k, \boldsymbol{\alpha}_k, \mathbf{T}_k$ are fixed to be $\boldsymbol{\beta}_k \equiv \boldsymbol{\theta}$ for each light ray. Note also that the gradient in (3.3.4) is taken in the angular coordinates. As previously stated, the naive implementation defined by (3.3.3) and (3.3.4) leads to an $O(N_l^2)$ runtime, which can be

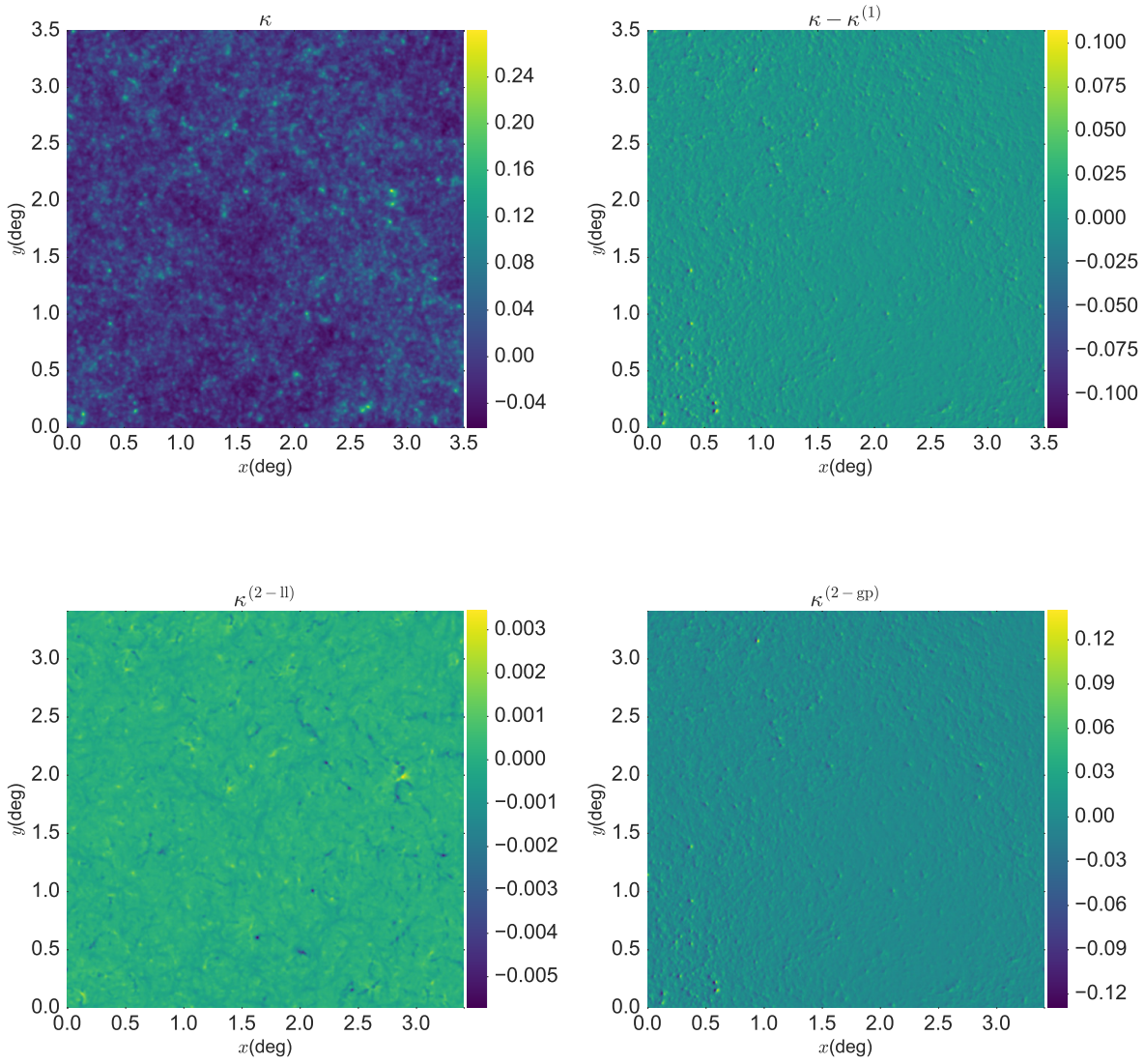

Figure 3.3: Sample κ reconstruction from one N–body simulation with $L_b = 260\,\mathrm{Mpc}/h$ and $N_p = 512^3$. The lens planes have a thickness of $\Delta = L_b/3$ and are resolved with $L_P^2 = 4096^2$ pixels. The κ maps are reconstructed with 2048^2 light rays arranged in a regular grid. The source galaxies are placed at redshift $z_s = 2$. The residuals $\kappa - \kappa^{(1)}$ are dominated by the geodesic term $\kappa^{(2-\mathrm{gp})}$.

quite inefficient if the number of lenses and light rays is large. We can design a more efficient algorithm, which runs in linear time, if we cache the partial sums

$$\begin{aligned} I_k^{\boldsymbol{\alpha},0} &= \textstyle\sum_{m=1}^{k} \boldsymbol{\alpha}_m \quad ; \quad I_k^{\boldsymbol{\alpha},1} = \sum_{m=1}^{k} \chi_m \boldsymbol{\alpha}_m \\ I_k^{\mathbf{T},0} &= \textstyle\sum_{m=1}^{k} \mathbf{T}_m \quad ; \quad I_k^{\mathbf{T},1} = \sum_{m=1}^{k} \chi_m \mathbf{T}_m \end{aligned} \tag{3.3.5}$$

The cached algorithm runs in linear time, as can be seen in the following relations

$$\kappa_s^{(2-\mathrm{ll})} = -\frac{1}{2} \sum_{k=1}^{N_l} W_{ks} \mathrm{Tr} \left[\mathbf{T}_k \left(I_k^{\mathbf{T},0} - \frac{I_k^{\mathbf{T},1}}{\chi_k} \right) \right] \tag{3.3.6}$$

$$\kappa_s^{(2-\mathrm{gp})} = \frac{1}{2} \sum_{k=1}^{N_l} W_{ks} \nabla \sigma_k \cdot \left(I_k^{\boldsymbol{\alpha},0} - \frac{I_k^{\boldsymbol{\alpha},1}}{\chi_k} \right) \tag{3.3.7}$$

Figure 3.3 shows a sample κ reconstruction from one N–body simulation, including the full ray–tracing map and a comparison between the residuals $\kappa - \kappa^{(1)}$ and the second order terms $\kappa^{(2-\mathrm{ll})}, \kappa^{(2-\mathrm{gp})}$.

3.4 The LensTools software package

In this section we present LensTools[24], a PYTHON software package that we developed in order to efficiently handle the WL operations discussed in this Chapter.

LensTools implements pipeline of operations which allow to produce simulated $\kappa, \boldsymbol{\gamma}$ images starting from a set of ΛCDM parameters (see Chapter 1). The sequence of operations in the pipeline is described by the diagram in Figure 3.4 The LensTools pipeline glues together the CAMB, N-GenIC and Gadget2 public codes, used in the N–body simulations, with PYTHON code. The Φ calculations and ray–tracing operations are also

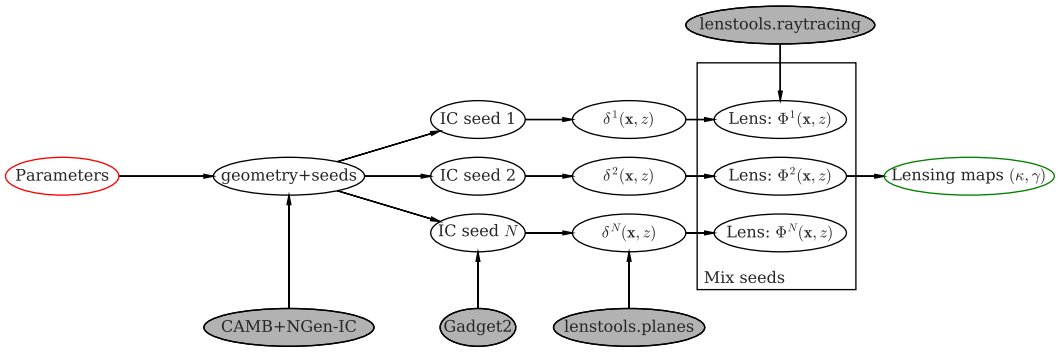

Figure 3.4: Scheme of the `LensTools` pipeline flow. Vertical arrows are directed from a particular application to its input. Horizontal arrows are directed from the input to the output products.

implemented in PYTHON. The solution to the Poisson equation (3.2.22) can be efficiently found via FFT, which `LensTools` performs using the NUMPY FFTPack [26]. The ray–tracing operations (3.2.12), (3.2.13), (3.2.16), (3.2.17) are also efficiently implemented with NUMPY taking advantage of vectorized linear algebra routines. `LensTools` also provides efficient implementations of the second order approximate methods for κ, which are defined by equations (3.3.2), (3.3.6) and (3.3.7).

Table 3.1 shows CPU time benchmarks for a test run performed on the XSEDE Stampede computer cluster (see `https://portal.xsede.org/tacc-stampede`). The N_p particles in each snapshot are divided between N_t files, which are read in parallel by N_t independent tasks. After the particle counting procedure (3.2.24) is performed by each task on the regular grid, the total surface density (calculated on a plane of L_P^2 pixels) is assembled by the master task, which then proceeds with the solution the Poisson equation

Step	Complexity	Test case	Runtime
Lens plane generation			
N–body input[1]	$O(N_p/N_t)$	$N_p = 512^3$, $N_t = 16$	2.10 s
Density estimation (3.2.24)	$O(N_p/N_t)$	$N_p = 512^3$, $N_t = 16$	0.20 s
MPI Communication	$O(L_P^2 \log N_t)$	$N_t = 16$, $L_P = 4096$	0.76 s
Poisson solver (3.2.27)	$O(L_P^2 \log L_P)$	$L_P = 4096$	2.78 s
Lens plane output	$O(L_P)$	$L_P = 4096$	0.04 s
Ray tracing			
Lens plane input	$O(L_P^2)$	$L_P = 4096$	0.32 s
Random plane shift	$O(L_P)$	$L_P = 4096$	0.15 s
$\boldsymbol{\alpha}_k, \mathbf{T}_k$ calculations (3.2.19),(3.2.20)	$O(N_R)$	$N_R = 2048^2$	1.54 s
Tensor products $\mathbf{T}_k\mathbf{A}_k$ in (3.2.17)	$O(N_R)$	$N_R = 2048^2$	1.29 s

Table 3.1: Ray–tracing operation benchmarks (see [24]). The numbers refer to tests conducted on the XSEDE Stampede cluster. Parallel operations are implemented with `mpi4py` [27], a PYTHON wrapper of the MPI library [28].

via FFT according to (3.2.27). The ψ outputs are then saved to disk. In a subsequent step, the lensing potential files are read from disk, and the geodesic equation (3.2.4) is solved for N_R different observed ray positions $\boldsymbol{\theta}$. This leads to the reconstruction of the WL shear $\boldsymbol{\gamma}$ and convergence κ profiles in the field of view spanned by $\boldsymbol{\theta}$. Multiple $\kappa, \boldsymbol{\gamma}$ realizations can be obtained with the sampling procedure described in § 3.2.3. Figure 3.5 shows the memory load as a function of the runtime for the plane generation and ray–tracing operations for the same test case shown in Table 3.1. The plot shows that, for the considered test case, computer clusters with at least 2 GB of memory per core are suitable for safely handling the `LensTools` operations (for this test case) without exhausting the resources.

The pipeline products are organized in a hierarchical directory structure whose levels correspond to specifications of ΛCDM cosmological parameters, choices of L_b, N_p, random seeds for the initial conditions $\tilde{\delta}(\mathbf{k})$ and choices of the lens plane parameters

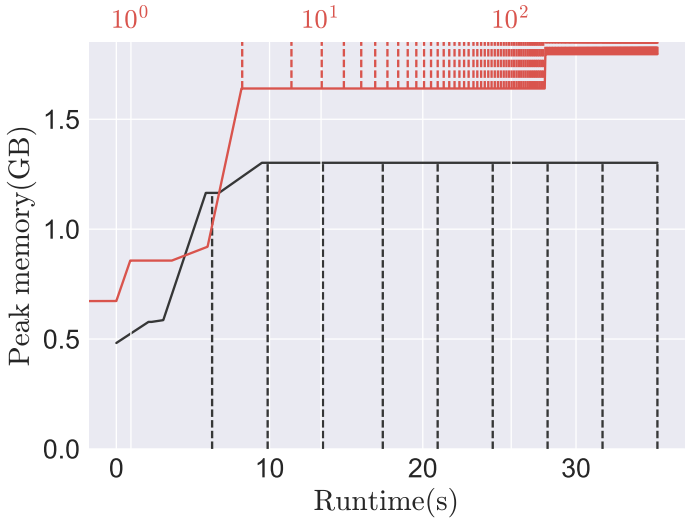

Figure 3.5: Memory load as a function of runtime for plane generation (black) and ray–tracing operations (red). Each vertical line corresponds to the completion of a ψ plane calculation (black) and a lens crossing during ray–tracing (red).

L_P, Δ. Separate directory tree levels are dedicated to the WL products $\kappa, \boldsymbol{\gamma}$. Both single redshift images and shear catalogs can be produced. `LensTools` provides an API to initialize, navigate and update the pipeline directory tree in a clean and efficient way, thus allowing easy retrieval of WL simulation products for further post–processing. For a throughout presentation of `LensTools`, we direct the reader to the code documentation at `http://lenstools.rtfd.io`.

Chapter 4

Shear image features

In this Chapter we describe how we can compress the high dimensional information contained in shear and convergence images into lower dimensional summary statistics (which we call *features* throughout the remainder of this work). These image features will then be used to infer the values of the ΛCDM parameters which describe our Universe. We focus our analysis on the two–dimensional κ images which can be generated with the ray–tracing simulations described in Chapter 3. The images span a square field of view of size $\theta^2_{\rm FOV}$ and, within the limits of the sampling procedure described in § 3.2.3, are independent from each other. Because of the stochastic nature of WL observables (which is due to cosmic variance), information on cosmology is inferred from ensemble averaged quantities $\langle f(\hat{\kappa})\rangle$, where f is a generic function of κ and the expectation value $\langle\rangle$ is taken over independent WL realizations. A two–dimensional Gaussian field is completely characterized, from a statistical point of view, in terms of quadratic image features, such as the field two–point correlation function or the its angular power spectrum. Since WL traces the statistical properties of the density contrast δ, whose evolution is controlled by non–linear

equations, WL observables cannot be modeled as Gaussian random fields. There is hence a possibility that cosmological information leaks from quadratic features into higher order statistics. In this work we consider two types of image features. One possibility consists of real space features, which have to do with the morphology of the image and can be expressed in terms of expectation values of local estimators. The second type of features are defined in Fourier space. We focus on the angular κ power spectrum, a non–local feature that encodes quadratic spatial correlations of the κ profile. In this Chapter we examine the relevant properties, advantages and drawbacks of these image features.

4.1 Local expectation values in real space

Knowledge of the angular profile $\hat{\kappa}(\boldsymbol{\theta})$, combined with the statistical isotropy assumption, allows us to estimate ensemble averages $\langle\rangle$ as real space spatial averages according to

$$\langle f(\hat{\kappa})\rangle = \frac{1}{\theta^2_{\rm FOV}} \int_{\rm FOV} d\boldsymbol{\theta} f(\hat{\kappa})(\boldsymbol{\theta}) \tag{4.1.1}$$

In this section we describe a systematic way to relate expectation values of local estimators to the connected moments of κ, following the derivation given in [29]. Since the estimators considered in this Chapter contain at most second order spatial derivatives in κ, we can assume the most general one of them to be a function of the N–dimensional vector $\mathbf{K}$, formally defined by

$$\mathbf{K} = (\alpha, \boldsymbol{\eta}, \boldsymbol{\zeta}) = \frac{1}{\sigma_0}(\kappa, \nabla\kappa, \partial^2_x\kappa, \partial^2_y\kappa, \partial_x\partial_y\kappa) \tag{4.1.2}$$

We indicated the first and second derivative of the κ field as $\boldsymbol{\eta}$ and $\boldsymbol{\zeta}$ respectively. $\boldsymbol{\eta}, \boldsymbol{\zeta}$ are expressed in units of the variance of κ, $\sigma_0^2 = \langle \kappa^2 \rangle$. We assume $\langle \kappa \rangle = 0$ without loss of generality. The probability distribution of $\mathbf{K}$, $\mathcal{L}(\mathbf{K})$, and its characteristic function $Z(\mathbf{J})$ are related according to

$$Z(\mathbf{J}) = \left\langle e^{i\mathbf{J}\cdot\mathbf{K}} \right\rangle = \int d\mathbf{K} \mathcal{L}(\mathbf{K}) e^{i\mathbf{J}\cdot\mathbf{K}} \tag{4.1.3}$$

Note that, using the definition (4.1.3), the expectation value of any polynomial $K_{i_1}...K_{i_n}$ can be calculated in terms of derivatives of Z using the expression

$$\langle K_{i_1}...K_{i_n} \rangle = \left[\left(-i \frac{\partial}{\partial J_{i_i}} \right) ... \left(-i \frac{\partial}{\partial J_{i_n}} \right) Z(\mathbf{J}) \right]_{\mathbf{J}=0} \tag{4.1.4}$$

Writing Z as an exponential of connected terms

$$Z(\mathbf{J}) = \exp\left(\sum_{n=2}^{\infty} \frac{i^n}{n!} M^{(n)}_{i_1...i_n} J_{i_1}...J_{i_n} \right), \tag{4.1.5}$$

we can readily identify $M^{(2)}$ as the covariance matrix of $\mathbf{K}$, because $\mathbf{M}^{(2)} = \langle \mathbf{K}\mathbf{K}^T \rangle$. For a Gaussian field, all $M^{(n)}$ with $n > 2$ vanish, and the correlations (4.1.4) are easy to compute because the argument of the exponential in (4.1.5) has only one term. If $\mathbf{K}$ is non–Gaussian, like in the WL case, perturbative approaches to the calculation of (4.1.4) can be attempted if the connected moments $\mathbf{M}^{(n)}$ do not grow too fast with n. The perturbative series is obtained from the inverse Fourier transform of Z after the $\mathbf{M}^{(2)}$ term has been factored out:

$$\mathcal{L}(\mathbf{K}) = \int \frac{d\mathbf{J}}{(2\pi)^N} \exp\left(-\frac{1}{2}\mathbf{J}^T\mathbf{M}^{(2)}\mathbf{J} - i\mathbf{J}\cdot\mathbf{K} \right) \exp\left(\sum_{n=3}^{\infty} \frac{i^n}{n!} M^{(n)}_{i_1...i_n} J_{i_1}...J_{i_n} \right) \tag{4.1.6}$$

Because multiplications in $\mathbf{J}$ space act as gradients in $\mathbf{K}$ space, and since we know how to perform Gaussian integrals analytically, we can convert (4.1.6) into

$$\mathcal{L}(\mathbf{K}) = \exp\left(\sum_{n=3}^{\infty} \frac{(-1)^n}{n!} M^{(n)}_{i_1 \ldots i_n} \partial_{K_{i_1}} \ldots \partial_{K_{i_n}}\right) \mathcal{L}_G(\mathbf{K}) \tag{4.1.7}$$

$$\mathcal{L}_G(\mathbf{K}) = \frac{1}{\sqrt{(2\pi)^N |\mathbf{M}^{(2)}|}} \exp\left(-\frac{1}{2}\mathbf{K}^T (\mathbf{M}^{(2)})^{-1} \mathbf{K}\right) \tag{4.1.8}$$

The expression (4.1.7) of the $\mathbf{K}$ likelihood in term of its connected moments also suggests that, in order to calculate the expectation value of a generic function $f(\mathbf{K})$, we can take advantage of integration by parts and write

$$\langle f(\mathbf{K}) \rangle = \left\langle \exp\left(\sum_{n=3}^{\infty} \frac{M^{(n)}_{i_1 \ldots i_n}}{n!} \partial_{K_{i_1}} \ldots \partial_{K_{i_n}}\right) f(\mathbf{K}) \right\rangle_G \tag{4.1.9}$$

where the expectation values $\langle\rangle_G$ are computed with the Gaussian probability distribution (4.1.8). Expanding the exponential in (4.1.9) in a power series leads to a perturbative expansion for the expectation value $\langle f(\mathbf{K}) \rangle$ in terms of the connected moments $M^{(n)}$. The series has a chance to converge if $\mathbf{M}^{(n)} \to 0$ as n grows, which could be the case for the κ maps examined in this work. Symmetry under rotations suggests that the covariance matrix $\mathbf{M}^{(2)}$ can be parametrized in terms of two parameters $\sigma_\eta^2 = \langle \eta^2 \rangle, \sigma_\zeta^2 = \langle (\zeta_{xx} + \zeta_{yy})^2 \rangle$ which appear in $\mathbf{M}^{(2)}$ according to the expression

$$\begin{gathered} \langle \alpha^2 \rangle = 1 \qquad ; \qquad \langle \alpha \boldsymbol{\eta} \rangle = \langle \boldsymbol{\eta} \boldsymbol{\zeta} \rangle = 0 \\ \langle \eta_i \eta_j \rangle = -\langle \alpha \zeta_{ij} \rangle = \frac{\sigma_\eta^2 \delta_{ij}}{2} \quad ; \quad \langle \zeta_{ij} \zeta_{kl} \rangle = \frac{\sigma_\zeta^2}{8} (\delta_{ij}\delta_{kl} + \delta_{ik}\delta_{jl} + \delta_{il}\delta_{jk}) \end{gathered} \tag{4.1.10}$$

A series expansion for local expectation values can be built from (4.1.9) once an assumption is made about the magnitude of the connected moments $\mathbf{M}^{(n)}$. Following [29], we will assume that $\mathbf{M}^{(n)} = O(\lambda^{n-2})$, where λ is a dimensionless parameter which describes small departures from Gaussianity. Note that, in order for the perturbation series to converge, λ needs to be small. Under this assumption, we can write the first few terms in the $\langle f \rangle$ expansion as

$$\langle f(\mathbf{K}) \rangle = \langle f(\mathbf{K}) \rangle_G + \langle f(\mathbf{K}) \rangle_3 + \langle f(\mathbf{K}) \rangle_4 + O(\lambda^3) \tag{4.1.11}$$

with

$$\langle f(\mathbf{K}) \rangle_3 = \frac{1}{6} \mathbf{M}^{(3)}_{\mathbf{i}} \left\langle \frac{\partial f(\mathbf{K})}{\partial K_{\mathbf{i}}} \right\rangle_G \tag{4.1.12}$$

$$\langle f(\mathbf{K}) \rangle_4 = \frac{1}{24} \mathbf{M}^{(4)}_{\mathbf{i}} \left\langle \frac{\partial f(\mathbf{K})}{\partial K_{\mathbf{i}}} \right\rangle_G + \frac{1}{12} \mathbf{M}^{(3)}_{\mathbf{i}} \mathbf{M}^{(3)}_{\mathbf{j}} \left\langle \frac{\partial^2 f(\mathbf{K})}{\partial K_{\mathbf{i}} \partial K_{\mathbf{j}}} \right\rangle_G \tag{4.1.13}$$

In equations (4.1.12), (4.1.13) we grouped individual $\mathbf{K}$ vector indexes in the multi–indexes $\mathbf{i}, \mathbf{j}$. Note that the quartic perturbation term (4.1.13) includes disconnected contributions $(\mathbf{M}^{(3)})^2$ which are of the same order as $\mathbf{M}^{(4)}$. In the next section we test the validity of this perturbative approach on morphological features of simulated κ images.

4.2 Minkowski Functionals

The Large Scale Structure of the cosmic density fluctuations is known to display prominent morphological features such as one dimensional filaments (see the structure in Figure 3.2 as an example). In the hope that a morphological description of κ contains valuable information about cosmology, we considered a class of two dimensional morphological descriptors

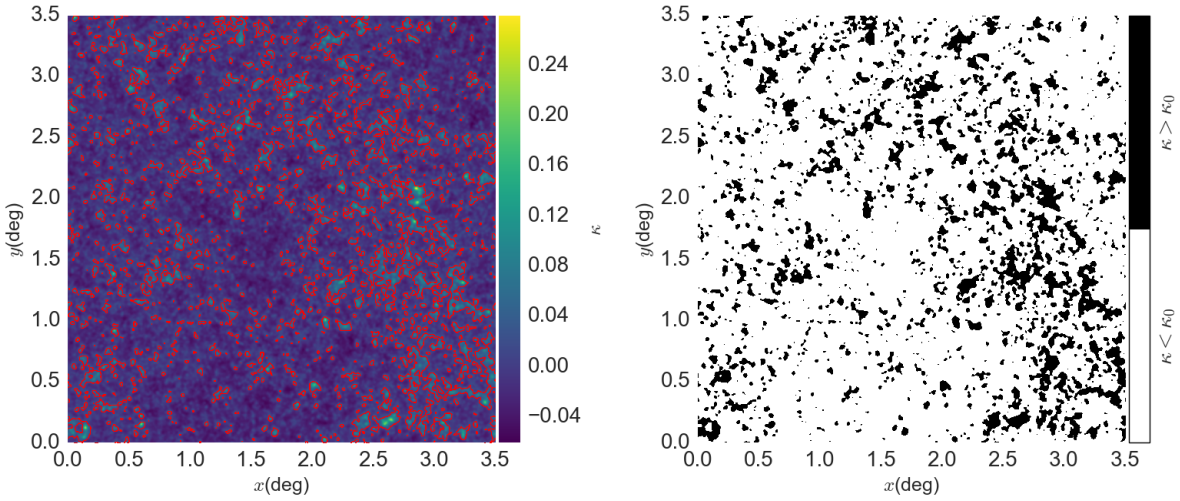

Figure 4.1: Example of a κ–excursion set (black, right panel) for a simulated field of view of size $\theta_{\rm FOV} = 3.5\,{\rm deg}$, with $\kappa_0 = 0.02$, referred to the image on the left panel. The $\kappa = 0.02$ iso–contours have been indicated in red. The sources have been placed at a constant redshift $z_s = 2$. The image has been convolved with a Gaussian kernel of size $\theta_G = 0.5'$.

known as Minkowski functionals (MFs) [30, 29, 31, 32, 33]. MFs of κ images are defined on the value–based spatial partitions of the image, commonly known as *excursion sets*. A κ_0–excursion set $\Sigma(\kappa_0)$ is defined to be the set of angular positions $\boldsymbol{\theta}$ for which $\kappa(\boldsymbol{\theta}) > \kappa_0$, as shown in Figure 4.1. The only three translation and rotation invariant morphological descriptors that can be measured from κ–excursion sets are the area V_0 of $\Sigma(\kappa_0)$, the length V_1 of its boundary $\partial\Sigma(\kappa_0)$, and its Euler characteristic V_2 [29]. For computational convenience, V_2 can be related to the geodesic curvature $\mathcal{K}$ of the excursion set boundary by the Gauss–Bonnet theorem. We can formally define the three MFs $V_k(\kappa_0)$ as

$$V_0(\kappa_0) = \int_{\Sigma(\kappa_0)} d\boldsymbol{\theta} \quad ; \quad V_1(\kappa_0) = \int_{\partial\Sigma(\kappa_0)} dl \quad ; \quad V_2(\kappa_0) = \int_{\partial\Sigma(\kappa_0)} \mathcal{K} dl \tag{4.2.1}$$

In equation (4.2.1), we indicated the line element on the boundary as dl. The definitions (4.2.1) emphasize the symmetry of the MFs under rotations, but do not offer a computationally convenient method to measure them. These definitions can be re–expressed, with some algebra, as area integrals of local quantities in the same form as equation (4.1.1). The area functional V_0 can be conveniently measured by thresholding the pixel values in the κ map:

$$V_0(\kappa_0) = \int d\boldsymbol{\theta}\Theta(\kappa(\boldsymbol{\theta}) - \kappa_0). \tag{4.2.2}$$

The perimeter functional can be expressed as an area integral with the help of integration by parts. The boundary of the excursion set $\partial\Sigma(\kappa_0)$, corresponds by definition to the set of points $\kappa \equiv \kappa_0$, which is orthogonal to the gradient $\nabla\kappa$. The normality condition allows us to find unit vectors which are tangent and normal to the boundary, which we call $\mathbf{t}, \mathbf{n}$. We can write

$$\mathbf{t} = \left(\frac{\partial_y\kappa}{|\nabla\kappa|}, -\frac{\partial_x\kappa}{|\nabla\kappa|}\right) \quad ; \quad \mathbf{n} = -\frac{\nabla\kappa}{|\nabla\kappa|} \tag{4.2.3}$$

It is easy to show, with the help of (4.2.3), that $\mathbf{t}\cdot\mathbf{n} = 0$ and that $\mathbf{n}$ points to the exterior of the excursion set. With a double integration by parts we can also show that

$$V_1(\kappa_0) = \int_{\partial\Sigma(\kappa_0)} \mathbf{n}\cdot\mathbf{n}dl = \int d\boldsymbol{\theta}\Theta(\kappa-\kappa_0)\nabla\cdot\mathbf{n} = \int d\boldsymbol{\theta}\delta^D(\kappa-\kappa_0)|\nabla\kappa| \tag{4.2.4}$$

Equation (4.2.4) yields a local estimator of the excursion boundary perimeter in terms of the gradient of κ. A similar procedure can be employed to compute the Euler functional V_2, taking advantage of the definition of the geodesic curvature $\mathcal{K}$ as the variation of the

tangent direction $\mathbf{t}$ across the boundary:

$$\frac{d\mathbf{t}}{dl} = \mathcal{K}\mathbf{n}. \tag{4.2.5}$$

Equation (4.2.5) leads to

$$\mathcal{K} = \frac{t_i t_j \partial_i \partial_j \kappa}{|\nabla \kappa|} \tag{4.2.6}$$

We now perform the double integration by parts, much like we did for (4.2.4), to get

$$V_2(\kappa_0) = \int d\boldsymbol{\theta} \delta^D(\kappa - \kappa_0) \left(\frac{2\partial_x \partial_y \kappa \partial_x \kappa \partial_y \kappa - \partial_x^2 \kappa (\partial_y \kappa)^2 - \partial_y^2 \kappa (\partial_x \kappa)^2}{|\nabla \kappa|^2} \right) \tag{4.2.7}$$

Equations (4.2.2), (4.2.4) and (4.2.7) provide practical estimators for measuring the morphological features V_k from an image by thresholding pixel values and measuring local κ gradients. In the next sub–section we will derive a relation between V_k and the real space moments of κ.

4.2.1 Relation with the moments of κ

The expectation value of the estimators defined in (4.2.2), (4.2.4) and (4.2.7) can be expressed as ensemble expectation values of functions of $\hat{\kappa}$ using equation (4.1.1). We can write

$$V_0(\kappa_0) = \theta^2_{\rm FOV}\langle\Theta(\hat{\kappa}-\kappa_0)\rangle$$

$$V_1(\kappa_0) = \theta^2_{\rm FOV}\langle\delta^D(\hat{\kappa}-\kappa_0)|\nabla\hat{\kappa}|\rangle \tag{4.2.8}$$

$$V_2(\kappa_0) = \theta^2_{\rm FOV}\left\langle\delta^D(\hat{\kappa}-\kappa_0)\frac{\hat{t}_i\hat{t}_j\partial_i\partial_j\hat{\kappa}}{|\nabla\hat{\kappa}|^2}\right\rangle$$

Taking advantage of statistical isotropy one can show that, for generic two–dimensional vector fields $\hat{\mathbf{u}},\hat{\mathbf{v}}$ consistent with this assumption, the following identities hold

$$\langle\hat{u}\rangle = \frac{\pi}{2}\langle|\hat{u}_x|\rangle \quad ; \quad \langle\hat{\mathbf{u}}\cdot\hat{\mathbf{v}}\rangle = \pi\langle|\hat{u}_x|\delta^D(\hat{u}_y)\hat{\mathbf{u}}\cdot\hat{\mathbf{v}}\rangle, \tag{4.2.9}$$

The relations (4.2.9), applied to (4.2.8) with $\mathbf{u}=\nabla\kappa$ and $v_i = \partial_i\partial_j\kappa\partial_j\kappa/|\nabla\kappa|^2$, lead to the expressions

$$V_0(\kappa_0) = \theta^2_{\rm FOV}\langle\Theta(\hat{\kappa}-\kappa_0)\rangle \tag{4.2.10}$$

$$V_1(\kappa_0) = \frac{\pi}{2}\theta^2_{\rm FOV}\langle\delta^D(\hat{\kappa}-\kappa_0)|\partial_x\hat{\kappa}|\rangle \tag{4.2.11}$$

$$V_2(\kappa_0) = -\pi\theta^2_{\rm FOV}\langle\delta^D(\hat{\kappa}-\kappa_0)\delta^D(\partial_y\hat{\kappa})|\partial_x\hat{\kappa}|\partial^2_y\hat{\kappa}\rangle \tag{4.2.12}$$

The parametrization (4.1.10) of the $\mathbf{K}$ covariance matrix allows to explicitly calculate expectation values of estimators f which are local in κ, such as (4.2.10), (4.2.11) and (4.2.12). As required in the series expansion (4.1.9), we need to calculate Gaussian expectation values of arbitrary $\alpha,\boldsymbol{\eta},\boldsymbol{\zeta}$ derivatives of the particular local estimator we are considering. Algebra on Gaussian integration leads to

$$\langle \partial_\alpha^n \Theta(\alpha-\nu)\rangle_G = \frac{(-1)^{n-1}}{\sqrt{2\pi}} e^{-\nu^2/2} H_{n-1}(\nu) \tag{4.2.13}$$

$$\langle \partial_\alpha^n \partial_{\eta_x}^m \delta^D(\alpha-\nu)|\eta_x|\rangle_G = \frac{H_{m-2}(0)}{\pi}\left(\frac{\sigma_\eta}{\sqrt{2}}\right)^{1-m} e^{-\nu^2/2} H_n(\nu) \tag{4.2.14}$$

$$\begin{gathered}\langle \partial_\alpha^k \partial_{\eta_y}^{l_1} \partial_{\eta_x}^{l_2} \partial_{\zeta_{yy}}^m \delta^D(\alpha-\nu)\delta^D(\eta_y)|\eta_x|\zeta_{yy}\rangle_G = \\ \frac{H_{l_1}(0)H_{l_2-2}(0)}{(2\pi)^{3/2}}\left(\frac{\sigma_\eta}{\sqrt{2}}\right)^{2-l_1-l_2-2m} e^{-\nu^2/2}[H_{k+1}(\nu)\delta_{m0} - H_k(\nu)\delta_{m1}]\end{gathered} \tag{4.2.15}$$

We defined the Hermite polynomials H_n as

$$H_{-1}(x) \equiv \sqrt{\frac{\pi}{2}} e^{x^2/2} \mathrm{erfc}\left(\frac{x}{\sqrt{2}}\right) \quad ; \quad H_n(x) \equiv e^{x^2/2}\left(-\frac{d}{dx}\right)^n e^{-x^2/2} \quad ; \quad H_{-2}(0) \equiv 1 \tag{4.2.16}$$

Expressions (4.2.13), (4.2.14) and (4.2.15), after some tedious algebra, lead to the perturbative relation between MFs and moments of κ

$$V_k(\kappa_0 = \sigma_0\nu) = A_k e^{-\nu^2/2}\left[V_k^G(\nu) + \delta V_k^1(\nu) + \delta V_k^2(\nu) + O(\lambda^3)\right] \tag{4.2.17}$$

In the notation introduced in equation (4.2.17), $V_k^G = H_{k-1}$ is the Gaussian contribution to the k–th MF and $\delta V_k^1, \delta V_k^2$ are the corrections coming respectively from the $O(\lambda)$, $O(\lambda^2)$ non–Gaussianity in κ. For reference, the amplitudes A_k are given by

$$A_0 = \frac{\theta_{\mathrm{FOV}}^2}{\sqrt{2\pi}} \quad ; \quad A_1 = \frac{\sigma_\eta \theta_{\mathrm{FOV}}^2}{2\sqrt{2}} \quad ; \quad A_2 = \frac{\sigma_\eta^2 \theta_{\mathrm{FOV}}^2}{\sqrt{8\pi}} \tag{4.2.18}$$

[34] performed the calculations up to order $O(\lambda^2)$ and found that the knowledge of seven

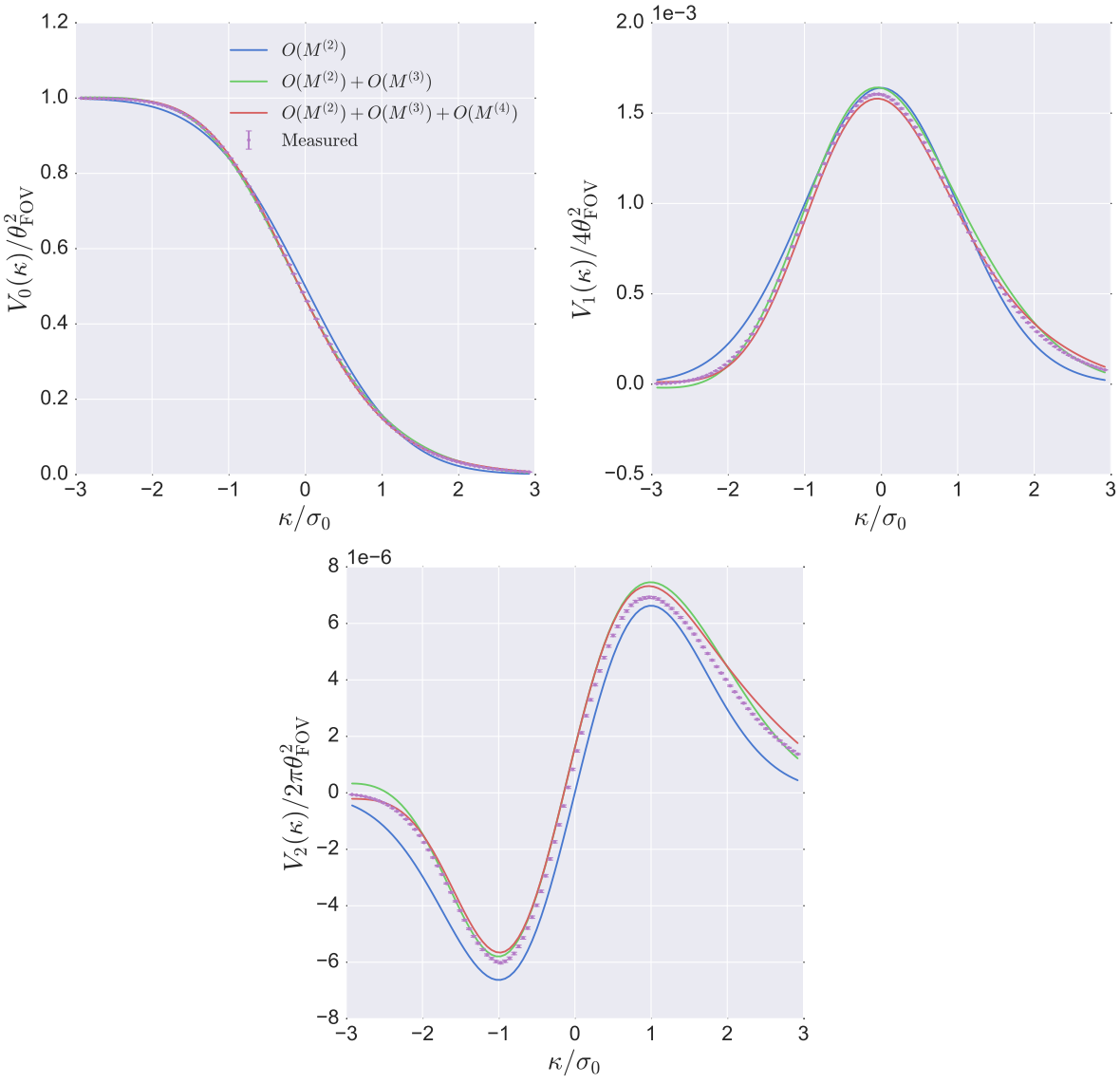

Figure 4.2: Comparison between the MFs measured from a sample of simulated fiducial κ maps (from the `IGS1` simulations, see Appendix) and the approximation based on perturbation theory up to order $O(\mathbf{M}^{(4)})$ (or $O(\lambda^2)$). We show the mean of the measured MFs calculated over 1000 κ realizations (simulated with constant source redshift $z_s = 1$ and smoothed with $\theta_G = 0.5'$) and the perturbative approach at Gaussian $O(\mathbf{M}^{(2)})$ order (blue) and including skewness $O(\mathbf{M}^{(3)})$ (green) and kurtosis $O(\mathbf{M}^{(4)})$ corrections. The moments $\boldsymbol{\mu}$ have also been measured from the mean of the same 1000 κ realizations.

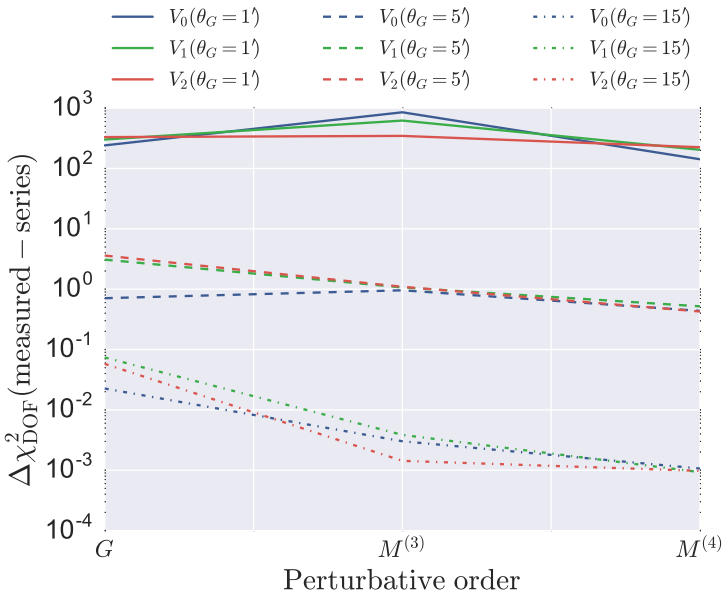

Figure 4.3: Study of the convergence of the perturbation series based on equation (4.2.17). We measure the degree of convergence using a $\Delta\chi^2$ metric defined as $\Delta\chi^2 = (V_k^{\mathrm{meas}} - V_k^{\mathrm{pert}})^T \mathbf{C}_{kk}^{-1} (V_k^{\mathrm{meas}} - V_k^{\mathrm{pert}})$, where V_k^{meas} are the measured MFs, V_k^{pert} are the approximated MFs at different orders in perturbation theory and $\mathbf{C}_{kk}$ is the $V_k - V_k$ covariance between different thresholds κ_0, measured from simulations. We show results for the area V_0 (blue), perimeter V_1 (green) and the Euler characteristic V_2 (red) of the excursion sets. Different line styles correspond to the different sized of the Gaussian smoothing windows θ_G applied to the images.

higher moments of κ is sufficient to calculate the corrections.

$$\mu_{30} = \frac{\langle \kappa^3 \rangle}{\sigma_0^3} \quad ; \quad \mu_{31} = -\frac{3}{4}\frac{\langle \kappa^2 \nabla^2 \kappa \rangle}{\sigma_0^3 \sigma_\eta^2} \quad ; \quad \mu_{32} = -3\frac{\langle |\nabla\kappa|^2 \nabla^2 \kappa \rangle}{\sigma_0^3 \sigma_\eta^4} \tag{4.2.19}$$

$$\begin{aligned} \mu_{40} &= \frac{\langle \kappa^4 \rangle_c}{\sigma_0^4} \qquad ; \quad \mu_{41} = \frac{\langle \kappa^3 \nabla^2 \kappa \rangle_c}{\sigma_0^4 \sigma_\eta^2} \\ \mu_{42} &= \frac{\langle \kappa |\nabla\kappa|^2 \nabla^2 \kappa \rangle_c}{\sigma_0^4 \sigma_\eta^4} \quad ; \quad \mu_{43} = \frac{\langle |\nabla\kappa|^4 \rangle_c}{2\sigma_0^4 \sigma_\eta^4} \end{aligned} \tag{4.2.20}$$

We use the subscript c to indicate the connected component of the quartic moments $\boldsymbol{\mu}_4$. The non–Gaussian corrections to the MFs can be expressed as

$$\delta V_k^1 = \frac{\mu_{30}}{6} H_{k+2} + \frac{k\mu_{31}}{3} H_k + \frac{k(k-1)\mu_{32}}{6} H_{k-2} \tag{4.2.21}$$

$$\begin{aligned} \delta V_0^2 &= \frac{\mu_{30}^2}{72} H_5 + \frac{\mu_{40}}{24} H_3 \\ \delta V_1^2 &= \frac{\mu_{30}^2}{72} H_6 + \left(\frac{\mu_{40} - \mu_{30}\mu_{31}}{24} \right) H_4 - \frac{1}{12} \left(\mu_{41} + \frac{3}{8}\mu_{31}^2 \right) H_2 - \frac{\mu_{43}}{8} \\ \delta V_2^2 &= \frac{\mu_{30}^2}{72} H_7 + \left(\frac{\mu_{40} - \mu_{30}\mu_{31}}{24} \right) H_5 \\ &\quad - \frac{1}{6} \left(\mu_{41} + \frac{\mu_{30}\mu_{32}}{2} \right) H_3 - \frac{1}{2} \left(\mu_{42} + 2\mu_{43} + \frac{\mu_{31}\mu_{32}}{2} \right) H_1 \end{aligned} \tag{4.2.22}$$

Figures 4.2,4.3 show comparisons between measured MFs from our simulated κ images (using estimators (4.2.2), (4.2.4) and (4.2.7)) and the $O(\lambda^2)$ perturbation series based on equations (4.2.21), (4.2.22). We can clearly observe a departure between the measured MFs profile and the moment–based approximation, even when non–Gaussian corrections up to $O(\lambda^2)$ are taken into account. Figure 4.3 clearly shows that the λ power series converges faster when a larger smoothing kernel is applied to the κ images, because of the mitigating

effect because of the reduced non–Gaussianity that results from the smoothing procedure. Large smoothing kernels, however, reduce the amount of information contained in WL data because they erase meaningful characteristics in the image features from which ΛCDM parameters are inferred. Because MFs and the first few moments of κ are not equivalent for small smoothing scales, morphological descriptors have the potential to carry cosmological information that moments, by themselves, are missing. This issue will be investigated further in Chapter 5.

4.3 Peak counts

In the previous section we showed how morphological features in κ maps are related to quadratic and higher–than–quadratic local moments of κ. In the limit of Gaussian fields, MFs are completely characterized in terms of the two quadratic moments σ_0, σ_η. If non–Gaussianity is present, on the other hand, MFs contain information on arbitrarily high order κ correlations. A similar reasonment can be applied to a different type of local κ feature, such as the statistics of local maxima (which we will call *peaks* from now on) counts. In this section we explore the usage of peak counts $N_{\rm pk}$ as an image feature. A κ peak of height κ_0 can be identified at a location $\boldsymbol{\theta}_p$ if the image gradient $\boldsymbol{\eta}$ vanishes and the Hessian matrix $\boldsymbol{\zeta}$ is positive definite at this location. Following [35], we define the peak angular density at an angular position $\boldsymbol{\theta}$ as

$$n_{\rm pk}(\boldsymbol{\theta}) = \sum_p \delta^D(\boldsymbol{\theta} - \boldsymbol{\theta}_p) = |\boldsymbol{\zeta}(\boldsymbol{\theta})| \delta^D(\boldsymbol{\eta}(\boldsymbol{\theta})) \tag{4.3.1}$$

In equation (4.3.1), the sum extends over all peaks in the map and the Jacobian determinant is defined as $|\boldsymbol{\zeta}| = \zeta_{xx}\zeta_{yy} - \zeta_{xy}^2$. If we are interested in knowing the expected number of

peaks of a certain height $\kappa_0 = \sigma_0\nu$ in a κ image, we have to calculate the expectation value of the local estimator

$$\frac{dN_{\rm pk}}{d\nu} = \theta_{\rm FOV}^2 \left\langle \delta^D(\alpha-\nu)\delta^D(\boldsymbol{\eta})|\boldsymbol{\zeta}|\Theta(|\boldsymbol{\zeta}|)\Theta({\rm Tr}\boldsymbol{\zeta})\right\rangle \tag{4.3.2}$$

The product of Θ functions in (4.3.2) ensures that the extremum of κ is actually a maximum and not a minimum or a saddle point. Note that we related the peak histogram to the expectation value of a local estimator, which can be calculated in perturbation series using (4.1.9) in the same fashion as we did for the MFs, although the calculation is more complicated. In this section, we will limit ourselves to finding an expression for $\frac{dN_{\rm pk}}{d\nu}$ at Gaussian order. For the sake of simplifying the calculations, it is useful to introduce a parametrization for $\boldsymbol{\zeta}$ in terms of three parameters t, u, ϕ as

$$\boldsymbol{\zeta} = -\sigma_\zeta \begin{pmatrix} \frac{x}{2} + x\epsilon\cos(2\phi) & x\epsilon\sin(2\phi) \\ x\epsilon\sin(2\phi) & \frac{x}{2} - x\epsilon\cos(2\phi) \end{pmatrix} \tag{4.3.3}$$

In this parametrization x, ϵ are scalars under rotations (because $\sigma_\zeta x = -{\rm Tr}\boldsymbol{\zeta}, \sigma_\zeta^2 x^2(1-4\epsilon^2)/4 = |\boldsymbol{\zeta}|$) and ϕ transforms as an angle shift. With the help of rotational symmetry and with the change of variable

$$u = \frac{\alpha - \gamma x}{\sqrt{1-\gamma^2}} \quad ; \quad \gamma = \frac{\sigma_\eta^2}{\sigma_\zeta}, \tag{4.3.4}$$

we can write the Gaussian part of the $\mathbf{K}$ likelihood (4.1.8) as

$$\mathcal{L}_G(\mathbf{K})d\mathbf{K} = \frac{8\epsilon x^2}{2\pi^3\sigma_\eta^2}\exp\left(-\frac{u^2+x^2}{2} - \frac{\eta^2}{\sigma_\eta^2} - 4x^2\epsilon^2\right) du dx d\boldsymbol{\eta} d\epsilon d\phi \tag{4.3.5}$$

The expectation value (4.3.2) can then be expressed in a more friendly way as

$$\left(\frac{dN_{\rm pk}}{d\nu}\right)_G = \frac{\theta_{\rm FOV}^2\sigma_\zeta^2}{4}\left\langle\delta^D\left(u\sqrt{1-\gamma^2}+\gamma x-\nu\right)\delta^D(\boldsymbol{\eta})x^2(1-4\epsilon^2)\Theta(-x)\Theta(1-4\epsilon^2)\right\rangle_G \tag{4.3.6}$$

Although tedious, the Gaussian integrals in (4.3.6) can be performed explicitly [35] to yield

$$\left(\frac{dN_{\rm pk}(\nu)}{d\nu}\right)_G = \frac{(\sigma_\eta\theta_{\rm FOV})^2}{2(2\pi)^{3/2}\gamma^2}e^{-\nu^2/2}G(\gamma,\gamma\nu) \tag{4.3.7}$$

$$\begin{aligned} G(\gamma,t) &= (t^2-\gamma^2)\left[1-\frac{1}{2}{\rm erfc}\left(\frac{t}{\sqrt{2(1-\gamma^2)}}\right)\right] \\ &+\frac{t(1-\gamma^2)}{\sqrt{2\pi(1-\gamma^2)}}+\frac{e^{-t^2/(3-2\gamma^2)}}{\sqrt{3-2\gamma^2}}\left[1-\frac{1}{2}{\rm erfc}\left(\frac{t}{\sqrt{2(1-\gamma^2)(3-2\gamma^2)}}\right)\right] \end{aligned} \tag{4.3.8}$$

Figure 4.4 shows a comparison between the peak histogram measured from one of our simulated κ maps and the histogram predicted using the Gaussian approximation (4.3.7), which makes use of the quadratic κ moments $\sigma_0, \sigma_\eta, \sigma_\zeta$. We can clearly see a departure of the measured histogram profile from the Gaussian approximation. The measured peak histogram displays a high κ tail that the Gaussian formula (4.3.7) ignores. This could be a hint that the peak histogram profile contains additional cosmological information than quadratic κ moments, by themselves, miss. This issue will be investigated in Chapter 5.

4.4 Angular power spectrum

In the previous sections we discussed image features which are local, or can be expressed as local estimators in κ. In this section we go beyond locality and focus on the information

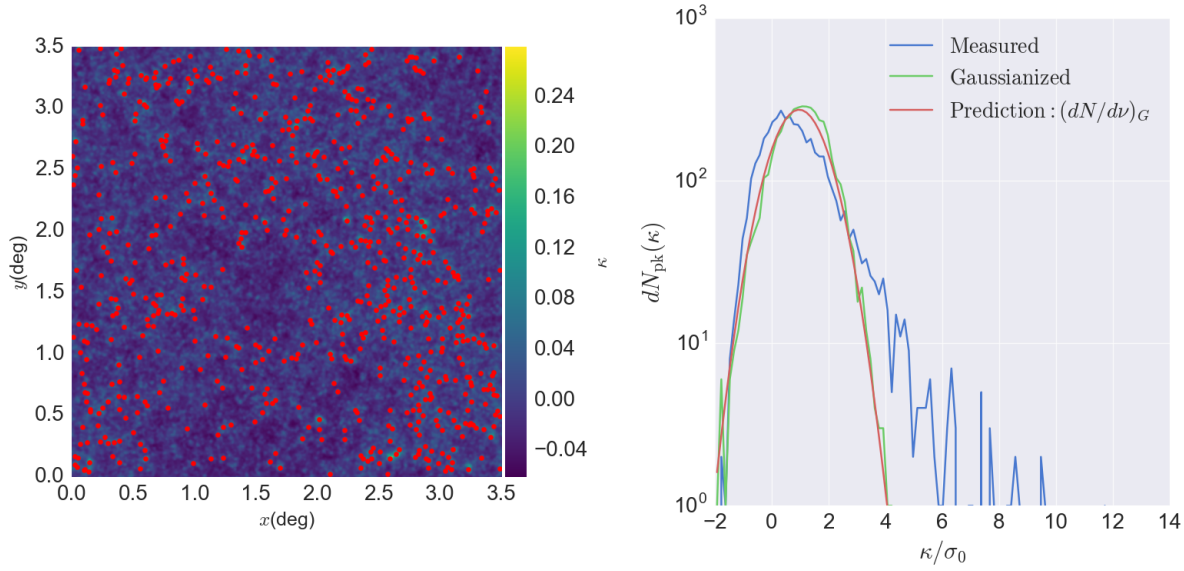

Figure 4.4: A sample κ map ($\theta_{\rm FOV} = 3.5\,{\rm deg}$) with the locations of its peaks (identified by the 8 nearest neighboring pixels) highlighted in red dots. The right panel shows the peak number (blue) as a function of the peak height $\nu\sigma_0$. The panel also shows the peak histogram for a Gaussian κ field with the same power spectrum as the WL simulated one (green) and the Gaussian prediction (red) for $dN_{\rm pk}/d\nu$ obtained with equation (4.3.7).

contained in larger scale correlations of κ. The most straightforward non local feature in κ one can consider is the angular two–point correlation function defined defined by

$$\xi_{\kappa\kappa}(\alpha) = \langle \hat{\kappa}(\boldsymbol{\theta})\hat{\kappa}(\boldsymbol{\theta}+\boldsymbol{\alpha})\rangle \tag{4.4.1}$$

In the definition (4.4.1) the correlation function $\xi_{\kappa\kappa}$ depends on the magnitude $\alpha = |\boldsymbol{\alpha}|$ of the angular lag $\boldsymbol{\alpha}$ only because cosmic WL fields are statistically invariant under translations and rotations. Quadratic non–local correlations, such as the one defined by (4.4.1), are better expressed in terms of the Fourier transform $\tilde{\kappa}(\boldsymbol{\ell})$ as

$$\left\langle \hat{\tilde{\kappa}}(\boldsymbol{\ell})\hat{\tilde{\kappa}}(\boldsymbol{\ell}')\right\rangle = (2\pi)^2\delta^D(\boldsymbol{\ell}+\boldsymbol{\ell}')P_{\kappa\kappa}(\ell) \tag{4.4.2}$$

Translational invariance causes the Dirac delta to appear in (4.4.2) and rotational invariance makes the angular power spectrum $P_{\kappa\kappa}$ depend on $\ell = |\boldsymbol{\ell}|$ only. In the limit of full sky coverage, we can relate $\xi_{\kappa\kappa}$ and $P_{\kappa\kappa}$ using both (4.4.1) and (4.4.2):

$$\xi_{\kappa\kappa}(\alpha) = \int \frac{d\boldsymbol{\ell}}{(2\pi)^2} P_{\kappa\kappa}(\ell) e^{i\boldsymbol{\ell}\cdot\boldsymbol{\alpha}} \tag{4.4.3}$$

The relation (4.4.3) is valid in the flat sky limit, with spherical harmonic corrections kicking in at small ℓ. Under the assumption of statistical isotropy, a practical estimator for $P_{\kappa\kappa}$ is obtained by replacing the expectation value in (4.4.2) with a Fourier space integral over the multipoles with constant magnitude $\ell = |\boldsymbol{\ell}|$. One can show that, if the Fourier transform $\tilde{\kappa}$ is computed from a field of view of linear size $\theta_{\rm FOV}$, the estimator

$$\hat{P}_{\kappa\kappa}(\ell) = \frac{1}{\theta^2_{\rm FOV}} \int \frac{d\boldsymbol{\ell}'}{2\pi\ell'} \left|\hat{\tilde{\kappa}}(\boldsymbol{\ell}')\right|^2 \delta^D\left(|\boldsymbol{\ell}'| - \ell\right) \tag{4.4.4}$$

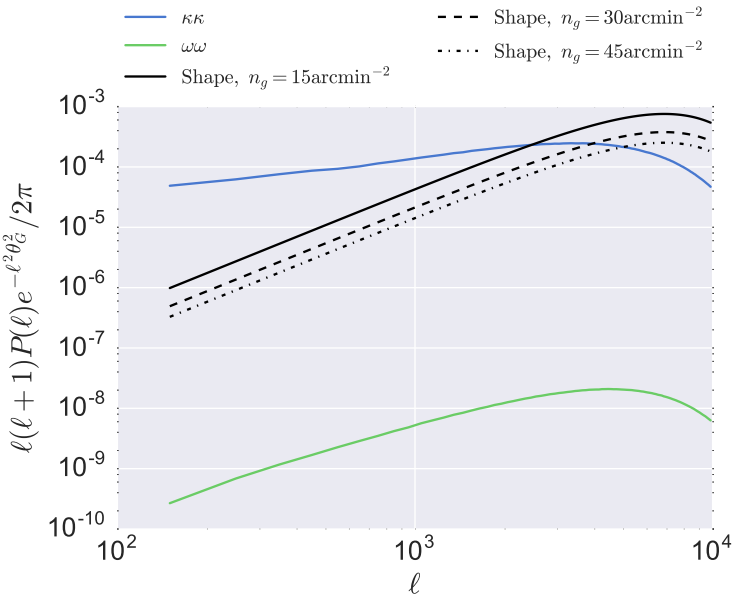

Figure 4.5: κ (blue) and ω (green, see equation (2.2.2)) angular power spectra, measured from the average of 1024 realizations of a fiducial cosmology in a field of view of size $\theta_{\rm FOV} = 3.5\,\deg$. The source galaxies were placed on a plane at $z_s = 2$. For reference we also show the auto–power spectra of Gaussian white shape noise (black) for three different choices of the angular galaxy density $n_g = 15, 30, 45\,\text{galaxies}/\text{arcmin}^2$. We applied a smoothing factor $e^{-\ell^2\theta_G^2}$ to the power spectra, corresponding to a Gaussian window of size $\theta_G = 0.5'$.

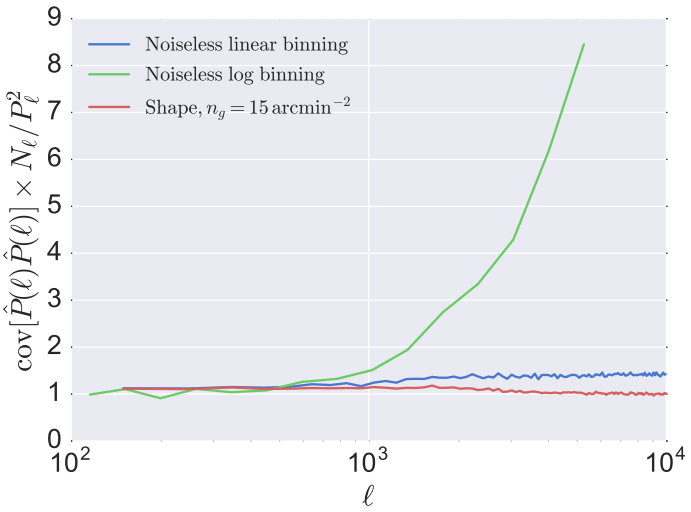

Figure 4.6: Measurement of the power spectrum diagonal covariance matrix in units of the Gaussian prediction in equation (4.4.7). N_ℓ is defined to be $\ell\delta\ell_b\theta^2_{\rm FOV}/4\pi$. We measured the $P_{\kappa\kappa}$ covariance matrix from the same 1024 realizations we used in Figure 4.5, and adopted two different binning choices: 100 uniformly spaced bins between $\ell \in [100, 10000]$ and 15 log–spaced bins between $\ell \in [100, 6000]$. We show both the noiseless cases for linear (blue) and log (green) and the case in which shape noise has been added (red) to the κ images with a galaxy density of $n_g = 15\,\mathrm{galaxies/arcmin}^2$.

converges to the real $P_{\kappa\kappa}$ if $\theta_{\rm FOV}$ is sufficiently large compared to the κ angular correlation scale. In Figure 4.5 we show sample behaviors of the WL κ and ω power spectra measured from our simulations, and we compare them with shape noise power spectra. In the Gaussian limit, we can also quantify the scatter of the estimator (4.4.4) by evaluating the $\tilde{\kappa}$ 4–point functions with Wick's theorem. In the limit of $\ell\theta_{\rm FOV} \gg 1$ we can write

$$\left\langle (\hat{P}_{\kappa\kappa}(\ell) - P_{\kappa\kappa}(\ell))(\hat{P}_{\kappa\kappa}(\ell') - P_{\kappa\kappa}(\ell')) \right\rangle_G = \frac{4\pi P^2_{\kappa\kappa}(\ell)}{\ell\theta^2_{\rm FOV}}\delta^D(\ell - \ell') \tag{4.4.5}$$

Looking at (4.4.5), we immediately conclude that, in the Gaussian case, the κ power spectrum covariance matrix is diagonal and is inversely proportional to the area of the field of view and to the number of multipoles $\sim \ell$ that fall inside $\theta_{\rm FOV}$. In a more realistic case, in which we measure the value of $P_{\kappa\kappa}$ smeared over a multipole bin of size $\delta\ell_{\rm bin}$ using

$$\hat{P}^{\rm bin}_{\kappa\kappa}(\ell_b) = \frac{1}{\delta\ell_{\rm bin}}\int_{\ell_b-\delta\ell_{\rm bin}/2}^{\ell_b+\delta\ell_{\rm bin}/2} d\ell \hat{P}_{\kappa\kappa}(\ell), \tag{4.4.6}$$

the estimator scatter assumes the familiar form

$$\left\langle \delta\hat{P}^{\rm bin}_{\kappa\kappa}(\ell_b)\delta\hat{P}^{\rm bin}_{\kappa\kappa}(\ell_{b'}) \right\rangle_G = \frac{4\pi[P^{\rm bin}_{\kappa\kappa}(\ell_b)]^2}{\ell_b\delta\ell_{\rm bin}\theta^2_{\rm FOV}}\delta_{bb'} \tag{4.4.7}$$

Figure 4.6 shows that (4.4.6) is a good approximation to the real power spectrum covariance matrix if one uses linear ℓ binning, but large non–Gaussian effects dominate at large ℓ when one uses log–spaced multipole bands [36, 25]. Figure 4.6 also shows that the Gaussian approximation is exact when shape noise is added to the κ images. This is reasonable since the shape noise we introduce is Gaussian distributed and its large covariance tends to

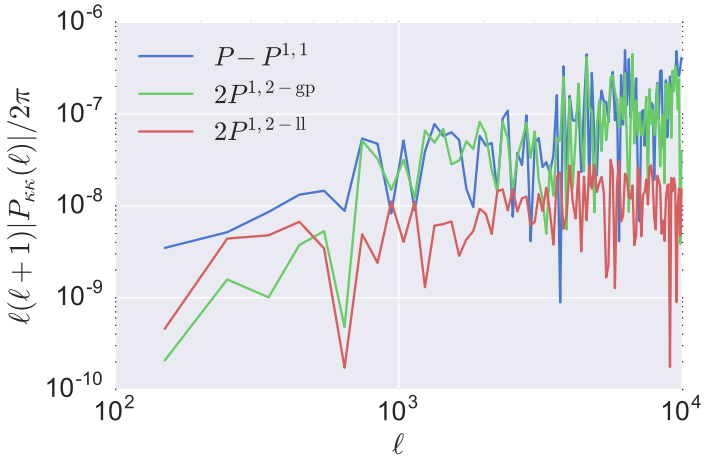

Figure 4.7: Difference between the full κ power spectrum, obtained from ray–tracing, and its Born approximated version. We show the measured power residuals (blue), and the Born–geodesic (green), Born–lens–lens (red) cross spectra averaged over 8192 field of view realizations ($z_s = 2, \theta_{\rm FOV} = 3.5\,\deg$) of a fiducial ΛCDM model.

dominate the WL signal on small scales. In the next sub–section we investigate the validity of the Born approximation (2.2.13) in predicting $P_{\kappa\kappa}$.

4.4.1 Born approximation

Since quadratic features, both in real and Fourier space, are the primary investigation tools for cosmological parameter inference in WL, we investigated how accurately the Born approximation (2.2.13) predicts the κ power spectrum. If we define

$$\left\langle \hat{\tilde{\kappa}}^{(i)}(\boldsymbol{\ell})\hat{\tilde{\kappa}}^{(j)}(\boldsymbol{\ell}')\right\rangle = (2\pi)^2\delta^D(\boldsymbol{\ell}+\boldsymbol{\ell}')P^{i,j}_{\kappa\kappa}(\ell) \tag{4.4.8}$$

where $\kappa^{(i)}$ is an $O(\Phi^i)$ contribution to κ, we can express the κ power spectrum in a power series in Φ. The first few terms of this series are

$$P_{\kappa\kappa} = P^{1,1}_{\kappa\kappa} + 2\Re(P^{1,2-\mathrm{ll}}_{\kappa\kappa} + P^{1,2-\mathrm{gp}}_{\kappa\kappa}) + O(\Phi^4) \tag{4.4.9}$$

The first non–trivial corrections to the Born approximated power spectrum are of $O(\Phi^3)$ and, as Figure 4.7 shows, they can account for the residuals $P_{\kappa\kappa} - P^{1,1}_{\kappa\kappa}$. The Born–geodesic cross terms, which trace local gradients in the cosmic density field, dominate over the Born–lens–lens terms, which are proportional to the non–local couplings of the tidal field. Depending in how big the statistical error on the measured $\hat{P}_{\kappa\kappa}$ is, the Born approximation may induce biases when used in the inference of cosmological parameters. This could in principle be an issue for large scale surveys since, as seen in (4.4.7), the variance in the power spectrum measurement is inversely proportional to the sky area covered by the survey. We will investigate WL constraints on ΛCDM parameters in Chapters 5,6 and 7.

4.5 Convergence moments

Because the WL κ field is non–Gaussian, higher order Fourier statistics contain statistical information that the power spectrum ignores. We can define a n–point correlation function of κ, both in real and Fourier space, as

$$\xi^{(n)}_{\kappa} = \langle \kappa(\boldsymbol{\theta}_1)...\kappa(\boldsymbol{\theta}_n)\rangle \tag{4.5.1}$$

$$\langle \tilde{\kappa}(\boldsymbol{\ell}_1)...\tilde{\kappa}(\boldsymbol{\ell}_n)\rangle_c = (2\pi)^{2n}\delta^D(\boldsymbol{\ell}_1 + ... + \boldsymbol{\ell}_n)P^{(n)}_{\kappa}(\boldsymbol{\ell}_1, ..., \boldsymbol{\ell}_n) \tag{4.5.2}$$

As previously noted, the Dirac delta function appears in (4.5.2) because of invariance under translations. The complete Fourier profile of the multi–spectra $P^{(n)}_{\kappa}$ can be computationally expensive to measure from high resolution κ images (the computational cost scales roughly

as $O(N_R^n)$, where N_R is the number of pixels in the image) but, if we are interested in selected multipole features only, we might be able to measure a finite, small number of kernel projections of $P_\kappa^{(n)}$ and still get some insight on the cosmological information carried by the κ non–Gaussianity. In order to perform the projection, we smooth the κ image with a Gaussian window of size θ_G and choose an arbitrary function of the multipoles $\tilde{\mu}$. We define

$$\mu_i^{(n)}(\theta_G) = \int d\boldsymbol{\ell}_1 ... d\boldsymbol{\ell}_n \delta^D(\boldsymbol{\ell}_1 + ... + \boldsymbol{\ell}_n) \left[\tilde{\mu}_i^{(n)} P_\kappa^{(n)}\right](\boldsymbol{\ell}_1, ..., \boldsymbol{\ell}_n) e^{-\theta_G^2(\ell_1^2+...+\ell_n^2)/2} \quad (4.5.3)$$

If $\tilde{\mu}_i^{(n)}$ is polynomial in the multipoles, $\mu_i^{(n)}$ is a connected local moment of the θ_G–smoothed convergence. Different choices of θ_G, $\mu_i^{(n)}$ probe different features in the κ multi–spectra at low computational cost. The only operations that need to be performed are the smoothing convolution and the measurement of local expectation values, which are cheap operations with complexity $O(N_R \log N_R), O(N_R)$ respectively. Motivated by the discussion in § 4.2.1 about the relation between morphological features and κ moments, in this work we focus our attention on the multi–spectra projections defined by the following nine polynomials

$$\tilde{\mu}_0^{(2)} = 1 \quad ; \quad \tilde{\mu}_1^{(2)} = \boldsymbol{\ell}_1 \cdot \boldsymbol{\ell}_2 \quad (4.5.4)$$

$$\tilde{\mu}_0^{(3)} = 1 \quad ; \quad \tilde{\mu}_1^{(3)} = \ell_3^2 \quad ; \quad \tilde{\mu}_2^{(3)} = \ell_3^2(\boldsymbol{\ell}_1 \cdot \boldsymbol{\ell}_2) \quad (4.5.5)$$

$$\tilde{\mu}_0^{(4)} = 1 \quad ; \quad \tilde{\mu}_1^{(4)} = \ell_4^2 \quad ; \quad \tilde{\mu}_2^{(4)} = \ell_4^2(\boldsymbol{\ell}_2 \cdot \boldsymbol{\ell}_3) \quad ; \quad \tilde{\mu}_3^{(4)} = (\boldsymbol{\ell}_1 \cdot \boldsymbol{\ell}_2)(\boldsymbol{\ell}_3 \cdot \boldsymbol{\ell}_4) \quad (4.5.6)$$

Note that, with these choices, the quadratic projections defined by (4.5.4) correspond to σ_0^2 and $\sigma_0^2\sigma_\eta^2$ respectively. The cubic and quartic projections defined by (4.5.5), (4.5.6), on the other hand, are equivalent to the local κ moments defined in (4.2.19), (4.2.20) modulo normalization factors. The polynomial nature of the kernels $\tilde{\mu}_i^{(n)}$, make it so $\mu_i^{(n)}$ capture local features in the convergence maps. By varying and combining different smoothing scales θ_G, one can hope to probe different angular scales in the multi–spectra, hence gaining sensitivity to large scale angular correlations.

4.5.1 Born approximation

In the same flavor as § 4.4.1, in this sub–section we study the accuracy of the Born approximation (2.2.13) in predicting the first few moments of κ, defined by the projections in (4.5.4), (4.5.5) and (4.5.6). Since these features are polynomial in Φ, it is easy to isolate the main contribution to $\mu_i^{(n)}$ as $O(\Phi^n)$. The first non trivial correction is of order $O(\Phi^{n+1})$. For the κ skewness and kurtosis we have

$$\kappa^3 = \left(\kappa^{(1)}\right)^3 + 3\left[\left(\kappa^{(1)}\right)^2 \kappa^{(2-\mathrm{ll})} + \left(\kappa^{(1)}\right)^2 \kappa^{(2-\mathrm{gp})}\right] + O(\Phi^5) \tag{4.5.7}$$

$$\kappa^4 = \left(\kappa^{(1)}\right)^4 + 4\left[\left(\kappa^{(1)}\right)^3 \kappa^{(2-\mathrm{ll})} + \left(\kappa^{(1)}\right)^3 \kappa^{(2-\mathrm{gp})}\right] + O(\Phi^6) \tag{4.5.8}$$

We show the residuals between the results obtained with ray–tracing and the Born approximation in Figure 4.8, which compares the difference $\delta\kappa^n = \kappa^n - \left(\kappa^{(1)}\right)^n$ to the largest non trivial post–Born corrections contained in (4.5.7), (4.5.8). The Figure shows that the first post–Born corrections can fully account for the residuals and, contrary to the power spectrum case, for higher κ moments the Born–geodesic and Born–lens–lens terms are comparable in magnitude. Figure 4.8 also shows that, for the sake of predicting κ mo-

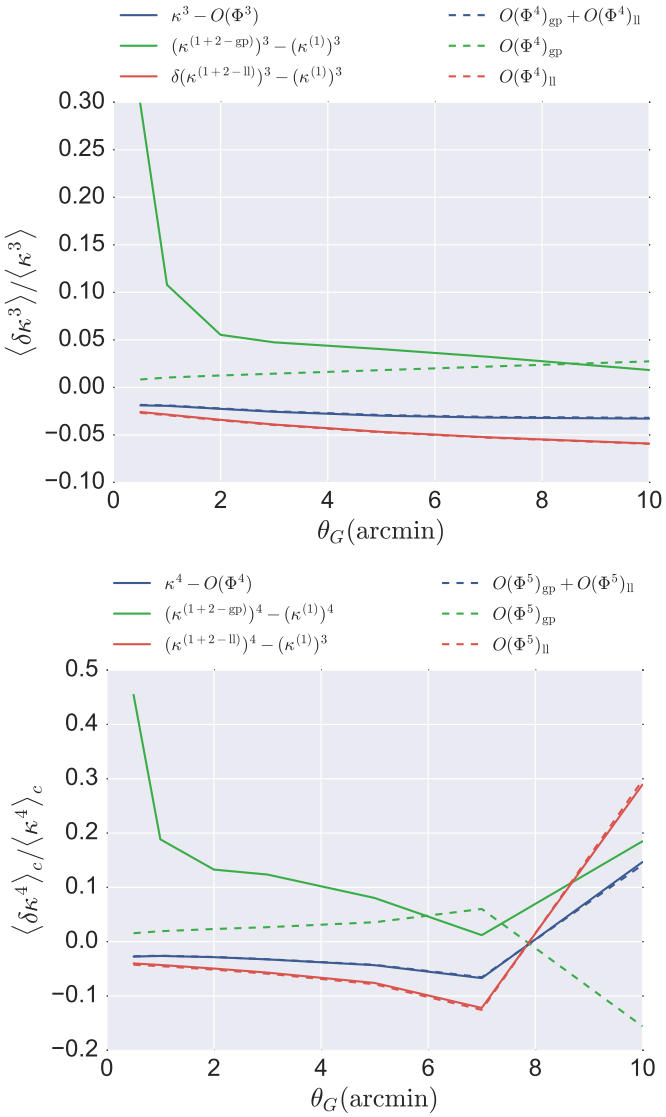

Figure 4.8: Comparison between the κ skewness and kurtosis obtained with full ray–tracing and with the Born approximation. With the solid lines we show the residuals between the Born result and the ray–tracing (blue), the geodesic truncated (green) and the lens–lens truncated (red) kappa. The dashed line show the first post–Born corrections in equations (4.5.7), (4.5.8) for the geodesic (green), lens–lens (red) cross terms, and the sum of the two (blue). We plot the results as a function of the smoothing scales θ_G, averaging over 8192 realizations of the field of view in a fiducial ΛCDM model.

ments, it is not advisable to truncate the κ power series in Φ at $O(\Phi^2)$. The reason is that, by doing so, large numerical contributions to the moments, coming from $O\left(\left(\kappa^{(2-\mathrm{gp})}\right)^2\right)$ terms and higher are not canceled by terms of order $O\left(\kappa^{(3)}\kappa^{(1)}\right)$, which have the same magnitude [37]. Ray–tracing is hence required to accurately improve the Born approximation. The issue whether the Born–approximated κ moments leads to biased inferences on ΛCDM parameters will be investigated in Chapter 7.

4.6 Summary

In this Chapter we gave an overview of image features (which is by no means exhaustive) that can be measured from κ pixelated images. We considered features which are local in κ (such as moments) or that can be expressed as expectation values of local κ estimators. We have also considered Fourier space features, such as the κ angular power spectrum, that are non–local and require knowledge of κ over the entire field of view to be measured. This can cause issues in WL analyses, as we will see in Chapter 6: masked regions in the field of view lead to biased measurements of the power spectrum, which can produce biases in parameter inferences if accounted for in feature forward models. Local estimators, on the other hand, are well behaved even in the presence of masks, provided that one excludes regions nearby the mask boundaries when calculating the expectation values. Following the literature, we examined classes of features which are not polynomial in κ, such as MFs and peak count histograms, showing in both cases that a relationship with κ local moments can be established via perturbation theory. The fact that the first few perturbative orders do not reproduce the features well lead us to claim that the angular power spectrum, κ moments (which probe selected polygon shapes in κ multi–spectra), morphological descriptors and

peak counts contain complementary information about cosmology. In the next Chapter we will focus on how these κ features can be used to infer the values of ΛCDM parameters, as well as their confidence intervals.

Chapter 5

Cosmological parameter inference

In this Chapter we introduce the Standard Model parameter inference techniques used in this work. The parameter inference procedure from WL observations starts with the construction of κ images from galaxy shear catalogs. Image features $\mathbf{d}$ are then extracted from the reconstructed images. When a forward model $\mathbf{d}(\mathbf{p})$ that relates features to ΛCDM parameters $\mathbf{p}$ is specified, an estimate of the parameters $\hat{\mathbf{p}}$ can be derived from the measured feature $\hat{\mathbf{d}}$ in a Bayesian fashion. In this Chapter we review the Bayesian probabilistic framework and we study parameter constraints from WL using the image features discussed in Chapter 4. We also discuss some of the numerical and physical effects that lead to the degradation of confidence intervals, suggesting possible mitigation techniques.

5.1 Bayesian formalism

In this section we describe the Bayesian probabilistic framework on which we base the ΛCDM parameter inference. We indicate a N_d–dimensional image feature as $\mathbf{d}$ and a N_π–dimensional tuple of ΛCDM parameters (see Table 1.1) as $\mathbf{p}$. We also denote feature

estimates from a simulated κ field of view as $\hat{\mathbf{d}}$, feature measurements from an actual observation as $\hat{\mathbf{d}}_{\rm obs}$ and the resulting parameter estimates as $\hat{\mathbf{p}}$. We assume the existence of a forward model $\mathbf{d}(\mathbf{p})$, which can be calculated using our WL simulation pipeline described in § 3.4 or, in special cases such as for the κ power spectrum, using analytical codes like NICAEA [38, 39]. According to Bayes theorem, the likelihood $\mathcal{L}(\hat{\mathbf{p}}|\hat{\mathbf{d}}_{\rm obs})$ of a parameter estimate $\hat{\mathbf{p}}$ given an observation $\hat{\mathbf{d}}_{\rm obs}$ is given by

$$\mathcal{L}(\hat{\mathbf{p}}|\hat{\mathbf{d}}_{\rm obs}, \mathbf{d}(\mathbf{p})) = \frac{\mathcal{L}(\hat{\mathbf{d}}_{\rm obs}|\hat{\mathbf{p}}, \mathbf{d}(\mathbf{p}))\Pi(\hat{\mathbf{p}})}{\mathcal{L}(\hat{\mathbf{d}}_{\rm obs})} \tag{5.1.1}$$

In equation (5.1.1), Π encodes prior information on the parameters coming from independent probes independent from WL (such as CMB experiments) and $\mathcal{L}(\hat{\mathbf{d}}_{\rm obs})$ is the overall likelihood of the observation, which plays the simple role of a $\mathbf{p}$–independent normalization factor in the parameter likelihood (5.1.1). In the prosecution of this work this normalization factor will be ignored. We assume a Gaussian feature likelihood

$$\mathcal{L}(\hat{\mathbf{d}}_{\rm obs}|\hat{\mathbf{p}}, \mathbf{d}(\mathbf{p})) = \frac{1}{(2\pi)^{N_d/2}|\mathbf{C}|^{1/2}} \exp\left(-\frac{1}{2}(\hat{\mathbf{d}}_{\rm obs} - \mathbf{d}(\mathbf{p}))^T \mathbf{C}^{-1} (\hat{\mathbf{d}}_{\rm obs} - \mathbf{d}(\mathbf{p}))\right), \tag{5.1.2}$$

where $\mathbf{C}$ is the $\mathbf{p}$–independent feature–feature covariance matrix. The Gaussian assumption for the data likelihood is justified by the Central Limit Theorem because measured image features are averaged over a large number of $\theta_{\rm FOV} = 3.5\,{\rm deg}$ fields of view (13 for CFHTLenS and over 1000 for LSST). We do not discuss covariance matrix dependence on $\mathbf{p}$ in this work, reserving the topic for future investigation.

Parameter confidence intervals can be obtained looking at surfaces in $\mathbf{p}$ space with constant $\mathcal{L}(\hat{\mathbf{p}})$. We define an $N\sigma$ confidence interval to be the region in $\mathbf{p}$ space in which

$\mathcal{L} > \mathcal{L}_N$. The likelihood confidence levels are defined as

$$\int_{\mathcal{L}>\mathcal{L}_N} \mathcal{L}(\hat{\mathbf{p}}|\hat{\mathbf{d}}_{\rm obs}, \mathbf{d}(\mathbf{p}))d\hat{\mathbf{p}} = \frac{1}{\sqrt{2\pi}} \int_{-N}^{N} e^{-x^2/2} dx \tag{5.1.3}$$

Note that this definition of $N\sigma$ confidence intervals (see Figure 5.1 for a visual example) corresponds to the commonly accepted one when $\mathcal{L}(\hat{\mathbf{p}})$ is a multivariate Gaussian in $\hat{\mathbf{p}}$. In this case, calling $\hat{\mathbf{p}}_0$ the location of the likelihood peak, the matrix $\mathbf{\Sigma}$ defined by

$$\left(\Sigma^{-1}\right)_{\alpha\beta} = -\left(\frac{\partial^2 \log \mathcal{L}(\hat{\mathbf{p}})}{\partial \hat{p}_\alpha \partial \hat{p}_\beta}\right)_{\hat{\mathbf{p}}=\hat{\mathbf{p}}_0}, \tag{5.1.4}$$

is the covariance of the parameter estimate. If the parameter likelihood is not a multivariate Gaussian, we can still use the peak location $\hat{\mathbf{p}}_0$ and the matrix (5.1.4) as estimates of the parameters and of their covariance matrix, although a complete characterization of the parameter space through the confidence intervals defined in (5.1.3) is preferred. Confidence intervals can be calculated by drawing samples from $\mathcal{L}(\hat{\mathbf{p}})$ using Markov Chain Monte Carlo (MCMC) techniques, which are implemented by many user–friendly software packages, such as `emcee` [40]. An example of 1,2 and 3σ confidence contours on the parameter doublet (Ω_m, σ_8) is shown in Figure 5.1.

5.1.1 Fisher matrix approximation

Parameter inference becomes simpler if the forward model $\mathbf{d}(\mathbf{p})$ is linear. Linearity can be safely assumed if confidence intervals are localized around the peak of the likelihood, which is the case for large scale surveys. Under the linearity assumption, we can write

$$\mathbf{d}(\mathbf{p}) = \mathbf{d}_0 + \mathbf{M}(\mathbf{p} - \mathbf{p}_0) + O(|\mathbf{p} - \mathbf{p}_0|^2). \tag{5.1.5}$$

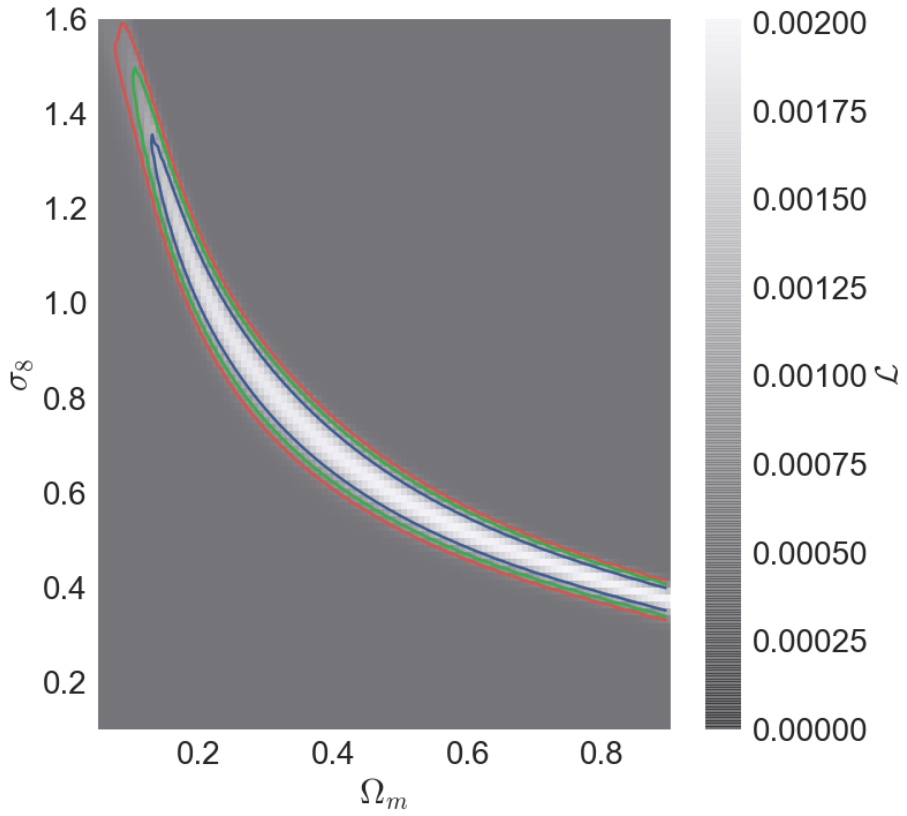

Figure 5.1: Sample 1 (blue), 2 (green) and 3σ (red) example confidence contours on (Ω_m, σ_8). The gray scale refers to the value of the parameter likelihood $\mathcal{L}(\hat{\mathbf{p}})$.

Assuming a flat prior $\Pi(\hat{\mathbf{p}})$ and substituting (5.1.5) into (5.1.2) we get, for the $\mathbf{p}$–dependent part of the likelihood

$$-2\log\mathcal{L}(\mathbf{p}) = \left[\hat{\mathbf{d}}_{\rm obs} - \mathbf{d}_0 - \mathbf{M}(\mathbf{p}-\mathbf{p}_0)\right]^T \mathbf{\Psi} \left[\hat{\mathbf{d}}_{\rm obs} - \mathbf{d}_0 - \mathbf{M}(\mathbf{p}-\mathbf{p}_0)\right] \tag{5.1.6}$$

We used the notation $\mathbf{\Psi} = \mathbf{C}^{-1}$. We can estimate the peak location of the likelihood $\hat{\mathbf{p}}_0$ and its covariance $\mathbf{\Sigma}$ from (5.1.6) using (5.1.4):

$$\hat{\mathbf{p}}_0 = \mathbf{p}_0 + \left(\mathbf{M}^T\mathbf{\Psi}\mathbf{M}\right)^{-1}\mathbf{M}^T\mathbf{\Psi}\left(\hat{\mathbf{d}}_{\rm obs} - \mathbf{d}_0\right) \tag{5.1.7}$$

$$\mathbf{\Sigma} = \mathbf{F}^{-1} \equiv \left(\mathbf{M}^T\mathbf{\Psi}\mathbf{M}\right)^{-1} \tag{5.1.8}$$

Equations (5.1.7), (5.1.8) take the name of *Fisher matrix* approximation and $\mathbf{F} \equiv \mathbf{M}^T\mathbf{\Psi}\mathbf{M}$ is usually referred to as *Fisher information matrix*. When prior information on the parameters is available, the estimates for the likelihood peak and covariance matrix have to be modified. If the prior is a multivariate Gaussian with distribution

$$\Pi(\mathbf{p}) = \sqrt{\frac{|\mathbf{F}_\Pi|}{(2\pi)^{N_\pi}}}\exp\left(-\frac{1}{2}(\mathbf{p}-\mathbf{p}_\Pi)^T\mathbf{F}_\Pi(\mathbf{p}-\mathbf{p}_\Pi)\right), \tag{5.1.9}$$

we can write

$$\hat{\mathbf{p}}_0 = (\mathbf{F}+\mathbf{F}_\Pi)^{-1}\left[\mathbf{F}_\Pi\mathbf{p}_\Pi + \mathbf{F}\mathbf{p}_0 + \mathbf{M}^T\mathbf{\Psi}(\hat{\mathbf{d}}-\mathbf{d}_0)\right] \tag{5.1.10}$$

$$\mathbf{\Sigma} = (\mathbf{F}+\mathbf{F}_\Pi)^{-1} \tag{5.1.11}$$

Equation (5.1.11) states that, if the parameter prior is independent from the WL observation, inverse parameter covariances have to be added in quadrature. If the parameter likelihood and prior peak at the same location $\mathbf{p}_0 = \mathbf{p}_\Pi$, equation (5.1.10) reduces to (5.1.7) with a modified Fisher information matrix $\mathbf{F} + \mathbf{F}_\Pi$.

5.2 Error degradation induced by noise in the covariance matrix

In the previous derivation of parameter estimates (5.1.7) and covariances (5.1.8), we have assumed perfect knowledge of the feature–feature covariance matrix $\mathbf{C}$ and of its inverse $\mathbf{\Psi}$. Although smooth models exist for the covariance matrix of the κ power spectrum (see (4.4.5) for example), the same is not true for the higher order features described in Chapter 4. When such smooth models are not readily available one can obtain an estimate $\hat{\mathbf{C}}$ of $\mathbf{C}$ from simulations. The estimate can then be used to calculate an approximate feature likelihood (5.1.2). If one choses this way to proceed, the noise in the estimator $\hat{\mathbf{C}}, \hat{\mathbf{\Psi}}$ carries over to the parameter estimate $\hat{\mathbf{p}}_0$ and covariance $\mathbf{\Sigma}$, which is then only available as a noisy estimate $\hat{\mathbf{\Sigma}}$. If simulations and observations are independent from each other, the parameter estimate $\hat{\mathbf{p}}_0$ is unbiased (within the limits of the linear approximation (5.1.5)). The parameter covariance estimator defined by

$$\hat{\mathbf{\Sigma}}_1 = \hat{\mathbf{F}}^{-1}, \tag{5.2.1}$$

on the other hand, is a biased estimate of $\mathbf{\Sigma}$, as we will see later in the Chapter. The unbiased version of (5.2.1) is the correct estimation of the error–bar to assign to $\hat{\mathbf{p}}_0$ only if

the scatter of the estimator (5.1.7) is equal to Σ. We will see, unfortunately, that this is not true. With the simplifying assumption that $\langle \hat{\mathbf{d}}_{\rm obs} - \mathbf{d}_0 \rangle = 0$, the scatter of (5.1.7) is given by

$$\left\langle \delta\hat{\mathbf{p}}_0 \delta\hat{\mathbf{p}}_0^T \right\rangle = \left\langle \hat{\mathbf{F}}^{-1}\mathbf{M}^T\hat{\mathbf{\Psi}}(\hat{\mathbf{d}}_{\rm obs} - \mathbf{d}_0)(\hat{\mathbf{d}}_{\rm obs} - \mathbf{d}_0)^T\hat{\mathbf{\Psi}}\mathbf{M}\hat{\mathbf{F}}^{-1} \right\rangle . \tag{5.2.2}$$

In equation (5.2.2), the expectation value has to be taken with respect of both the observations and the simulations, which are both affected by noise but are uncorrelated. To have an idea of the magnitude of (5.2.2), we can take the expectation value over the observation and focus ourselves on the the noise introduced exclusively by the simulations. We will use the fact

$$\left\langle (\hat{\mathbf{d}}_{\rm obs} - \mathbf{d}_0)(\hat{\mathbf{d}}_{\rm obs} - \mathbf{d}_0)^T \right\rangle = \mathbf{C} \tag{5.2.3}$$

to produce a noisy estimator of the $\hat{\mathbf{p}}_0$ scatter, which we call $\hat{\mathbf{\Sigma}}_2$. The latter quantity is defined as

$$\hat{\mathbf{\Sigma}}_2 = \hat{\mathbf{F}}^{-1}\mathbf{M}^T\hat{\mathbf{\Psi}}\mathbf{C}\hat{\mathbf{\Psi}}\mathbf{M}\hat{\mathbf{F}}^{-1} \tag{5.2.4}$$

In the next sub–section we are going to show how the expectation values of (5.2.1) and (5.2.4) over the simulations can be calculated explicitly under a Gaussianity assumption.

5.2.1 Covariance matrix estimation

In order to produce estimates of the feature–feature covariance matrix $\mathbf{C}$, we use our WL simulation pipeline (described in Chapter 3.4), whose products are pseudo–independent

realizations of κ in a WL field of view. We measure the feature $\hat{\mathbf{d}}_r$ from each simulated image using the techniques described in Chapter 4 and we produce an estimator for the covariance matrix $\hat{\mathbf{C}}$ based on simulated ensembles of N_r image realizations:

$$\hat{\mathbf{d}}_{\rm mean} = \frac{1}{N_r}\sum_{r=1}^{N_r}\hat{\mathbf{d}}_r \tag{5.2.5}$$

$$\hat{\mathbf{C}} = \frac{1}{n}\sum_{r=1}^{N_r}\left(\hat{\mathbf{d}}_r - \hat{\mathbf{d}}_{\rm mean}\right)^T\left(\hat{\mathbf{d}}_r - \hat{\mathbf{d}}_{\rm mean}\right) \tag{5.2.6}$$

We indicated the effective number of degrees of freedom in the ensemble as $n = N_r - 1$. This effective number is smaller than N_r because the mean feature $\hat{\mathbf{d}}_{\rm mean}$ is not known and has to be estimated from the ensembles themselves. If the feature estimate $\hat{\mathbf{d}}_r$ is drawn from a multivariate Gaussian distribution with covariance matrix $\mathbf{C}$, the covariance estimate $\hat{\mathbf{C}}$ is distributed according to the Wishart probability density [41, 42, 43]. A functional form for the Wishart density function, $\mathcal{L}(\hat{\mathbf{C}}|\mathbf{C}, n)$, can be obtained from its characteristic function

$$\phi(\mathbf{J}) = \left\langle e^{i{\rm Tr}(\mathbf{J}\hat{\mathbf{C}})}\right\rangle \tag{5.2.7}$$

We can derive an expression of $\mathcal{L}(\hat{\mathbf{C}}|\mathbf{C}, n)$ from $\phi(\mathbf{J})$ performing an inverse Fourier transform in matrix space (much like the inversion described in (4.1.6)). The characteristic function ϕ can be evaluated from the moments of the Wishart distribution, which are easily expressed in terms of $\mathbf{C}$ and n via a straightforward though tedious procedure based on Wick's theorem. After the smoke clears we get (see [41] for the details)

$$\phi(\mathbf{J}) = \left|\mathbb{1}_{N_d\times N_d} - \frac{2i\mathbf{J}\mathbf{C}}{n}\right|^{-n/2} \tag{5.2.8}$$

The inverse Fourier transform leads to the functional form of the Wishart density function $\mathcal{L}(\hat{\mathbf{C}}|\mathbf{C}, n) = \mathcal{W}(\mathbf{C}, \hat{\mathbf{C}}, n)$, with

$$\mathcal{W}(\mathbf{C}, \hat{\mathbf{C}}, n) = \left(\frac{n^{nN_d/2} |\mathbf{C}|^{-n/2} |\hat{\mathbf{C}}|^{(n-N_d-1)/2}}{2^{nN_d/2} \Gamma_{N_d}(n/2)} \right) \exp\left(-\frac{n}{2} \mathrm{Tr}(\hat{\mathbf{C}}\mathbf{C}^{-1}) \right) \tag{5.2.9}$$

The generalized gamma function Γ_N is defined via an integral over the positive semidefinite $N \times N$ symmetric matrices as

$$\Gamma_N(x) = \int_{\mathbf{X}>0} d\mathbf{X} |\mathbf{X}|^{x-(N+1)/2} e^{-\mathrm{Tr}\mathbf{X}} \tag{5.2.10}$$

We can use the functional form of the Wishart density (5.2.9) to derive a closed formula for the distribution of the estimate of the inverse $\hat{\mathbf{\Psi}} = \hat{\mathbf{C}}^{-1}$. This can be done by means of a change of variables in matrix space. Following [41], we obtain the result $\mathcal{L}(\hat{\mathbf{\Psi}}|\mathbf{\Psi}, n) = \mathcal{W}^{-1}(\hat{\mathbf{\Psi}}, \mathbf{\Psi}, n)$, with

$$\mathcal{W}^{-1}(\hat{\mathbf{\Psi}}, \mathbf{\Psi}, n) = \left(\frac{n^{nN_d/2} |\mathbf{\Psi}|^{n/2} |\hat{\mathbf{\Psi}}|^{-(n+N_d+1)/2}}{2^{nN_d/2} \Gamma_{N_d}(n/2)} \right) \exp\left(-\frac{n}{2} \mathrm{Tr}(\mathbf{\Psi}\hat{\mathbf{\Psi}}^{-1}) \right) \tag{5.2.11}$$

Using the expression (5.2.11), it can be shown (see [43]) that the estimate of the inverse covariance $\hat{\mathbf{\Psi}}$ is biased according to

$$\left\langle \hat{\mathbf{\Psi}} \right\rangle = \frac{n\mathbf{\Psi}}{n - N_d - 1} \tag{5.2.12}$$

Because the moments of the probability distribution of any square sub–matrix of $\hat{\mathbf{\Psi}}$ can be expressed in terms of the relevant elements of $\mathbf{\Psi}$, n and the combination $\gamma = (n - N_d - 1)/2$

(see again [43]), it can be shown that the rescaled Fisher information estimate $\hat{\mathbf{F}}'$, defined by

$$\hat{\mathbf{F}}' = \frac{(n + N_\pi - N_d)\hat{\mathbf{F}}}{n}, \tag{5.2.13}$$

is distributed as $\mathcal{L}(\hat{\mathbf{F}}'|\mathbf{F}', n, N_\pi, N_d) = \mathcal{W}^{-1}(\hat{\mathbf{F}}', \mathbf{F}', n + N_\pi - N_d)$. This fact leads immediately to the conclusion that parameter error bar estimates based on (5.2.1) are biased according to

$$\left\langle \hat{\mathbf{\Sigma}}_1 \right\rangle = \left(1 + \frac{N_\pi - N_d}{n}\right) \mathbf{\Sigma} \tag{5.2.14}$$

This bias can easily be easily mitigated by applying a suitable correction factor (suggested in equation (5.2.14)) to the parameter covariance estimator (5.2.1). This procedure can be used to estimate parameter error bars in an unbiased fashion by relying only on the simulations, can hence be used to obtain approximate forecasts for parameter contours. When analyzing a real observation, however, we are left with a parameter estimate $\hat{\mathbf{p}}_0$ which obtained from the peak of the likelihood. As we are going to see, $\hat{\mathbf{p}}_0$ is drawn from a distribution whose width is larger than $\mathbf{\Sigma}$. This increased scatter originates from the fact that the feature–feature covariance estimate is noisy: even if the $\hat{\mathbf{C}}$ estimator is unbiased, the estimate of the peak scatter $\hat{\mathbf{\Sigma}}_2$, defined in (5.2.4), is not. Unlike the case for $\hat{\mathbf{\Sigma}}_1$, the expectation value of $\hat{\mathbf{\Sigma}}_2$ cannot be calculated exactly and needs to be approximated. We tackle this issue in the next sub–section.

5.2.2 Perturbative calculation of the estimate scatter

It is not possible to calculate the expectation value of (5.2.4) analytically because the expression contains both $\hat{\mathbf{\Psi}}$ and $\hat{\mathbf{F}}^{-1}$. In order to evaluate the behavior of the scatter $\hat{\mathbf{\Sigma}}_2$ with N_d, N_r, we adopt a perturbative approach in the quantity $\delta\hat{\mathbf{\Psi}}$, defined by

$$\hat{\mathbf{\Psi}} = \mathbf{\Psi} + \delta\hat{\mathbf{\Psi}} \tag{5.2.15}$$

With this definition, the expression (5.2.4) can be expanded in a power series in $\delta\hat{\mathbf{\Psi}}$. If the moments of the inverse Wishart distribution are known, we can use them to calculate $\langle\hat{\mathbf{\Sigma}}_2\rangle$ at arbitrary orders in $\delta\hat{\mathbf{\Psi}}$. Using the notation

$$\delta\hat{\mathbf{F}} = \mathbf{M}^T\delta\hat{\mathbf{\Psi}}\mathbf{M}, \tag{5.2.16}$$

we can write

$$\hat{\mathbf{\Sigma}}_2 = (\mathbf{F} + \delta\hat{\mathbf{F}})^{-1}\mathbf{M}^T(\mathbf{\Psi} + \delta\hat{\mathbf{\Psi}})\mathbf{C}(\mathbf{\Psi} + \delta\hat{\mathbf{\Psi}})\mathbf{M}(\mathbf{F} + \delta\hat{\mathbf{F}})^{-1} \tag{5.2.17}$$

The series expansion for $(\mathbf{F} + \delta\hat{\mathbf{F}})^{-1}$, which is given by

$$(\mathbf{F} + \delta\hat{\mathbf{F}})^{-1} = \sum_{k=0}^{\infty}(-1)^k(\mathbf{F}^{-1}\delta\hat{\mathbf{F}})^k\mathbf{F}^{-1}, \tag{5.2.18}$$

provides a straightforward, although algebraically tedious, way to express (5.2.17) at the desired order in $\delta\hat{\mathbf{\Psi}}$. [43] showed that a series expansion in $\delta\hat{\mathbf{\Psi}}$ is roughly equivalent to a perturbation series in $1/N_r$, with higher connected moments of the inverse Wishart distribution corresponding to higher powers in $1/N_r$. We need to know the moments of $\mathcal{W}^{-1}$ up to quartic order [25] to express the expectation value of (5.2.17) at $O(1/N_r^2)$. We

quote the expressions for the $\mathcal{W}^{-1}$ moments from [43]:

$$\left\langle \delta\hat{\Psi}_I \delta\hat{\Psi}_J \right\rangle = \frac{\Psi_I \Psi_J + \gamma \Psi_{\{I}\Psi_{J\}}}{(\gamma-1)(2\gamma+1)} \tag{5.2.19}$$

$$\left\langle \delta\hat{\Psi}_I \delta\hat{\Psi}_J \delta\hat{\Psi}_K \right\rangle = \frac{\gamma^2 \Psi_{\{I}\Psi_J\Psi_{K\}}}{(\gamma-1)(\gamma-2)(\gamma+1)(2\gamma+1)} \tag{5.2.20}$$

$$\left\langle \delta\hat{\Psi}_I \delta\hat{\Psi}_J \delta\hat{\Psi}_K \delta\hat{\Psi}_L \right\rangle = \frac{\gamma^3(2\gamma^2-5\gamma+9)\Psi_{\{I}\Psi_J\}\Psi_{\{K}\Psi_{L\}}}{(\gamma-1)(\gamma-2)(\gamma-3)(2\gamma-1)(\gamma+1)(2\gamma+1)(2\gamma+3)} \tag{5.2.21}$$

The adopted notation is the following: we use a capital letter $I = (i_1, i_2)$ to indicate a pair of indexes i_1, i_2, and we use curly braces to indicate a symmetrization in the indexes

$$\Psi_{\{I}\Psi_{J\}} = \Psi_{i_1 j_1}\Psi_{i_2 j_2} + \Psi_{i_1 j_2}\Psi_{i_2 j_1} \tag{5.2.22}$$

In equations (5.2.19), (5.2.20) and (5.2.21), we kept only the terms which are of order $O(1/N_r^2)$. Looking at the structure of the expression (5.2.17) and at the expressions for the inverse Wishart moments, we conclude that the expectation value $\langle\hat{\mathbf{\Sigma}}_2\rangle$ must be be the sum of terms in the form $f_a(N_d, N_\pi)\mathbf{\Sigma}/N_r^a$, where f_a a polynomial of N_d, N_π. Each of these polynomials contains at least one factor proportional to $N_d - N_\pi$ since, if $N_d = N_\pi$, $\langle\hat{\mathbf{\Sigma}}_2\rangle = \mathbf{\Sigma}$. After expanding (5.2.17) at quadratic, cubic and quartic order in $\delta\hat{\mathbf{\Psi}}$ and carrying out the calculations, we can separate the contributions to $\langle\hat{\mathbf{\Sigma}}_2\rangle$ due to $O(\delta\hat{\mathbf{\Psi}}^n)$ terms as

$$(\delta\hat{\mathbf{\Psi}})^2 \to \frac{\gamma(N_d - N_\pi)\mathbf{\Sigma}}{(\gamma-1)(2\gamma+1)} \tag{5.2.23}$$

$$(\delta\hat{\mathbf{\Psi}})^3 \to -\frac{4(N_d - N_\pi)(1+N_\pi)\mathbf{\Sigma}}{N_r^2} \tag{5.2.24}$$

$$(\delta\hat{\mathbf{\Psi}})^4 \rightarrow \frac{3(N_d - N_\pi)(1 + N_\pi)\mathbf{\Sigma}}{N_r^2} \tag{5.2.25}$$

Combining (5.2.23), (5.2.24) and (5.2.25) we finally get

$$\left\langle \hat{\mathbf{\Sigma}}_2 \right\rangle = \left(1 + \frac{N_d - N_\pi}{N_r} + \frac{(N_d - N_\pi)(N_d - N_\pi + 2)}{N_r^2}\right)\mathbf{\Sigma} + O\left(\frac{1}{N_r^3}\right) \tag{5.2.26}$$

The result (5.2.26) has an important consequence: although parameter error bars forecast from simulations via (5.2.14) are unbiased, the scatter of the likelihood peak $\hat{\mathbf{p}}_0$ is larger than $\mathbf{\Sigma}$ by a factor of $\sim 1 + N_d/N_r$. This is always the case when we use a noisy estimate of feature covariance matrix obtained with (5.2.6). This means that, for high dimensional image features, estimation noise in the covariance matrix severely degrades parameter estimates, and the error bar forecast from simulations is an under–estimate. [42] proposed an empirical formula for $\langle \hat{\mathbf{\Sigma}}_2 \rangle$ which accurately reproduces numerical estimates of the parameter degradation:

$$\left\langle \hat{\mathbf{\Sigma}}_2 \right\rangle_{\text{empirical}} = \left(\frac{N_r - 2}{N_r + N_\pi - N_d - 2}\right)\mathbf{\Sigma} \tag{5.2.27}$$

Note that (5.2.27) reduces to (5.2.26) when expanded up to order $O(1/N_r^2)$. Figure 5.2 shows the results of a numerical experiment we performed using ensemble bootstrapping. We measured the constraint degradation of the Dark Energy equation of state parameter w_0. The Figure shows that, for ratios N_d/N_r close to unity, the scatter of the w_0 estimate is be significantly bigger than the forecast covariance $\mathbf{\Sigma}$ (see [44, 25]). This numerical degradation brings up the necessity of dimensionality reduction: high dimensional features likely contain more information about cosmology but, since their covariance matrix has

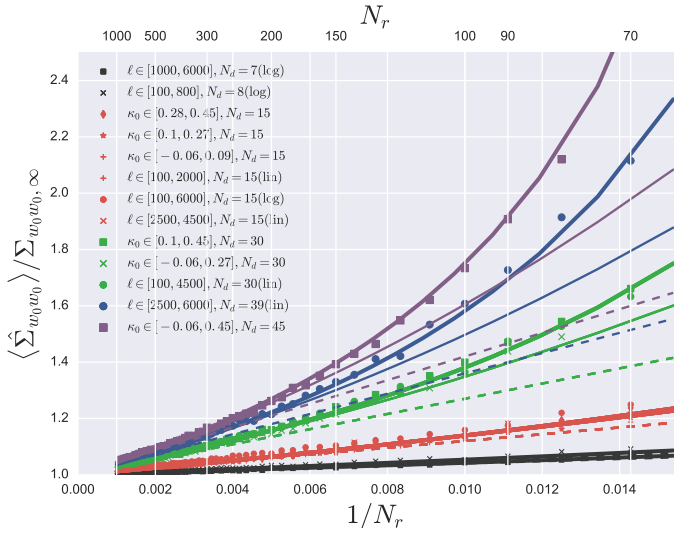

Figure 5.2: Expectation value of the w_0 peak scatter $\hat{\Sigma}_{w_0 w_0}$ as a function of the number of pseudo–independent realizations N_r used to measure the feature covariance matrix. We consider a variety of features with different dimensionality, including the κ power spectrum and peak counts. We show the numerical results obtained with a bootstrapping procedure (points), the $O(1/N_r), O(1/N_r^2)$ perturbation theory predictions from equation (5.2.26) (dashed and thin solid lines respectively) and the empirical result from equation (5.2.27) (thick solid lines). The asymptotic parameter covariance $\boldsymbol{\Sigma}_\infty$, which coincides with the true covariance $\boldsymbol{\Sigma}$, has been estimated with a linear regression of $\langle \hat{\boldsymbol{\Sigma}} \rangle_2$ versus $1/N_r$ using the large N_r tail.

to measured from simulations, constraint degradation results in larger error bars. A good compromise is to find a way to construct low dimensional features which retain as much information on cosmology as possible. We propose some possible recipes for this non trivial task later in the Chapter.

5.3 Pseudo–independence of realizations

The analytical results illustrated in § 5.1, § 5.2 are based on the assumption that the realizations in the κ ensembles are independent. Because these ensembles are built with the sampling procedure described in § 3.2.3, which makes use of N_s independent N–body simulations to construct a large number $N_r \gg N_s$ of WL fields, the realizations are all independent. Moreover, if N_s is small, it is not guaranteed that cosmic variance is sampled in an unbiased way. Given the size ($c/H_0 \sim 3\,\mathrm{Gpc}$) of the present Hubble horizon, this might be an issue for our simulations, which have a box size of $L_b \approx 250\,\mathrm{Mpc}/h$. The effect of biased sampling is evident in Figure 5.3, which shows the distribution of the κ power spectrum at selected ℓ values over different realizations. We can clearly see that, if the WL sampling is based on a single N–body simulation ($N_s = 1$), the peak of the distribution of $P_{\kappa\kappa}$ varies among ensembles. Different initial conditions for the N–body simulation lead to different estimates of the small scale power spectrum ($\ell \gtrsim 1000$). The same distinction is not evident on larger scales ($\ell \lesssim 400$). Figure 5.3 also shows that, with the chosen box size, $N_s = 5$ is sufficient to obtain an unbiased sample of the κ power spectrum up to $\ell \approx 5000$. Another aspect of biased feature sampling is shown in the top panel of Figure 5.4, which shows the mean of selected features as a function of the number of independent simulations N_s. The plot shows that for features that trace density fluctuations in the linear

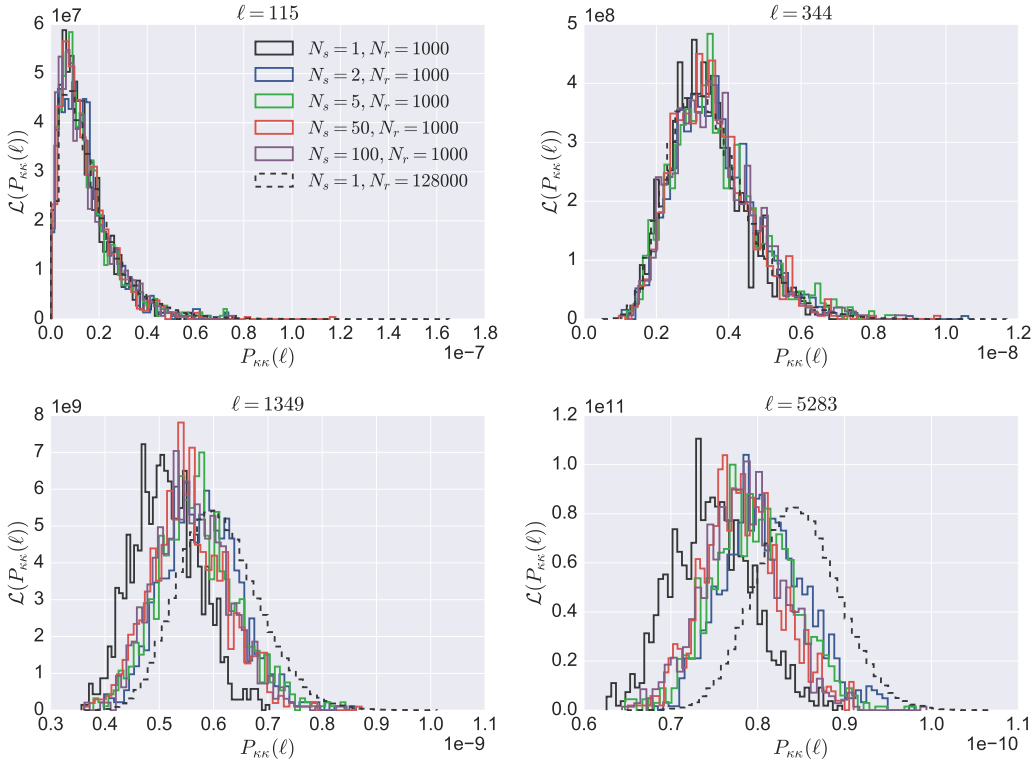

Figure 5.3: Distribution of the κ power spectrum at four distinct values of ℓ. We plot the histogram of 1000 $P_{\kappa\kappa}$ realizations in ensembles built with different N_s (solid colored lines). We also show the distribution of $\sim 10^5$ $P_{\kappa\kappa}$ realizations in an ensemble built from a single N–body simulation ($L_b = 240\,\mathrm{Mpc}/h$) (dashed black line). The simulations on which this Figure is based are taken from the `CovarianceBatch` set (see Appendix).

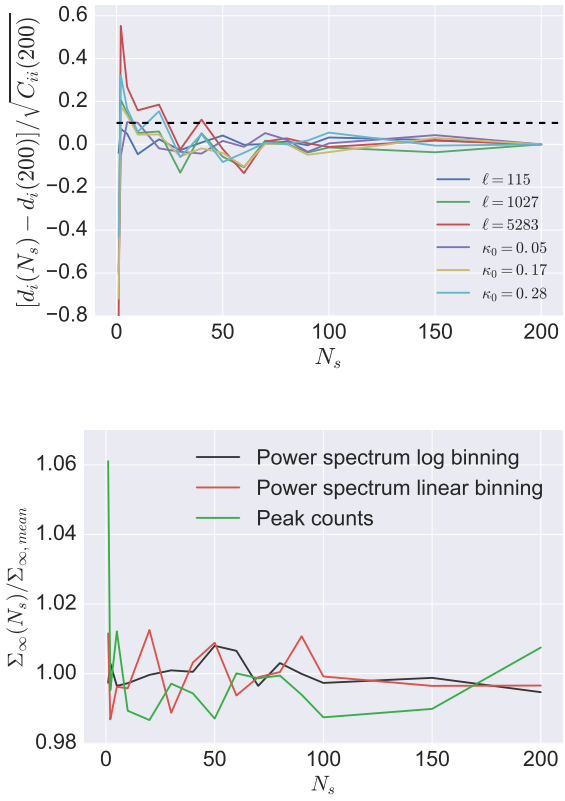

Figure 5.4: Top panel: mean feature measured from $N_r = 1000$ realizations drawn from ensembles build with varying N_s. We show the κ power spectrum measured at three selected ℓ values and the peak counts of three different heights κ_0 (colored lines). The mean feature is plotted in units of the statistical error measured from the ensemble variance. We also draw a dashed black line which shows the tolerance of 10% of the statistical error. Bottom panel: asymptotic parameter variance on w_0 plotted against the number of independent simulations N_s used to construct the WL ensembles. The asymptotic variance has been obtained with a linear regression of the bootstrapped $\langle\hat{\boldsymbol{\Sigma}}_2\rangle$ versus $1/N_r$ for large N_r. The trends are shown in units of the mean over N_s for two different binning choices of the power spectrum (black, red) and for the peak counts (green). The simulations on which this Figure is based are taken from the `CovarianceBatch` set (see Appendix).

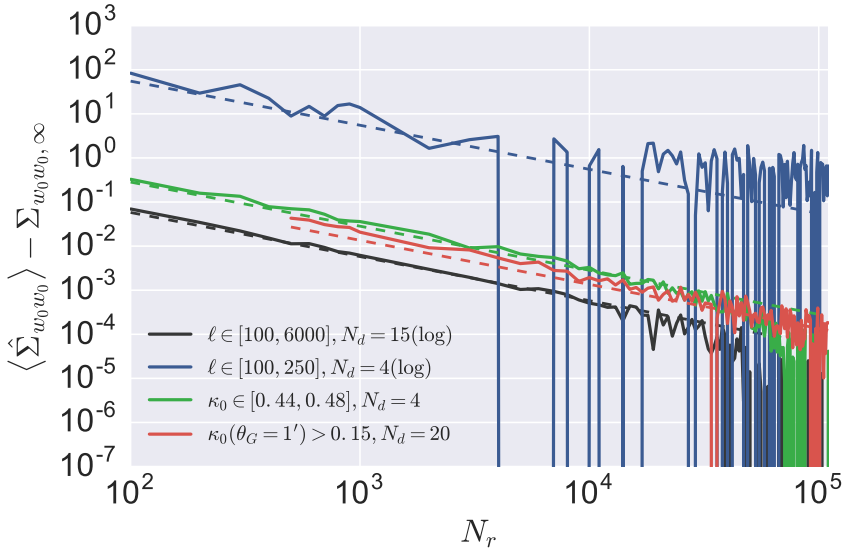

Figure 5.5: Degradation in the w_0 constraint as a function of N_r for different choice of features. The features measured from ensembles built with $N_s = 1$. The asymptotic variance $\mathbf{\Sigma}_{w_0 w_0, \infty}$ was estimated using the value of $\langle \hat{\mathbf{\Sigma}}_2 \rangle$ at $N_r = 128,000$. We show the trends for small (black) and large (blue) scale power spectra and large threshold peak counts for non–smoothed (green) and $1'$ smoothed (red) κ images. The simulations on which this Figure is based are taken from the `CovarianceBatch` set (see Appendix).

regime, such as power spectra at small ℓ and low height peaks, as few as $N_s = 2$ simulations (with $L_b = 240\,\mathrm{Mpc}/h$) are sufficient for the bias to be within 10% of the statistical error. On the contrary, for features that trace the non–linear cosmic density such as power spectra at high ℓ and high peaks, the required number of N–body simulations (for the same 0.1σ reference tolerance) is of the order of 10. The lower panel of Figure 5.4 shows that the pseudo–independence of κ realizations at small N_s does not affect the estimation of the asymptotic parameter variance $\mathbf{\Sigma}$, which is correctly obtained at $N_s = 2$ already (modulo statistical fluctuations).

If $N_s = 1$, the WL realizations cannot be considered all independent, as Figure 5.5

shows. The Figure highlights the fact that, when the WL sampling is based on a single N–body simulation, features measured from the κ ensemble start to be correlated for large N_r. Regardless of which feature one considers, the error bar degradation $\langle\hat{\mathbf{\Sigma}}_2\rangle - \mathbf{\Sigma}$ behaves asymptotically as $1/N_r$ in the limit of independent realizations. What our numerical experiment shows, on the other hand, is a flattening of the trend at high N_r, hinting to correlations among the realizations in the ensemble. The $1/N_r$ behavior is broken at different N_r depending on which feature we are looking at. Large scale κ power spectra drawn from a single box can be considered independent for $N_r < \text{few} \times 10^3$, while non–linear statistics, such power spectra at high ℓ and peak counts, are independent up to $N_r < \text{few} \times 10^4$. These numbers should be interpreted as orders of magnitude and are referred to the size of the boxes $L_b = 240\,\text{Mpc}/h$ used in this work. Different box sizes will likely modify the scale N_r on which deviations from the $1/N_r$ behavior start to appear [45, 25].

5.4 Dimensionality reduction

In the previous sections we discussed how noise in the feature covariance matrix degrades the inference of cosmological parameters. A way to mitigate this effect (which is expressed by equations (5.2.26) and (5.2.27)) is to use a large number N_r of independent WL realizations. In section § 5.3, however, we saw that there is a limit on the number of independent realizations one can generate from a single N–body simulation. Because the degradation in the error bars, at first order, is proportional to the feature dimensionality N_d, techniques that capture the same cosmological information with a smaller number of dimensions $N_c < N_d$ assume particular relevance. In this section we will explore one of such techniques, which takes the name of *Principal Component Analysis* (PCA) [46]. PCA projects image features

onto a lower dimensional space which hopefully retains most of the original information. We indicate with $\mathbf{D}$ the $N_M \times N_d$ feature matrix, in which each of the N_M rows represents an image feature in a different ΛCDM model. We perform a SVD decomposition [26, 46] of $\mathbf{D}$ by writing it in the form

$$\mathbf{D} = \mathbf{L}\mathbf{\Lambda}\mathbf{R} \tag{5.4.1}$$

where $\mathbf{L}$ is $N_M \times K$, $\mathbf{R}$ is $K \times N_d$ and $\mathbf{\Lambda}$ is a diagonal $K \times K$ matrix. We adopted the notation $K = \min(N_d, N_M)$. The diagonal components of $\mathbf{\Lambda} = (\Lambda_1, ..., \Lambda_K)$, assumed sorted from biggest to smallest, take the name of *singluar values* and represent the variance of the coordinates defined by the basis vectors in $\mathbf{R}$ over the N_M models. The idea behind PCA is to project the feature space onto the first $N_c < N_d$ basis vectors, defined as the rows of $\mathbf{R}$, which have the largest Λ_i. The remaining coordinates are discarded, as they are associated with numerical noise with negligible information about cosmology. Because N_d components of the feature vector can each have a different scale (think about $P_{\kappa\kappa}$ for example), in order not to exclude some of them because of their measure units, a whitening operation is usually performed before the SVD. The whitened feature matrix $\mathbf{D}^W$ is defined to be

$$D^W_{md} = \frac{D_{md} - \mu_d}{\sigma_d} \tag{5.4.2}$$

In equation (5.4.2), we introduced N_d arbitrary location and scale parameters μ_d, σ_d, which re–center and normalize $\mathbf{D}$ so that each dimension has the same magnitude. Popular choices for μ_d, σ_d are, respectively, the mean and standard deviation of the rows of $\mathbf{D}$ [46]. After the whitening operation, we perform the SVD of $\mathbf{D}^W$ and calculate the singular values $\mathbf{\Lambda}$ and the basis vectors $\mathbf{R}$. We then select the N_c biggest singular values and

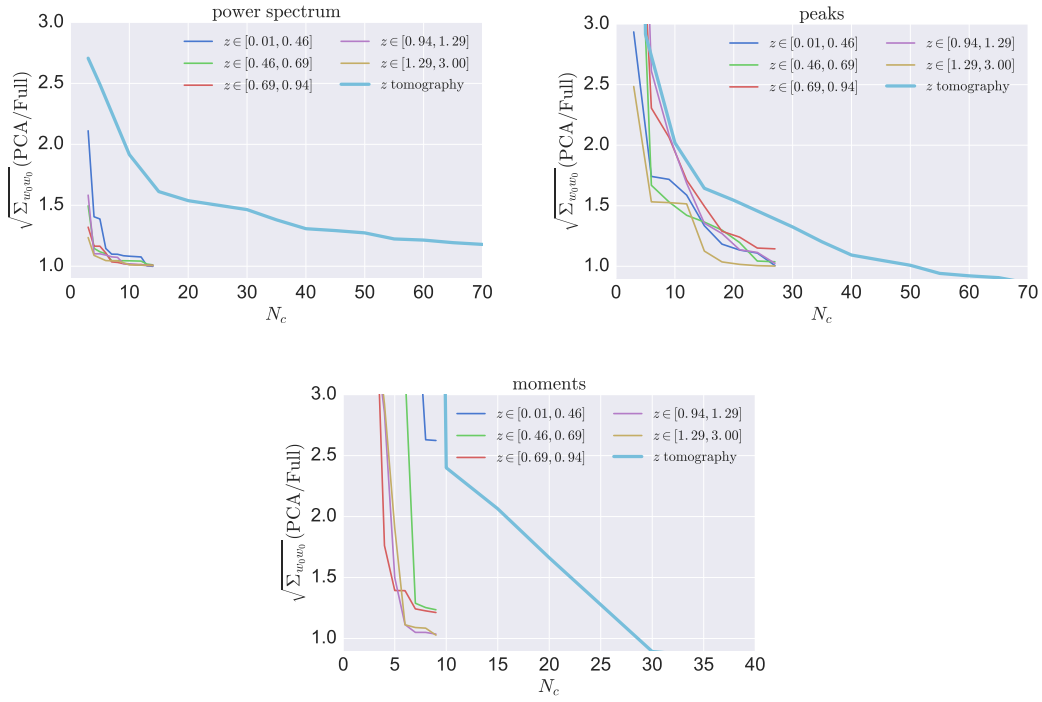

Figure 5.6: 1σ constraint on w_0 as function of the number of PCA components N_c used in the projection. We show the case for the κ power spectrum (top left) binned with 15 ℓ bins per redshift, the κ peak counts (top right) binned in 45 κ height bins per redshift, and the 9 moments (bottom) defined in (4.5.4), (4.5.5) and (4.5.6). We consider the single redshift case (thin lines) and the tomographic case (thick line). The constraints are plotted in units of the non–projected constraint, obtained from the full feature space. The feature covariance matrix has been measured from an ensemble made of $N_r = 16,000$ realizations in order to ignore constraint degradation effects. We use $N_M = 100$ different choices of $(\Omega_m, w_0, \sigma_8)$ to perform the PCA [47], and we choose the whitening parameters as $\mu_d = \sigma_d = \sum_p D_{pd}/N_M$.

define $\mathbf{R}(N_c)$ as the matrix made by the first N_c rows of $\mathbf{R}$. We project the image feature $\mathbf{d}$ from the high dimensional space to the lower dimensional space using PCA via a matrix multiplication:

$$\mathbf{d}_{\rm PCA}(N_c) = \mathbf{R}(N_c)\left(\frac{\mathbf{d}-\boldsymbol{\mu}}{\boldsymbol{\sigma}}\right) \tag{5.4.3}$$

Because the PCA projection changes with different specifications of the external parameters μ_d, σ_d, this type of technique is not scale invariant. Nevertheless, we will see it will prove useful in parameter inferences from WL. Modern surveys, such as LSST [3], are planning to use redshift tomography of image features in order to get tight constraints on cosmology. Tomography greatly increases the dimensionality of the feature space. If tracer galaxies are divided in N_z redshift bins, the feature dimensionality N_d increases at least by a factor of N_z, which can become N_z^2 if the case we consider cross power spectra of κ across different z bins. Figure 5.6 shows an application of PCA to forecasts of ΛCDM parameter error bars obtained from redshift tomography of an LSST–like survey [47]. The Figure shows that using the projection of single redshift features, even if the dimensionality is halved, we still get a constraint on w_0 which is within $\sim 15-20\%$ of the value we get in the non–projected case. We achieve even better performance in the tomography case. A wide variety of dimensionality reduction techniques have been proposed in the literature (see [46] for a non–comprehensive list), and their application to WL cosmology will be investigated in future work.

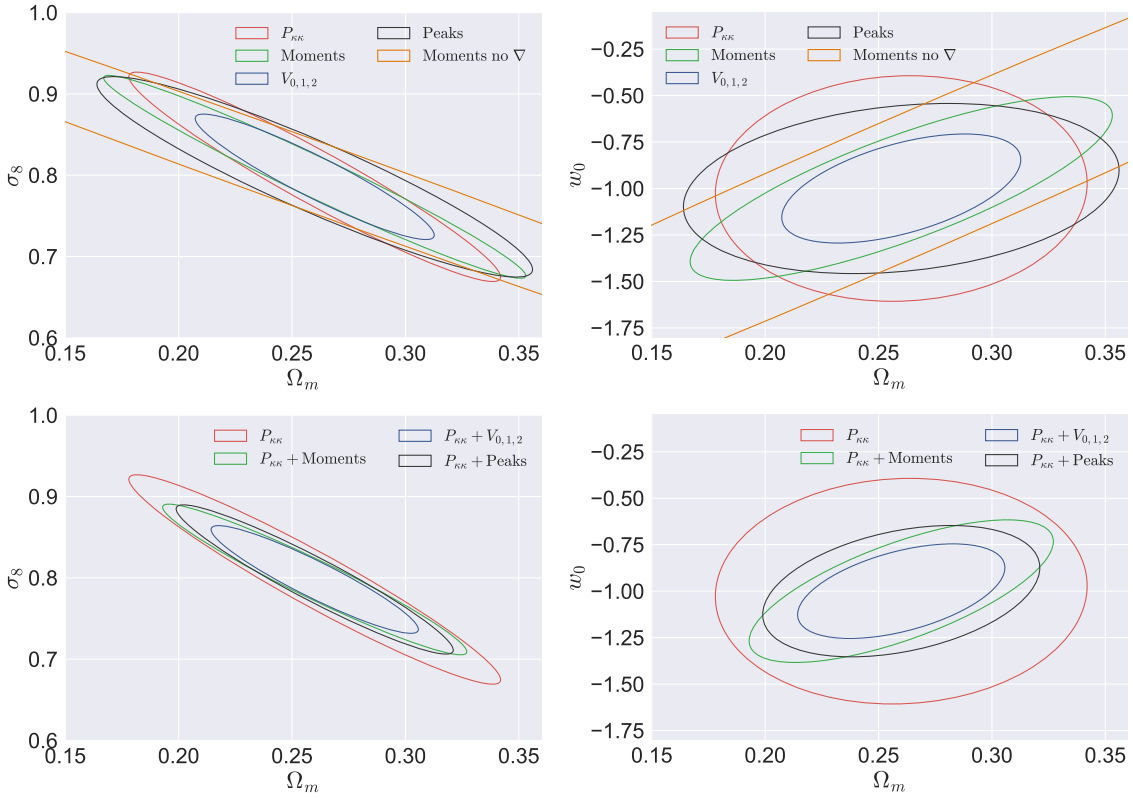

Figure 5.7: 1σ (68% confidence level) constraints on (Ω_m, σ_8) (left) and (Ω_m, w_0) (right) from a single $(3.5\,\mathrm{deg})^2$ WL field of view. The elliptical contours are based on the parameter covariance matrix (5.1.8). The feature covariance matrix $\hat{\mathbf{C}}$ has been estimated from 1000 realizations of the fiducial cosmology and has been corrected for the bias in (5.2.14). In the top panels we show the constraints obtained using the following features: $P_{\kappa\kappa}$ ($\ell \in [10^2, 10^5]$, $N_d = 100$), the 9 κ moments described in § 4.5, Minkowski functionals ($\kappa_0 \in [-2\sigma, 2\sigma]$, $N_d = 100$) and peak counts ($\kappa_0 \in [-2\sigma, 5\sigma]$, $N_d = 100$). In the bottom panels we show constraints obtained by combining $P_{\kappa\kappa}$ with each of the other three features. Shape noise for a constant source redshift $z_s = 2$ with $n_g = 15\,\mathrm{galaxies/arcmin}^2$ has been included.

5.5 Constraints from Weak Lensing

In this section we want to give the reader an idea of the constraining power of WL on ΛCDM. Moreover, we want to show higher order image features (described in Chapter 4) complement the κ power spectrum adding new information about cosmology. Error bar forecasts on (Ω_m, σ_8) and (Ω_m, w_0) are shown in Figure 5.7. The Figure displays constraints from both individual and combined features where the combinations include higher order statistics and the power spectrum. The bias on the $\mathbf{\Sigma}$ estimate that arises from high N_d (see equation (5.2.14)) has been corrected for. We can see that, for source galaxies place at constant redshift with an angular density of $n_g = 15\,\mathrm{galaxies/arcmin}^2$, κ peak counts and moments have a constraining power which is comparable with $P_{\kappa\kappa}$. We also observe that Minkowski functionals deliver constraints which are about a factor of 2 better than the ones provided by the moments alone (a hint about the fact that these two descriptors are not equivalent can be found in Chapter 4).

Regarding the moments of κ, we can see that most of the cosmological information is contained in moments with κ gradients (i.e. $\mu_m^{(n)}$ with $m > 0$) which probe small scale spatial correlations in addition to the PDF of κ.

From the bottom panel of Figure 5.7, we observe that higher order features complement $P_{\kappa\kappa}$ in giving better constraints on cosmology. The error bar improvement can be as big as a factor of 2 for the Minkowski functionals combined with the power spectrum. In the next Chapter we study a real WL dataset and its cosmological information.

Chapter 6

An application to data: the CFHTLenS galaxy survey

In this Chapter we discuss the application of WL analysis to the data contained in the Canada France Hawaii Telescope LenS survey catalogs [48, 49, 50] (CFHTLenS in the remainder of this work). The catalogs are publicly available. We start by reviewing the reduction procedure we used to convert row–ordered data to κ maps. As a next step, we present a set of cosmological simulations tailored to the CFHTLenS catalogs, which are then used to build a feature emulator. We use this emulator as a forward model to produce ΛCDM parameter inferences.

6.1 CFHTLenS catalogs

The CFHTLenS galaxy survey covers an area of $154\,\mathrm{deg}^2$, which divided in four patches of size 64,23,44 and $23\,\mathrm{deg}^2$ respectively. The publicly released catalogs, created with the SExtractor software [51], contain information on galaxy photometric redshifts (see [52] for

a detail on the estimation procedure) and shapes extracted with `lensfit` [48, 49]. After applying a redshift cut $0.2 < z < 1.3$ to the source galaxies, and after considering only the ones with positive weight w (larger w indicates smaller shape measurement uncertainty), we are left with roughly $N_g = 4.2$ million objects, which are distributed over an area of $124.7\,\mathrm{deg}^2$. This corresponds to an average galaxy density of $n_g \approx 9.3\,\mathrm{galaxies/arcmin}^2$. The catalog size is further reduced by 25% if sub–patches with non negligible star–galaxy correlations are rejected [53]. These correlations are introduced by imperfect Point Spread Function (PSF) removal procedures. Using the information contained in the publicly available catalogs, we can estimate the corresponding κ profile making use of the KS procedure (2.2.28) applied to the cosmic shear estimated from ellipticity measurements. We create smooth ellipticity maps using an histogram approach (see [54, 55])

$$\bar{\mathbf{e}}(\boldsymbol{\theta}) = \frac{\sum_{i=1}^{N_g} W(|\boldsymbol{\theta} - \boldsymbol{\theta}_i|)\mathrm{w}_i(\mathbf{e}_i - \mathbf{c}_i)}{\sum_{i=1}^{N_g} W(|\boldsymbol{\theta} - \boldsymbol{\theta}_i|)\mathrm{w}_i(1 + m_i)} \tag{6.1.1}$$

In equation (6.1.1), $\boldsymbol{\theta}_i, \mathrm{w}_i, \mathbf{e}_i, \mathbf{c}_i, m_i$ refer to the sky position, weight, observed ellipticity, additive and multiplicative ellipticity correction of the i–th galaxy. The reconstructed images have been convolved with a Gaussian window

$$W(\boldsymbol{\theta}) = \frac{1}{2\pi\theta_G^2} \exp\left(-\frac{\theta^2}{2\theta_G^2}\right) \tag{6.1.2}$$

with size $\theta_G = 1'$. We vary the size of the smoothing window to $1.8'$ and $3.5'$ for testing purposes. We use the estimate $\boldsymbol{\gamma}(\boldsymbol{\theta}) = \bar{\mathbf{e}}(\boldsymbol{\theta})$ apply equation (2.2.28) to construct the κ images which will be used in the inference of parameters. We divide the survey area in 13 square sub–fields of $12\,\mathrm{deg}^2$ angular size. We sample each subfield with 512^2 evenly spaced square pixels. The reduced data undergoes further compression: image features

(see Chapter 4) are measured from each sub–field and then averaged over the 13 sub–fields. Masked pixels in the maps are not an issue when measuring κ moments and Minkowski functionals, as both statistics can be evaluated with local estimators in real space (see § 4.2, § 4.5). Masking is an issue for the power spectrum, which requires non–local operations such as FFTs. We deal with this by filling the masked pixels with $\kappa = 0$ and restricting the ℓ range in the analysis to exclude multipoles which correspond to the typical size of the masks. In any case, when analyzing observations, masking effects are included in the forward model in order to minimize bias in the parameter constraint. The extracted features are then compared to the simulated ones in a Bayesian fashion (see Chapter 5) to obtain posterior distributions for the ΛCDM parameter triplet $(\Omega_m, w_0, \sigma_8)$. In the next section we describe the simulations used for constructing of the CFHTLenS feature emulator.

6.2 Emulator

Emulators encode the relation between image features and cosmological parameters. We sampled the ΛCDM parameter space using N_M points and we ran the simulation pipeline described in § 3.4 on each combination of parameters. We then measure the mean feature in each cosmology and we infer the mean feature for an arbitrary set of parameters (not included in the N_M samples) using interpolation.

6.2.1 Cosmological parameter sampling

We consider a subset of $N_\pi = 3$ parameters $\mathbf{p} = (\Omega_m, w_0, \sigma_8)$, seeking a way to uniformly sample it with the constraint that no parameter is repeated twice. This scheme takes the name of *latin hypercube* [56]. One way to implement the latin hypercube scheme is to

build a N_π–dimensional rectangular box that contains the sampled points and normalize it to $[0,1]^{N_\pi}$ for simplicity. We set the number N_M of cosmological models in the box to 91. Following [56, 54], we define a cost function

$$\mathcal{C}(\mathbf{P}) = \frac{2{N_\pi}^{1/2}}{N_M(N_M-1)} \sum_{i<j} \frac{1}{|\mathbf{P}_i - \mathbf{P}_j|} \tag{6.2.1}$$

where $\mathbf{P}$ is a $N_M \times N_\pi$ matrix that contains information on the sample points in $[0,1]^{N_\pi}$. The sum runs over all $N_M(N_M-1)/2$ sample pairs. In order to sample the hypercube uniformly, we seek a configuration $\mathbf{P}$ that minimizes the cost function (6.2.1) with the latin hypercube constraint. Because $\mathcal{C}$ is proportional the Coulomb potential energy of N_M unit point charges confined in a box, its minimum leads to a statistically isotropic configuration. The simplest latin hypercube arrangement is the design $\mathbf{P}^0$, in which the points are arranged on the diagonal of the hypercube

$$\mathbf{P}^0_i = \frac{i}{N_M} \underbrace{(1,1,...,1)}_{N_\pi} \tag{6.2.2}$$

This trivial arrangement is far from optimal. A possible heuristic method to find out the optimal configuration $\mathbf{P}$ which minimizes (6.2.1) is simulated annealing [57]. Since this algorithm is too computationally expensive for our purposes, we resort on a less accurate but faster heuristic scheme, consisting in the following steps:

1. Start from the diagonal design $\mathbf{P}^0$

2. Pick a random pair of points (i,j) among the $N_M(N_M-1)/2$ available, pick a random parameter p among the N_π available

3. Swap P_{ip} with P_{jp} (the swap preserves the latin hypercube property), recompute the

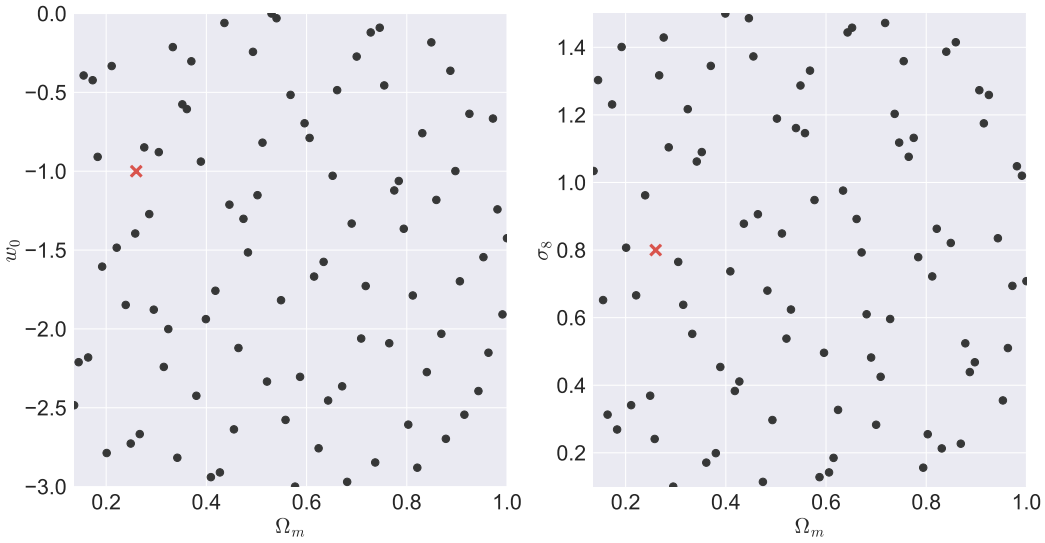

Figure 6.1: Distribution of the $(\Omega_m, w_0, \sigma_8)$ sample triplets. We show both the (Ω_m, w_0) (left) and the (Ω_m, σ_8) (right) projections. The black points correspond to the $N_M = 91$ latin hypercube models (`CFHTEmu1` simulations), and the red cross correspond to the fiducial ΛCDM parameters read from Table 1.1 (`CFHTcov` simulations). The design results from 10^5 iterations of the heuristic procedure described in § 6.2.1.

cost function $\mathcal{C}$ (this is done in $O(1)$ time taking advantage of the separability of (6.2.1))

4. If the cost is lower, keep the swap, otherwise undo it, reverting to the previous configuration

5. Re–iterate the procedure starting from point 2.

After several iterations, we are left with a latin hypercube design which samples the parameter space approximately uniformly. The last step is to rescale the parameter coordinates from the $[0, 1]^{N_\pi}$ bounds to their originally intended values. The design we used in the present analysis is shown in Figure 6.1.

6.2.2 Simulations

We run one N–body simulation with $N_p = 512^3$, $L_b = 240\,\mathrm{Mpc}/h$ for each of the cosmologies shown in Figure 6.1. These simulations (referred to as `CFHTemu1`) share the random seed used to generate the initial conditions. We also run 50 independent N–body simulations (referred to as `CFHTcov`) for the fiducial cosmology indicated as a red cross in Figure 6.1. We used the fiducial dataset to estimate feature covariance matrices. We generate WL shear catalogs by ray–tracing from the observed galaxy sky positions and to the real ones at the redshifts read from in the CFHTLenS catalog. In order to correctly forward model observations, we add the intrinsic galaxy ellipticity to the WL signal obtained from ray–tracing. This is done by looking at the CFHTLenS catalog itself, assuming that the WL signal contained in the observations is much smaller than the intrinsic ellipticity noise. We take the catalog complex ellipticity e of each galaxy and we rotate it by a random angle ϕ by performing the substitution

$$e \to e\exp(2i\phi) \tag{6.2.3}$$

We then add this intrinsic ellipticity to the simulated WL shear. The random rotation prevents a double counting of the WL signal, whose spatial coherence is destroyed by the rotation. The forward modeled catalogs are defined by

$$e(\mathbf{p}) = \gamma(\mathbf{p}) + e\exp(2i\phi) \tag{6.2.4}$$

We then performed the KS inversion and consequent feature extraction steps.

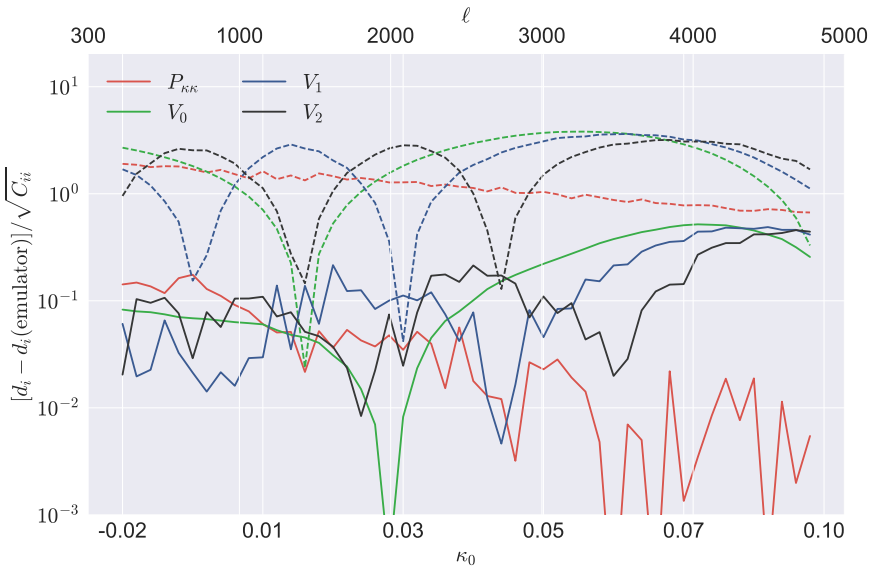

Figure 6.2: Test of the emulator accuracy for the CFHTLenS κ power spectrum $P_{\kappa\kappa}$ (red) and Minkowski functionals V_k (green, blue, black). We use the `CFHTemu1` simulations to produce a feature emulator which is then tested against the mean feature measured in the `CFHTcov` simulations (solid lines). We also compare the mean `CFHTcov` feature to an emulated feature with $(\Omega_m, w_0, \sigma_8) = (0.8, -1.0, 0.5)$ (dashed lines). The differences are plotted in units of the statistical error in each of the N_d feature dimensions.

6.2.3 Interpolation

Using the `LensTools` feature extraction routines, we construct the $N_M \times N_d$ feature matrix $\mathbf{D}$ (defined in § 5.4), which contains information on the mean feature in each of the N_M cosmologies. We used $\mathbf{D}$ to infer the mean feature in arbitrary cosmologies not necessarily included in the N_M samples. Although we could adopt sophisticated approaches based on Gaussian Processes (see [56]), for the purpose of this analysis we found it convenient to use a Radial Basis Functions (RBF) interpolation scheme. We model the cosmology dependence of feature $\mathbf{d}$ as

$$d_i(\mathbf{p}) = \sum_{j=1}^{N_M} \lambda_{ij} f(|\mathbf{p} - \mathbf{p}_j|; R) \tag{6.2.5}$$

where $\mathbf{p}_i$ is the i–th sampled ΛCDM parameter triplet and f is the multiquadric function

$$f(x; R) = \sqrt{1 + \left(\frac{x}{R}\right)^2} \tag{6.2.6}$$

We chose the smoothing parameter R as the average distance between the `CFHTemu1` points

$$R = \frac{2}{N_M(N_M - 1)} \sum_{i<j} |\mathbf{p}_i - \mathbf{p}_j| \tag{6.2.7}$$

The interpolation to an arbitrary cosmology $\mathbf{p}$ can be performed once the weights λ_{ij} are known. The weights must obey the constraint $d_i(\mathbf{p}_j) = D_{ji}$ for each index pair (i, j). This leads to the expression

$$\boldsymbol{\lambda} = [\mathbf{f}(R)^{-1}\mathbf{D}]^T \tag{6.2.8}$$

where we defined the $N_M \times N_M$ matrix $f_{ij}(R) \equiv f(|\mathbf{p}_i - \mathbf{p}_j|; R)$. A test on the accuracy of the feature emulator $\mathbf{d}(\mathbf{p})$ is displayed in Figure 6.2: the plot shows that features in the fiducial cosmology can be emulated with an accuracy that is within 10% of the corresponding statistical error. We used the emulated feature $\mathbf{d}(\mathbf{p})$ as the forward model in Bayesian parameter inference defined by equation (5.1.1).

6.3 Parameter inference

In this section we present the main results of this investigation, which consist in the constraints on the $(\Omega_m, w_0, \sigma_8)$ parameter triplet from CFHTLenS data using higher order statistics. The features used include the κ power spectrum $P_{\kappa\kappa}$, the Minkowski functionals V_k of the excursion sets and the κ moments defined in (4.5.4), (4.5.5) and (4.5.6). [55], on the other hand, focused on the κ peak counts. We built the feature space with $N_d = 50$ linearly spaced multipoles $\ell \in [300, 5000]$ for the power spectrum and $N_d = 50$ linearly spaced thresholds $\kappa_0 \in [-0.04, 0.12]$ for the excursion sets. Taking advantage of the low dimensionality of the parameter space ($N_\pi = 3$), we were able to compute the parameter likelihood $\mathcal{L}(\mathbf{p}|\mathbf{d})$ explicitly, using equation (5.1.1), on a regularly spaced three dimensional grid of parameters. Using the grid values of $\mathcal{L}$, we found the parameter confidence levels $\mathcal{L}_N$ using equation (5.1.3) in a binary search algorithm. We were mostly interested in the 1σ level $\mathcal{L}_1$.

6.3.1 PCA projection

In order to avoid constraint degradation issues, as discussed in § 5.2, we performed a PCA projection on the feature space following the guidelines of § 5.4. We used the information contained in the $N_M = 91$ cosmologies that make up the `CFHTemu1` simulation suite. Figure 6.3 shows the singular values Λ_i obtained from the SVD procedure (5.4.1) applied to the κ power spectrum, Minkowski functionals and moments. In the right panel we can clearly see that the first few components ($N_c \sim 3$) are already able to capture more than 99.5% of the feature variance across the N_M cosmologies, hence suggesting the possibility of an efficient compression of the feature space. Because the optimal number of compo-

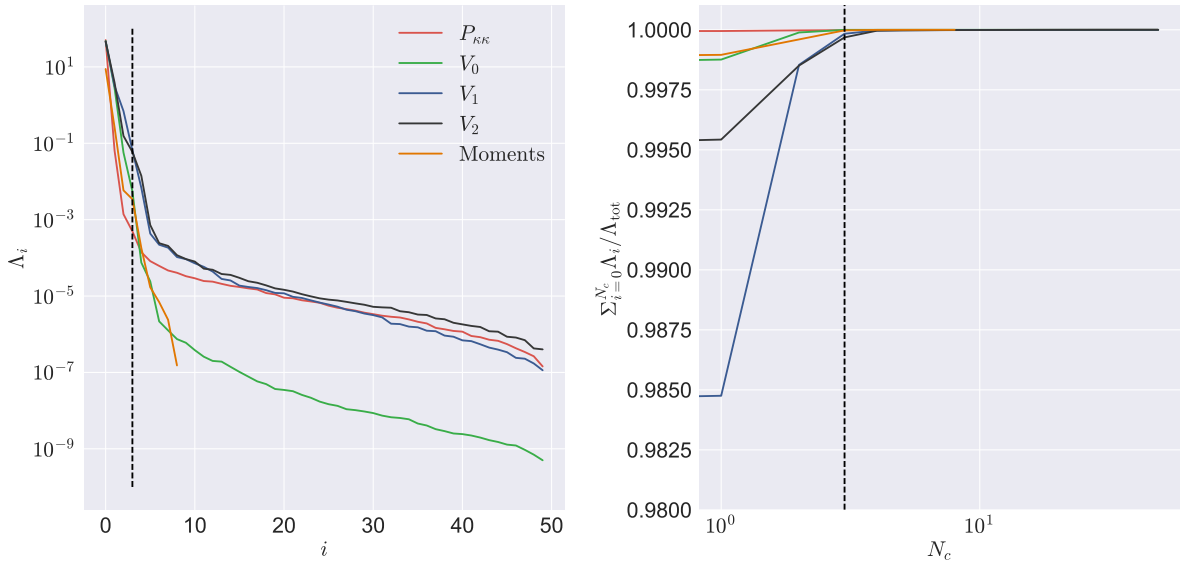

Figure 6.3: Singular values Λ_i from the SVD of $\mathbf{D}$ (left panel) and their cumulative sums in units of the total variance (right panel), as a function of the component number. We show the cases for the κ power spectrum (red), Minkowski functionals V_k (green, blue, black) and κ moments (orange). A vertical black dashed line in correspondence of $N_c = 3$ has been drawn for reference. The whitening factors μ_d, σ_d have been chosen as the mean and standard deviation of the feature matrix $\mathbf{D}$ across the N_M models.

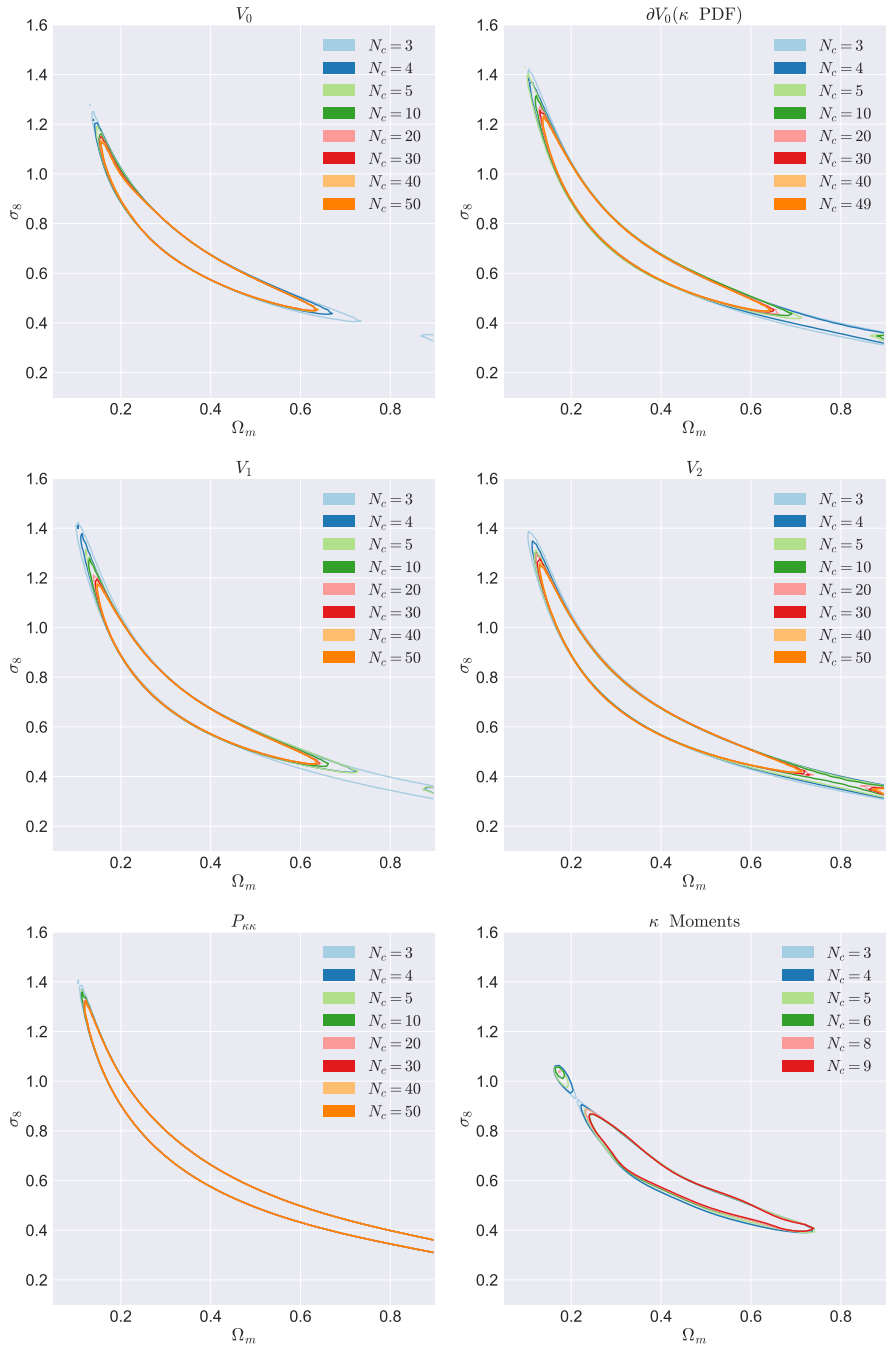

Figure 6.4: Robustness test on the number of PCA components N_c necessary to constrain the (Ω_m, σ_8) doublet. We show the cases for the κ power spectrum, PDF, Minkowski functionals and moments (left to right, top to bottom) and denote different values of N_c with different colors. Confidence contours are calculated from the parameter likelihood $\mathcal{L}(\Omega_m, w_0, \sigma_8)$ marginalized over w_0.

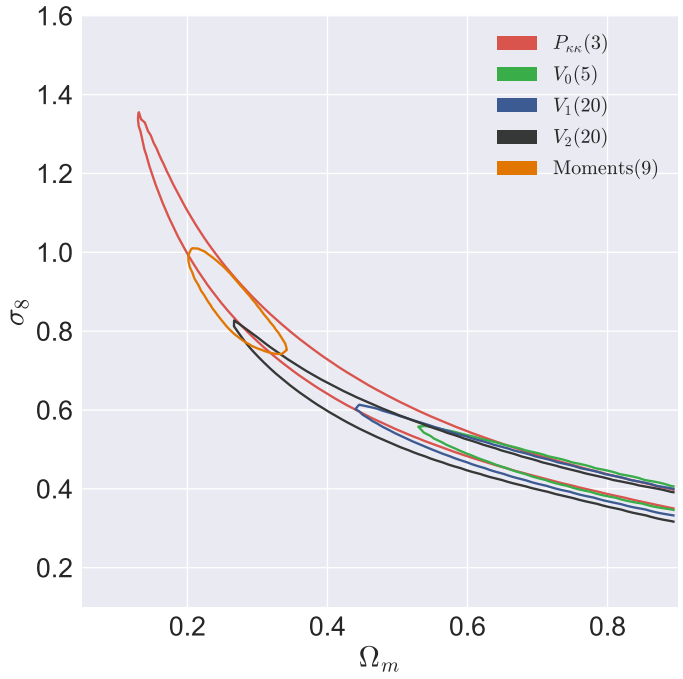

Figure 6.5: 1σ (68% confidence level) constraints on (Ω_m, σ_8) from CFHTLenS using the κ power spectrum (red), Minkowski functionals (green, blue, black) and κ moments (orange). The number N_c of principal components is indicated in parentheses. Confidence contours are calculated from the parameter likelihood $\mathcal{L}(\Omega_m, w_0, \sigma_8)$ marginalized over w_0.

nents N_c is not known a priori, we performed a robustness test on the (Ω_m, σ_8) constraint by varying N_c and observing how the 1σ confidence contour varies in response. We used this test (which is confined to the simulations and does not include CFHTLenS observations) as a way to select the smallest N_c for which the contour size stabilizes. The results of this test can be seen in Figure 6.4, which shows the optimal number of principal components for different features. N_c ranges from 3 for $P_{\kappa\kappa}$ to 5 for V_0 and 20 for $V_{1,2}$. For the moments of κ, we keep the full feature space with $N_c = 9$.

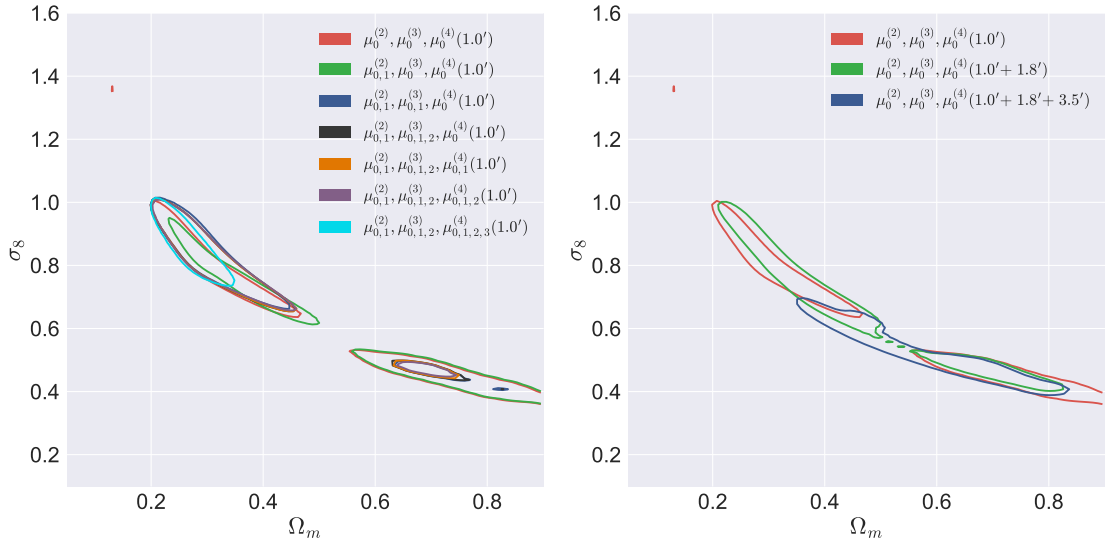

Figure 6.6: Breakdown of the 1σ constraint on (Ω_m, σ_8) using the CFHTLenS κ moments. We show different combinations of moments measured from κ maps smoothed with $\theta_G = 1'$ (left panel) and combination of single point moments $\mu_0^{(n)}$ measured from κ maps smoothed with different smoothing scales $\theta_G = 1', 1.8', 3.5'$ (right panel). The definitions of the moments $\mu_m^{(n)}$ are contained in § 4.5.

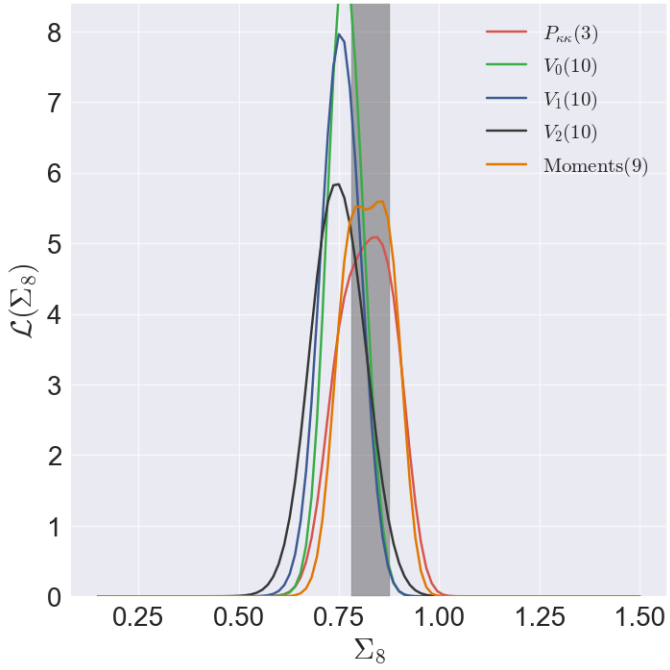

Figure 6.7: Σ_8 likelihood (marginalized over (Ω_m, w_0)) obtained from CFHTLenS observations using the κ power spectrum (red), Minkowski functionals V_k (green, blue, black) and κ moments (orange). The number N_c of principal components is indicated in parentheses in the legend. We also denote, with a gray band, the 1σ constraint on Σ_8 found by Planck [14] as a consistency check.

6.3.2 Density fluctuations

In this section we discuss how CFHTLenS constrains the Dark Matter density parameter Ω_m and the amplitude of the initial density fluctuations σ_8. It is evident from Figure 6.5 that the κ moments are the most efficient in constraining (Ω_m, σ_8) because of both precision and absence of bias. The power spectrum constraint is degraded by a well known degeneracy between Ω_m and σ_8, evident in the definition of the lensing density (3.2.23). We can also say that the constraint from Minkowski functionals is affected from uncorrected residual systematics in the CFHTLenS catalogs. These residuals, combined with the degeneracy, shift the peak of the parameter likelihood towards the unphysical large Ω_m, low σ_8 region.

Figure 6.6 shows the breakdown of the (Ω_m, σ_8) constraint obtained from different sets of κ moments. In agreement with what stated in § 5.5, we find that most of the constraining power comes from moments which include gradients of κ ($\mu_m^{(n)}$ with $m > 0$). We also observe that a significant amount of cosmological information is carried by moments which are quartic in κ, as [58] also conclude. The right panel of Figure 6.6 shows that, for the sake of constraining Ω_m, σ_8, combining one point moments $\mu_0^{(n)}$ with different smoothing scales is not as effective as using gradient moments.

Although there is a degeneracy between Ω_m and σ_8, the combination of parameters $\Sigma_8 = \sigma_8(\Omega_m/0.27)^\alpha$ can be tightly constrained upon a suitable choice for the exponent α, as different values of α map to different directions in the (Ω_m, σ_8) plane. Using the parameter likelihood $\mathcal{L}(\Omega_m, w_0, \sigma_8)$, we can compute the expectation value $\mathbb{E}$ and variance $\mathbb{V}$ of Σ_8. The optimal α is computed by minimizing $\mathbb{V}/\sqrt{\mathbb{E}}$. The optimization procedure yields an approximate value of $\alpha = 0.55$, with slight variations across features. The marginalized constraint on Σ_8 is shown in Figure 6.7 and Table 6.1 We clearly see that the κ power spectrum and the moments deliver a Σ_8 constraint consistent with the one from Planck [14]

Feature	$\Sigma_8 = \sigma_8 \Omega_m^{0.55}$
$P_{\kappa\kappa}(3)$	$0.84^{+0.06}_{-0.09}$
$P_{\kappa\kappa}(3)$ + Moments(9)	$0.86^{+0.02}_{-0.09}$
$V_0(10) + V_1(10) + V_2(10)$	$0.75^{+0.07}_{-0.04}$
$P_{\kappa\kappa}(3) + V_0(10) + V_1(10) + V_2(10)$	$0.76^{+0.04}_{-0.05}$
$P_{\kappa\kappa}(3) + V_0(10) + V_1(10) + V_2(10)$+ Moments(9)	$0.76^{+0.06}_{-0.04}$

Table 6.1: Tabulated values of 1σ constraints on Σ_8 from CFHTLenS using different features

(although with a larger error bar). The same conclusion does not hold for the Minkowski functionals, which seem to be affected by uncorrected systematics in the CFHTLenS catalogs to a greater extent than the power spectrum and the moments.

6.3.3 Dark Energy

Constraining on the physical nature of Dark Energy, unfortunately, is not possible using CFHTLenS data alone, mainly because of the small size of the survey. Looking at Figure 6.8, which shows constraints on Dark Energy equation of state w_0, we can conclude that the CFHT survey this parameter unconstrained. With bigger surveys coming up in the future one can hope to reduce statistical errors on feature measurements and to obtain smaller confidence contours as a consequence. Reduced statistical errors, on the other hand, require throughout knowledge of systematic effects, which have to be included in forward models in order to avoid bias in the parameters. The treatment of some of these systematic challenges will be the object of the next Chapter.

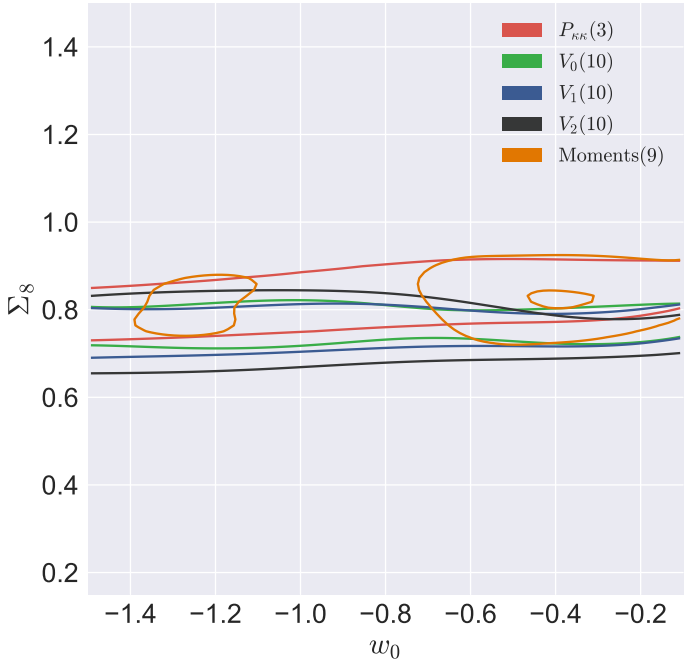

Figure 6.8: 1σ (68% confidence level) constraints on (w_0, Σ_8) from CFHTLenS using the κ power spectrum (red), Minkowski functionals (green, blue, black) and κ moments (orange). The number N_c of principal components is indicated in parentheses. The confidence contours are referred to the parameter likelihood $\mathcal{L}(\Omega_m, w_0, \Sigma_8)$ marginalized over Ω_m.

Chapter 7

Applications to the LSST survey: systematic challenges

In this Chapter we tackle some of the systematic issues that arise in a survey with large sky coverage such as LSST [3]. In the previous Chapter we saw that a small WL survey, such as CFHTLenS, leaves the Dark Energy equation of state w_0 essentially unconstrained. LSST covers an area of roughly $12,000\,\mathrm{deg}^2$, which is 100 times bigger than CFHTLenS. This can in principle lead to constraints on cosmology which are 10 times more precise. Increased precision, however, comes at a cost, because systematic effects that were negligible for CFHTLenS due to large statistical errors, may not be negligible anymore when compared to smaller cosmic variance fluctuations. We discuss a variety of systematic effects that can affect parameter estimates: we focus on atmospheric contaminations to the shear signal, sensor effects, and inaccuracies in photometric redshift estimation. We also study potential bias that can arise from approximate forward models based on the Born approximation. To conclude, we mention additional systematic effects which we did not have the chance to

investigate, and that we leave for future work.

7.1 Atmospheric/PSF spurious shear

The first systematic issue we investigate is the contamination of source galaxy shape measurements [20] due to the presence of the atmosphere. Before hitting the sensors on the telescope plate, photons travel through the Earth's atmosphere, which dilutes the WL signal by convolving it with a characteristic Point Spread Function (PSF). This effect can be better understood thinking about a point source, like a star: when observed on the telescope, this point source looks like an extended object, which traces the angular profile of the PSF. This contamination adds the instrumentation specific issues, such as the telescope's own PSF, tracking errors and photon shot noise. All these effects are modeled and simulated using the `phosim` software package [59]. We were provided with 20 independent realizations of a `phosim`–generated spurious shear catalog (see [60]) that contains information on 10^5 galaxies spread over a $4\,\mathrm{deg}^2$ field of view. The properties listed in the catalog include residual spurious shear measurements for each galaxy, after PSF corrections via a polynomial model subtraction were attempted [60]. The stochastic component of the residual shear decreases approximately as the inverse of the number of exposures of the field of view. The spatial patterns of the shear residuals in 4 of these realizations are shown in Figure 7.1. Angular correlations in the patterns seen in Figure 7.1 can be quantified in terms of the shear–shear two point correlation function

$$\xi^{+}_{\gamma\gamma}(\alpha) = \left\langle \gamma^1(\boldsymbol{\theta})\gamma^1(\boldsymbol{\theta}+\boldsymbol{\alpha}) + \gamma^2(\boldsymbol{\theta})\gamma^2(\boldsymbol{\theta}+\boldsymbol{\alpha}) \right\rangle , \tag{7.1.1}$$

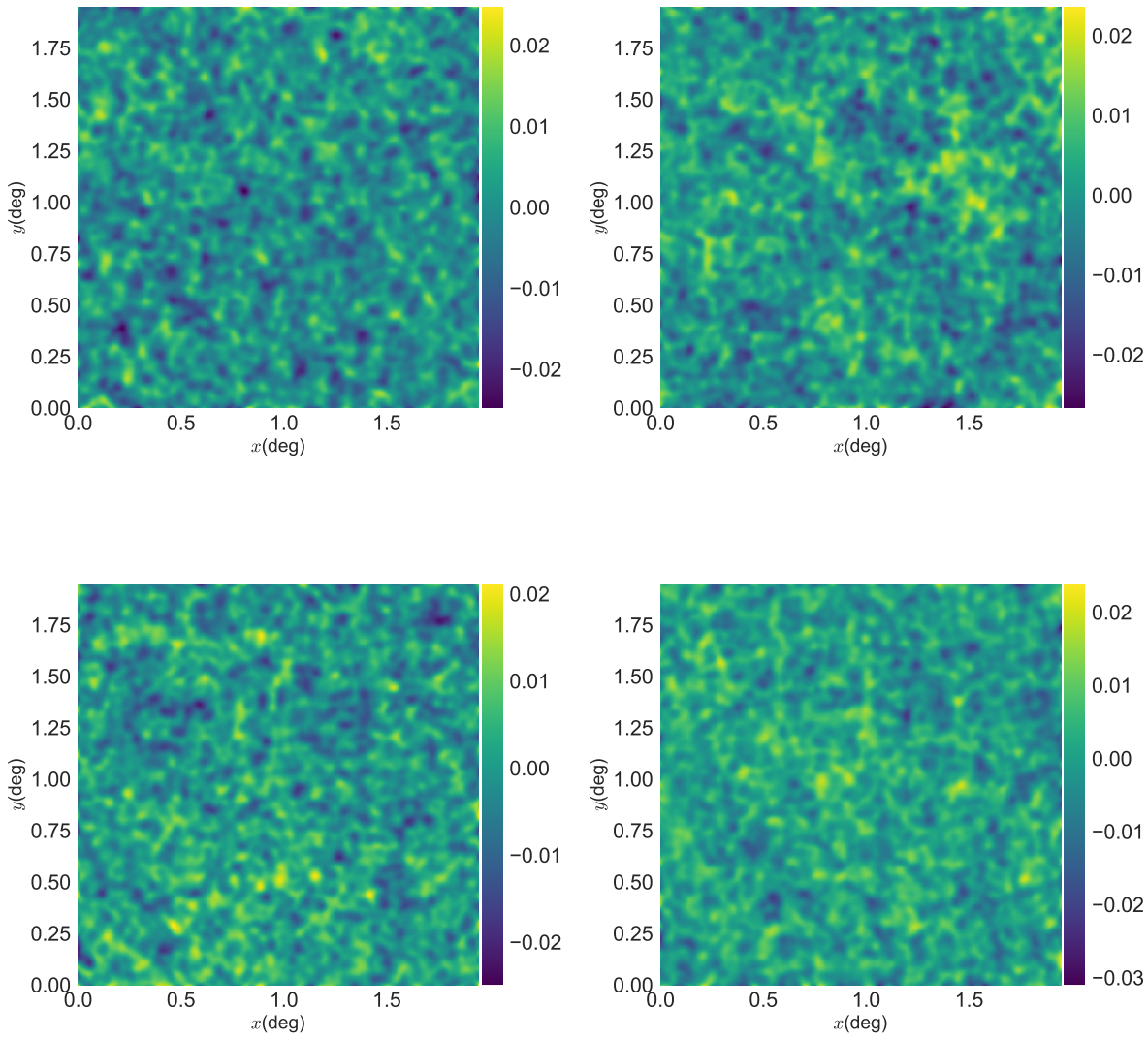

Figure 7.1: 4 independent realizations of the residual spurious κ after subtractions performed with polynomial fits to the PSF [60]. We show the reconstructed κ profiles obtained via the KS inversion procedure in (2.2.28). A Gaussian smoothing window with scale $\theta_G = 1'$ has been convolved with the images.

which is related to the spurious shear E and B mode power spectra as

$$\xi^{+}_{\gamma\gamma}(\alpha) = \int_0^\infty \frac{d\ell}{2\pi}\ell J_0(\ell\alpha)[S^{EE}(\ell) + S^{BB}(\ell)] \tag{7.1.2}$$

In equation (7.1.2), S^{EE} and S^{BB} refer to the power spectra of the E and B modes of the spurious shear, which defined in equation (2.2.29). J_0 is the 0–th order Bessel function of the first kind. A useful number to quote is the real space amplitude $\sigma_{\kappa,\mathrm{sp}}$ of the κ contamination induced by spurious shear, defined by

$$\sigma^2_{\kappa,\mathrm{sp}} = \int_0^\infty \frac{d\ell}{2\pi}\ell S^{EE}(\ell) \tag{7.1.3}$$

As we can see from Figure 7.2, we are allowed assume statistical isotropy assumption for this kind of contamination, as its power spectrum depends on $\ell = |\boldsymbol{\ell}|$ only. We also observe that, contrary to what happens for the WL signal, the magnitude of the spurious E and B mode auto power spectra is comparable. This property can be used as a flag for other kind of systematic effects that contribute to the observed shear with a large B mode. A popular model for the scale dependence of the residual spurious shear is encoded by a log–linear power spectrum [61]:

$$S^{EE}(\ell) = \frac{A}{\ell(\ell+1)}\left|1 + n\log\left(\frac{\ell}{\ell_0}\right)\right|, \tag{7.1.4}$$

where A, n, ℓ_0 refer to the spurious shear amplitude, spectral index and ℓ pivot point respectively. [61] employ such a model in order to forecast parameter bias caused by uncorrected spurious shear. Using the 20 spurious shear realizations we were provided with, we found that the log–linear model (7.1.4) for the residual shear is only correct for small ℓ

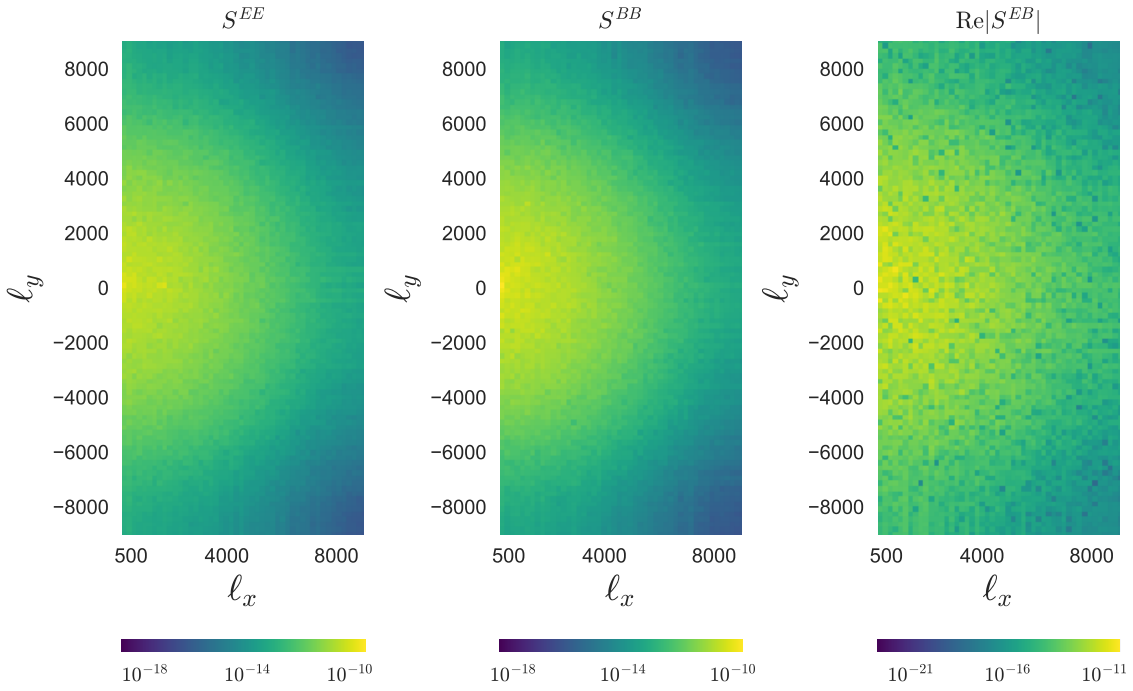

Figure 7.2: Two dimensional profiles of the power spectra measured from the spurious shear E (left panel) and B (middle panel) modes. We also measure the cross EB term $\langle\tilde{\gamma}^E\tilde{\gamma}^B\rangle$ (right panel). The quantities shown are the average of 20 independent residual spurious shear realizations. The statistical isotropy of the patterns is evident, as well as the fact that S^{EE} and S^{BB}, unlike the case for the WL signal, are comparable in magnitude.

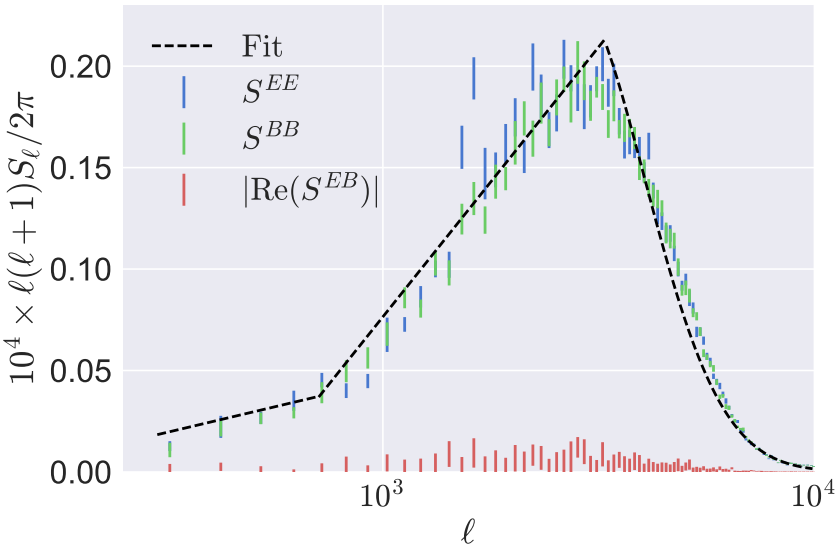

Figure 7.3: ℓ dependence of the residual spurious shear power spectra S^{EE} (blue), S^{BB} (green) and S^{EB} (red). The mid points and error bars refer respectively to the mean and standard deviation of the power spectra measured from the 20 spurious shear realizations. The dashed black line shows the best fit to the EE power spectrum performed with the empirical model in equation (7.1.5).

and breaks down on smaller scales [20] (probably due in part to the effect of smoothing), as can be seen in Figure 7.3. We propose the following alternative model for the spurious shear power spectrum. The model is piecewise log–linear but has an exponential damping at high ℓ, and provides a better fit to the instrument simulation than (7.1.4). We used the following empirical approximation

$$S^{EE}(\ell) = \begin{cases} \frac{A_0}{\ell(\ell+1)} \left|1 + n_0 \log\left(\frac{\ell}{\ell_0}\right)\right| & \text{if} \quad \ell \leq 700 \\ \frac{A_1}{\ell(\ell+1)} \left|1 + n_1 \log\left(\frac{\ell}{\ell_0}\right)\right| & \text{if} \quad 700 \leq \ell \leq 3300 \\ \frac{A_2 \log \ell}{\ell(\ell+1)} \exp\left[-b(\log \ell - \mu)^2\right] & \text{if} \quad \ell > 3300 \end{cases} \tag{7.1.5}$$

We fixed the pivot point to $\ell_0 = 700$ and we found the best fit parameters to the pattern seen in Figure 7.3 to be $(A_0, n_0, A_1, n_1, A_2, b, \mu) = (3.17 \cdot 10^{-5}, 1.36, 1.6 \cdot 10^{-4}, 7.54, 4.4 \cdot 10^{-5}, 15.37, 3.41)$. If we model the residual spurious shear as an additive contamination to the WL signal, using equation (5.1.7) we can evaluate the ΛCDM parameter bias that is induced by leaving this systematic effect uncorrected for. We generated Gaussian spurious shear κ mock images using the empirical model (7.1.5). The Fourier coefficients for the spurious κ maps were drawn from a normal distribution with zero mean and variance $S^{EE}(\ell)$. We added these spurious shear mock realizations on top of the WL signal maps (taken from the `IGS1` simulations, see Appendix), extracted the image features according to the procedures described in Chapter 4 and quantified parameter bias on the triplet $(\Omega_m, w_0, \sigma_8)$. The results are shown in Table 7.1. The calculations show that, under the assumption that source galaxies are positioned at a constant redshift $z_s = 2$, the effect of the spurious shear on cosmological constraints depends on the feature used in the analysis. Features that are polynomial in κ, such as the power spectrum and moments, deliver constraints which are essentially unbiased (for the study cases described in Table 7.1). The same conclusion is not true for features which probe the morphology of κ: constraints from Minkowski functionals are biased with a several σ significance, when spurious shear is left uncorrected for. The situation is not as dramatic for the peak counts constraint on σ_8, as the significance of the bias is below 1σ. When we look at the Ω_m and w_0 constraints, however, the bias can be as large as 2σ for the spurious shear modeled by the LSST instrument simulation. Because the direction of the bias depends on the particular feature considered, possibilities of self–calibration could be explored in the future.

Survey Assumptions

$z_s = 2$, $n_g = 15\,\text{galaxies/arcmin}^{-2}$, $\ell \in [100, 2 \cdot 10^4]$, $\kappa_{\rm MF} \in [-2\sigma, 2\sigma]$, $\kappa_{\rm pk} \in [-2\sigma, 5\sigma]$

Model	Ω_m	w_0	σ_8
		κ **power spectrum**	
Log–linear	$4.0 \cdot 10^{-6}$	$-2.69 \cdot 10^{-4}$	$2.5 \cdot 10^{-5}$
LSST simulation	$-6.22 \cdot 10^{-5}$	$2.94 \cdot 10^{-4}$	$1.32 \cdot 10^{-4}$
LSST simulation $\times 10$	$-7.51 \cdot 10^{-4}$	0.0025	0.0015
Error (1σ)	0.0015	0.01	0.0025
		Minkowski functionals	
Log–linear	0.0026	0.037	-0.0024
LSST simulation	0.0020	0.025	-0.0014
LSST simulation $\times 10$	0.007	0.055	-0.0068
Error (1σ)	0.001	0.005	0.0014
		κ **Moments**	
Log–linear	$-2.8 \cdot 10^{-5}$	-0.0011	$4.7 \cdot 10^{-5}$
LSST simulation	$1.09 \cdot 10^{-5}$	$-3.96 \cdot 10^{-4}$	$-7.60 \cdot 10^{-6}$
LSST simulation $\times 10$	$-2.84 \cdot 10^{-5}$	$-4.72 \cdot 10^{-3}$	$1.26 \cdot 10^{-4}$
Error (1σ)	0.0016	0.008	0.002
		Peak counts	
Log–linear	0.009	0.026	$3.2 \cdot 10^{-4}$
LSST simulation	0.0011	0.018	$2.9 \cdot 10^{-4}$
LSST simulation $\times 10$	0.0026	0.046	$4.0 \cdot 10^{-4}$
Error (1σ)	0.0011	0.0062	0.0015

Table 7.1: Bias on the parameter triplet $(\Omega_m, w_0, \sigma_8)$ calculated using three different models for the LSST spurious shear: *Log–linear* (first rows) refers to the log–linear model (7.1.4) with $(A, n, l_0) = (10^{-6.6}, 0.7, 700)$, with the normalization $\sigma^2_{\kappa,\rm sp} = 4 \times 10^{-7}$. *LSST simulation* (second rows) refers to the spurious shear mocks generated with the empirical model (7.1.5) (the amplitudes have been divided by a factor of $N_{\rm exposures} = 368$ to account for multiple field of view exposures), *LSST simulation* $\times$ *10* (third rows) refers to the same model but with the amplitude $\sigma^2_{\kappa,\rm sp}$ increased by a factor of 10. The 1σ error values (fourth rows) refer to the forecasts for an LSST–like survey obtained with equation (5.1.8).

7.2 CCD sensor effects

In this section we discuss issues that arise from imperfections in the sensors used to image source galaxies. Modern telescopes, such as LSST, use Charge–Coupled Devices (CCD) [62, 3, 59] as means to covert photon counts into voltage signals, which are then mapped into digitized images. Impurity gradients in the silicon, of which CCDs are made, cause the presence of spurious transverse electric fields, which displace the photons captured by the CCD. Such displacements lead to distortions in shape measurements, which in principle affect reconstructed WL fields. The astrometric displacement $\mathbf{d}_E$ due to the transverse electric fields is usually modeled as radial field [63] on the surface of the CCD according to

$$\mathbf{d}_E = d(r)\hat{\mathbf{r}} \tag{7.2.1}$$

At first order, this generates an additive contribution to the reconstructed κ field, which takes the name of *tree ring* effect. The induced contamination to the convergence, $\kappa_{\rm tree}$, can be calculated as (see [63])

$$\kappa_{\rm tree} = -\frac{1}{2}\nabla\cdot\mathbf{d}_E = -\frac{1}{2}\left(\frac{d(r)}{r} + \frac{d}{dr}d(r)\right). \tag{7.2.2}$$

A visualization of the tree ring effect is shown in the left panel of Figure 7.4. An additional source of contamination that derives from CCD manufacture imperfections has to do with the variable size of the CCD pixels. If the pixel area is not uniform across the CCD surface, variations in photon counts are erroneously interpreted as variations in the intensity profile of the source. This creates an additional source of error in the measurement of galaxy shapes. The typical spatial profile of the convergence contamination due pixel size varia-

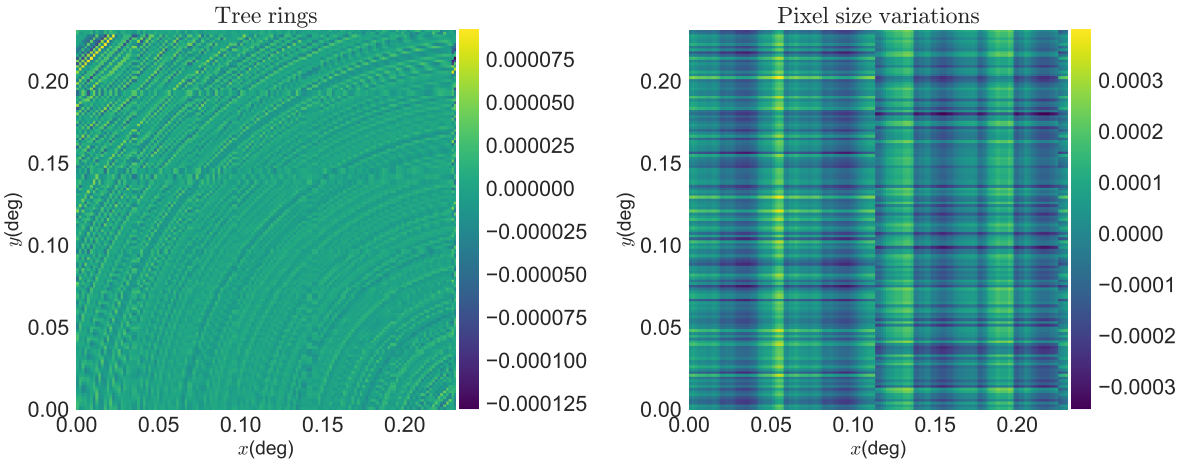

Figure 7.4: Spatial profiles of the additive contaminations to κ due to the tree ring (left) and pixel size variations (right) effects. The images cover a field of view of $(0.2\,\mathrm{deg})^2$. In order to extend the mapping of the systematics to the entire LSST field of view of $(3.5\,\mathrm{deg})^2$, we repeated the patterns seen in this Figure across the whole field of view, applying random 90° rotations at each replication.

tions, κ_{pixel}, is shown in the right panel of Figure 7.4. We remand the reader to [63] for a throughout discussion and modeling of the tree ring and pixel size variation effects. In order to evaluate the systematic effects on cosmological constraints, we make use of equation (5.1.7) and we use the κ power spectrum $P_{\kappa\kappa}$ as an image feature. The bias estimate $\hat{\mathbf{b}}$ in the parameters is calculated as

$$\hat{\mathbf{b}} = \hat{\mathbf{p}}_{\mathrm{sp}} - \hat{\mathbf{p}}_0 = \mathbf{Z}(\hat{\mathbf{d}}_{\mathrm{sp}} - \hat{\mathbf{d}}_0), \tag{7.2.3}$$

where we indicated the measured κ power spectra with and without CCD systematics present as $\hat{\mathbf{d}}_{\mathrm{sp}}$ and $\hat{\mathbf{d}}_0$ respectively. The $N_\pi \times N_d$ projection matrix $\mathbf{Z}$ is defined as

$$\mathbf{Z} = (\mathbf{M}^T\mathbf{\Psi}\mathbf{M})^{-1}\mathbf{M}^T\mathbf{\Psi}, \tag{7.2.4}$$

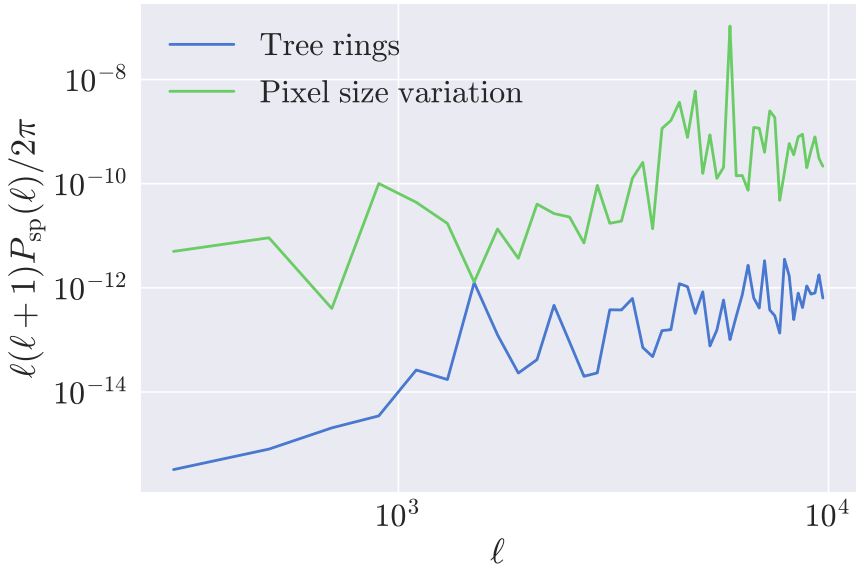

Figure 7.5: Power spectral density of the additive κ contamination due to the tree ring (blue) and pixel size variation (green) effects. The power spectra were measured from one realization of a $(3.5\,\mathrm{deg})^2$ field of view obtained repeating the patterns in Figure 7.4 with random 90° rotations.

following the notation of § 5.1.1, in which $\mathbf{M}, \mathbf{\Psi}$ are feature derivative with respect to cosmology and the inverse covariance matrix respectively. More explicitly, we write the power spectrum residuals as

$$\hat{P}_{\kappa\kappa+\mathrm{sp}}(\ell_b) - \hat{P}_{\kappa\kappa}(\ell_b) = \left| \frac{\hat{\tilde{\kappa}}(\ell_b) + \tilde{\kappa}_{\mathrm{sp}}(\ell_b)}{2\pi} \right|^2 - \hat{P}_{\kappa\kappa}(\ell_b) \tag{7.2.5}$$

In equation (7.2.5), the subscript i can either refer to the tree ring or pixel variation effect. Note that, contrary to $\hat{\tilde{\kappa}}$, the systematic contribution $\tilde{\kappa}_{\mathrm{sp}}$ is not a stochastic quantity, since it is tied to the field of view. The same is true for its angular power spectrum $P_{\kappa\kappa,\mathrm{sp}}$ (shown

in Figure 7.5). We express the estimator for the bias in the α–th cosmological parameter as

$$\hat{b}_\alpha = \sum_{\ell_b=\ell_{\min}}^{\ell_{\max}} Z_{\alpha\ell_b} \left(P_{\kappa\kappa,\mathrm{sp}}(\ell_b) + \frac{\hat{\tilde{\kappa}}(\ell_b)\tilde{\kappa}^*_{\mathrm{sp}}(\ell_b) + \hat{\tilde{\kappa}}^*(\ell_b)\tilde{\kappa}_{\mathrm{sp}}(\ell_b)}{(2\pi)^2} \right) \tag{7.2.6}$$

We assume a diagonal covariance matrix for the κ power spectrum, which is calculated according to (4.4.7):

$$C_{\ell_b\ell_{b'}} = \frac{P^2_{\kappa\kappa}(\ell_b)}{N_{\mathrm{modes}}(\ell_b)} \delta_{\ell_b\ell_{b'}}, \tag{7.2.7}$$

where $N_{\mathrm{modes}}(\ell_b)$ is the number of $\boldsymbol{\ell}$ modes that fall inside the Fourier annulus of radius ℓ_b. The value of $N_{\mathrm{modes}}(\ell_b)$ can be read off equation (4.4.7). Using the diagonal assumption, we can write down the expectation value $\mathbf{b}$ and scatter $\sigma_{\mathbf{b}}$ of the bias estimator (7.2.6) as

$$b_\alpha = \left\langle \hat{b}_\alpha \right\rangle = \sum_{\ell_b=\ell_{\min}}^{\ell_{\max}} Z_{\alpha\ell_b} P_{\mathrm{sp}}(\ell_b) \tag{7.2.8}$$

$$\sigma_{b_\alpha} = \sqrt{\left\langle \left(\hat{b}_\alpha - b_\alpha \right)^2 \right\rangle} = 2 \sum_{\ell_b=\ell_{\min}}^{\ell_{\max}} Z_{\alpha\ell_b} \sqrt{\frac{P_{\mathrm{sp}}(\ell_b) P_{\kappa\kappa}(\ell_b)}{N_{\mathrm{modes}}(\ell_b)}} \tag{7.2.9}$$

Note that, because of the nature of the bias estimator (7.2.6), the parameter bias induced by CCD effects has both a fixed component (7.2.8) proportional to P_{sp} and a stochastic component with a root mean square error (7.2.9), which scales as $\sqrt{P_{\mathrm{sp}}/N_{\mathrm{modes}}}$. Depending on the size of the survey, which sets the magnitude of $N_{\mathrm{modes}}(\ell_b)$, the fixed and stochastic components of the bias have different relative amplitudes because, while (7.2.9) decreases with the survey area, (7.2.8) does not. Table 7.2 shows the values of the bias components $\mathbf{b}, \sigma_{\mathbf{b}}$ for an LSST–like galaxy survey. Compared with the 1σ ΛCDM parameter errors shown in Table 7.1, we can safely conclude that the bias induced by this kind of CCD imperfections

Bias component	Ω_m	w_0	σ_8
Tree rings			
$\mathbf{b}$	$5.05 \cdot 10^{-10}$	$2.79 \cdot 10^{-9}$	$-3.52 \cdot 10^{-10}$
$\sigma_{\mathbf{b}}$	$6.92 \cdot 10^{-8}$	$1.34 \cdot 10^{-7}$	$1.29 \cdot 10^{-7}$
Pixel size variations			
$\mathbf{b}$	$1.21 \cdot 10^{-5}$	$-2.18 \cdot 10^{-5}$	$-1.79 \cdot 10^{-5}$
$\sigma_{\mathbf{b}}$	$1.21 \cdot 10^{-5}$	$3.37 \cdot 10^{-5}$	$1.82 \cdot 10^{-5}$

Table 7.2: Amplitudes for the fixed (7.2.8) and stochastic (7.2.9) components of the $(\Omega_m, w_0, \sigma_8)$ bias induced by the tree ring and pixel size variations effects resulting from CCD fabrication imperfections. The spurious contributions to κ were measured from a LSST instrument simulation [63], and the forward models necessary to obtain the WL $P_{\kappa\kappa}$ derivatives $\mathbf{M}$ and covariance matrix $\mathbf{C}$ were calculated with the analytical code `NICAEA` [38, 39]. The number N_{modes} of $\boldsymbol{\ell}$ modes which appears in equation (7.2.9) is referred to an LSST–like survey. Shape noise contributions for source galaxies placed at $z_s = 2$, with a galaxy density of $n_g = 15\,\mathrm{galaxies/arcmin}^2$, are included.

is negligible even for a survey with an area as wide as LSST. The bias is several order of magnitude smaller than the parameter uncertainty caused by cosmic variance.

7.3 Photometric redshift errors

In this section we study the effect of uncorrected redshift measurement errors on ΛCDM inferences. Photometric surveys, such as LSST, do not use full spectroscopic information in order to determine the redshift z_s of a source, but use a limited number of frequency bands (LSST uses 5 of them for example) to provide an estimate of z_s instead. This estimate is usually inaccurate [64]. We model the relation between the photometric and real redshift of a source galaxy as the sum of a fixed bias b_{ph} and a stochastic component of root mean square σ_{ph} [47, 64], according to

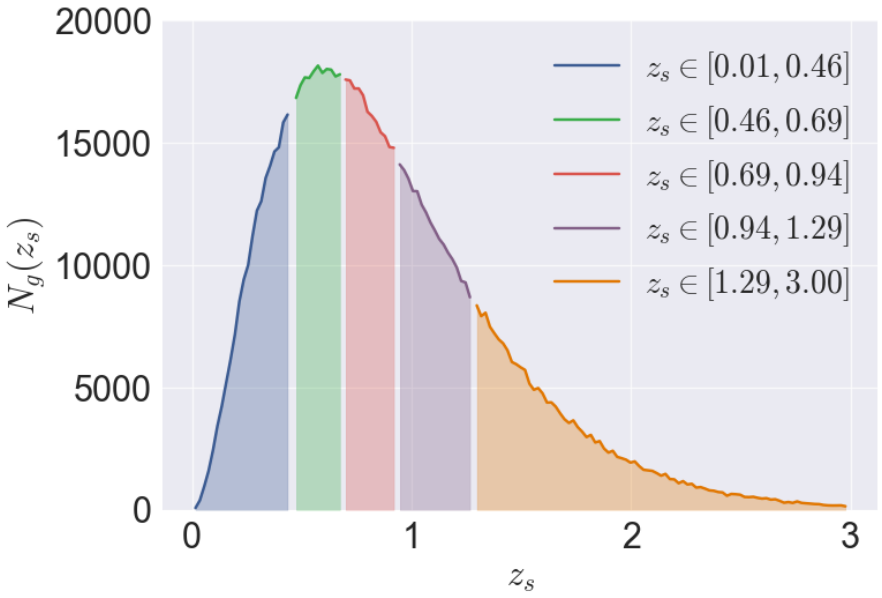

Figure 7.6: Redshift distribution of 10^6 source galaxies arranged uniformly in a $(3.5\,\mathrm{deg})^2$ field of view (which corresponds to a density of $n_g = 22\,\mathrm{galaxies/arcmin}^2$). The distribution follows the law $n(z_s) \propto (z_s/z_0)^2 \exp(-z_s/z_0)$ with $z_0 = 0.3$. For the purpose of this study (which makes use of the `LSST100Parameters` simulation suite, see Appendix) the galaxies have been divided in 5 redshift bins, chosen such that each bin contains the same number of galaxies.

$$z_{\mathrm{ph}}(z_s) = z_s + b_{\mathrm{ph}}(z_s) + \sigma_{\mathrm{ph}}(z_s)\mathcal{N}(0,1) \tag{7.3.1}$$

We chose the functional forms of the fixed and stochastic components following the LSST Science Book [64]:

$$b_{\mathrm{ph}}(z_s) = 0.003(1 + z_s) \tag{7.3.2}$$

$$\sigma_{\mathrm{ph}}(z_s) = 0.02(1 + z_s) \tag{7.3.3}$$

We simulated an LSST–like galaxy survey by drawing the redshift z_s of $N_g = 10^6$ source

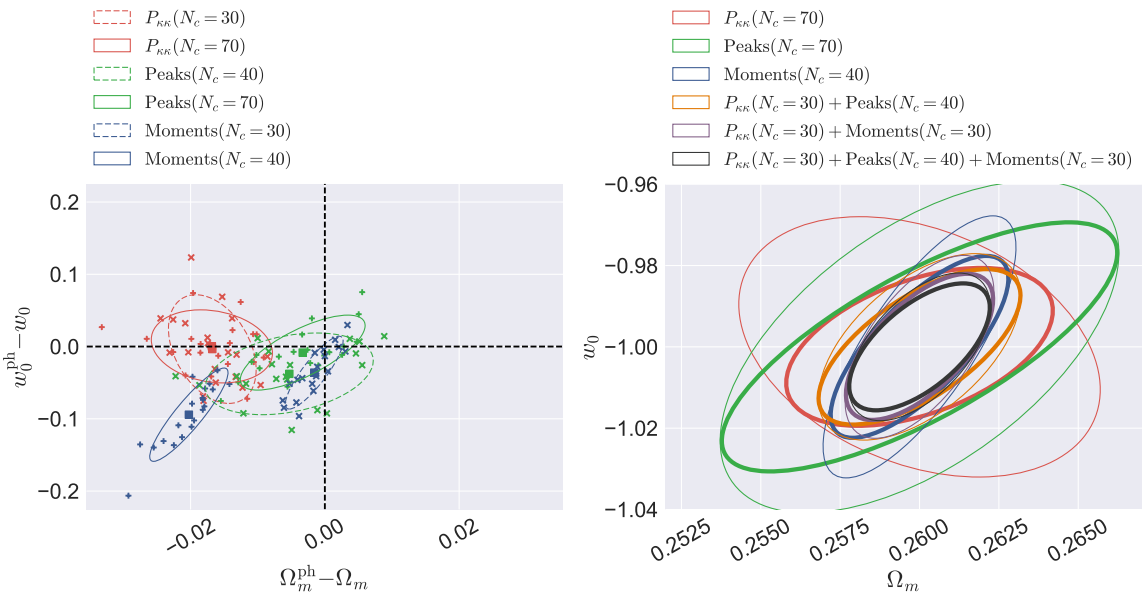

Figure 7.7: Left panel: bias on (Ω_m, w_0) induced by photometric redshift errors, obtained using the κ tomographic power spectrum (red), peak counts (green) and moments (blue). We show the bias values for 20 independent LSST–like survey realizations (crosses) and indicate the mean of $\hat{p}^{\rm ph} - \hat{p}$ as a square. For reference, we draw the 1σ (68% confidence level) ellipses on the bias $\hat{p}^{\rm ph} - \hat{p}$ assuming its distribution is Gaussian. Right panel: 1σ confidence ellipses on (Ω_m, w_0) obtained from tomographic features (color coded in the legend). We the constraints without (thin lines) and with (thick lines) Planck [14] priors included via equation (5.1.11). Feature covariance matrices have been measured from $N_r = 16,000$ realizations of the shear catalogs.

galaxies from the distribution in Figure 7.6. The galaxies are distributed uniformly in a $(3.5\,\mathrm{deg})^2$ field of view. Uncorrected photometric redshift errors can bias the constraints on cosmology when employing redshift tomography as a technique to map the WL feature space [65, 47] more in depth. If we assign the redshift $z_{\rm ph}$ to a galaxy which has a real redshift of z_s during the feature forward modeling process, we must consider the possibility that this forward model is wrong. To study the importance of this effect, we divided the source galaxies in $N_z = 5$ redshift bins and we used the `LensTools` functionality

ray–trace $\boldsymbol{\gamma}$ to the real redshift z_s of each galaxy. This operation produces multiple realizations (see § 3.2.3) for different ΛCDM cosmologies (we refer to this dataset as to the `LSST100Parameters` simulations). The shear catalogs are then converted into tomographic images via a binning procedure defined by

$$\boldsymbol{\gamma}(\boldsymbol{\theta}_p, \bar{z}_b) = \frac{\sum_{g=1}^{N_g} \boldsymbol{\gamma}(\boldsymbol{\theta}_g, z_g) W(\boldsymbol{\theta}_g, \boldsymbol{\theta}_p; z_g, \bar{z}_b)}{\sum_{g=1}^{N_g} W(\boldsymbol{\theta}_g, \boldsymbol{\theta}_p; z_g, \bar{z}_b)}. \tag{7.3.4}$$

In equation (7.3.4), $\boldsymbol{\theta}_g, z_g$ denote the galaxy position and redshift respectively and $\boldsymbol{\theta}_p, \bar{z}_b$ indicate the pixel position on the image and the center of the redshift bin (see Figure 7.6). We chose the window function W to be a top–hat:

$$W(\boldsymbol{\theta}_g, \boldsymbol{\theta}_p; z_g, \bar{z}_b) = \begin{cases} 1 \quad \text{if} \quad \boldsymbol{\theta}_g \in \boldsymbol{\theta}_p, z_g \in \bar{z}_b \\ \\ 0 \quad \text{otherwise.} \end{cases} \tag{7.3.5}$$

We then applied the KS inversion procedure (2.2.28) to each of the 5 $\boldsymbol{\gamma}(\boldsymbol{\theta}_p, \bar{z}_b)$ images to obtain the convergence field $\kappa(\boldsymbol{\theta}_p, \bar{z}_b)$ (a smoothing factor of $e^{-\ell^2\theta_G^2/2}$ with $\theta_G = 0.5'$ has been applied during the KS inversion for convenience). We extracted image features with the techniques described in Chapter 4, with the additional tomographic classification of the source galaxies in different redshift bins $\{\bar{z}_b\}$. We define the cross–redshift κ power spectrum $P_{\kappa\kappa}(\ell, \bar{z}_b, \bar{z}_{b'})$ as

$$\langle \tilde{\kappa}(\boldsymbol{\ell}, \bar{z}_b) \tilde{\kappa}(\boldsymbol{\ell}', \bar{z}_{b'}) \rangle = (2\pi)^2 \delta^D(\boldsymbol{\ell} + \boldsymbol{\ell}') P_{\kappa\kappa}(\ell, \bar{z}_b, \bar{z}_{b'}) \tag{7.3.6}$$

Note that, when introducing tomography, the dimensionality of the feature space N_d defined by $P_{\kappa\kappa}$ increases from N_d to $N_d N_z(N_z - 1)/2$. For higher order κ features, which are not quadratic in κ, we join the vectors $\mathbf{d}$ measured in different bins $\bar{z}_b$, increasing the

dimensionality of the feature space from N_d to $N_d N_z$. Dimensionality reduction techniques become especially relevant when considering tomographic features because, given the increased dimensionality, the constraint degradation pitfalls described in § 5.2 become important.

In order to study the effects of photometric redshift errors, we took the simulated shear catalogs in the fiducial cosmology and replaced each redshift z_s with an estimate $z_{\rm ph}$ based on photometry. The estimate was obtained using equation (7.3.1). We then performed a κ reconstruction with equation (7.3.4), we measured the features from the images and we inferred ΛCDM parameters using equations (5.1.7), (5.1.8). We quantified the bias induced on the inference on a parameter p by uncorrected photometric redshift errors as $\hat{p}^{\rm ph} - \hat{p}$, where $\hat{p}^{\rm ph}, \hat{p}$ denote parameter estimates from mock observations with and without redshift errors. We show the results in Figure 7.7. The plot shows that photometric redshift errors, if left uncorrected, cause significant bias in the parameters when using polynomial features such as the power spectrum and the moments of κ. Peak counts, on the other hand, are less affected by these systematics, likely because they probe correlations between shapes galaxy that are very close to each other on the sky. These correlations are affected to a lesser extent by photometric redshift errors, which are spatially uncorrelated. Since the bias for different features appears to point in different feature space directions, the possibility of self–calibration may be considered in the future.

The right panel of Figure 7.7 shows constraint forecasts on Ω_m and w_0 coming from WL tomography. The Figure shows that the combination of κ power spectrum, moments and peaks can in principle constrain w_0 to a percent level.

Solver	Runtime (1 FOV)	Memory usage	CPU time (1000 FOV)
Born	36.0 s	0.86 GB	10 hours
Full ray–tracing	124.8 s	1.65 GB	35 hours
Born + $O(\Phi^2)$	156.7 s	1.52 GB	44 hours

Table 7.3: CPU time and memory usage benchmarks for κ reconstruction. The test case we considered consists in a discretization with $N_l = 42$ uniformly spaced lenses between the observer and the sources at $z_s = 2$, each with a resolution of 4096^2 pixels. The κ field is resolved with 2048^2 light rays. We show both the runtime for producing a single field of view and the CPU hours needed to perform the reconstruction 1000 times, which is the amount of time needed to mock an LSST–like galaxy survey. Run times do not include the Poisson solution calculation, as this can be recycled to produce multiple field of view realizations (see § 3.2.3). The Poisson solution run time is negligible in the account of the total CPU time needed for the production of $N_r \gg N_l$ WL realizations.

7.4 Born approximation

In the previous sections we focused on the bias arising from observational systematics. In this section, on the other hand, we study a potential source of error due to the approximate theoretical modeling of WL features, namely the Born approximation. If one truncates the forward model for κ to first order in the gravitational potential Φ, equation (3.3.2) is sufficient for the calculation. The Born approximation is faster than exact ray–tracing (based on (3.2.17)) because the knowledge of the density contrast δ is sufficient for the computation. For full ray–tracing, on the other hand, Φ is necessary to compute the ray deflection angles and hence the solution to the Poisson equation (3.2.22) is needed. Table 7.3 (taken from [66]) shows that, using the `LensTools` implementation, one can save as much as a factor of 4 in CPU time when computing κ using the Born approximation. These time savings, however, come at a price since the forward model (5.1.5) and the matrix $\mathbf{M}$ are accurate only at $O(\Phi)$. When using approximate forward models to fit observations via (5.1.7), depending on the particular image feature used, one may induce bias in the inference of

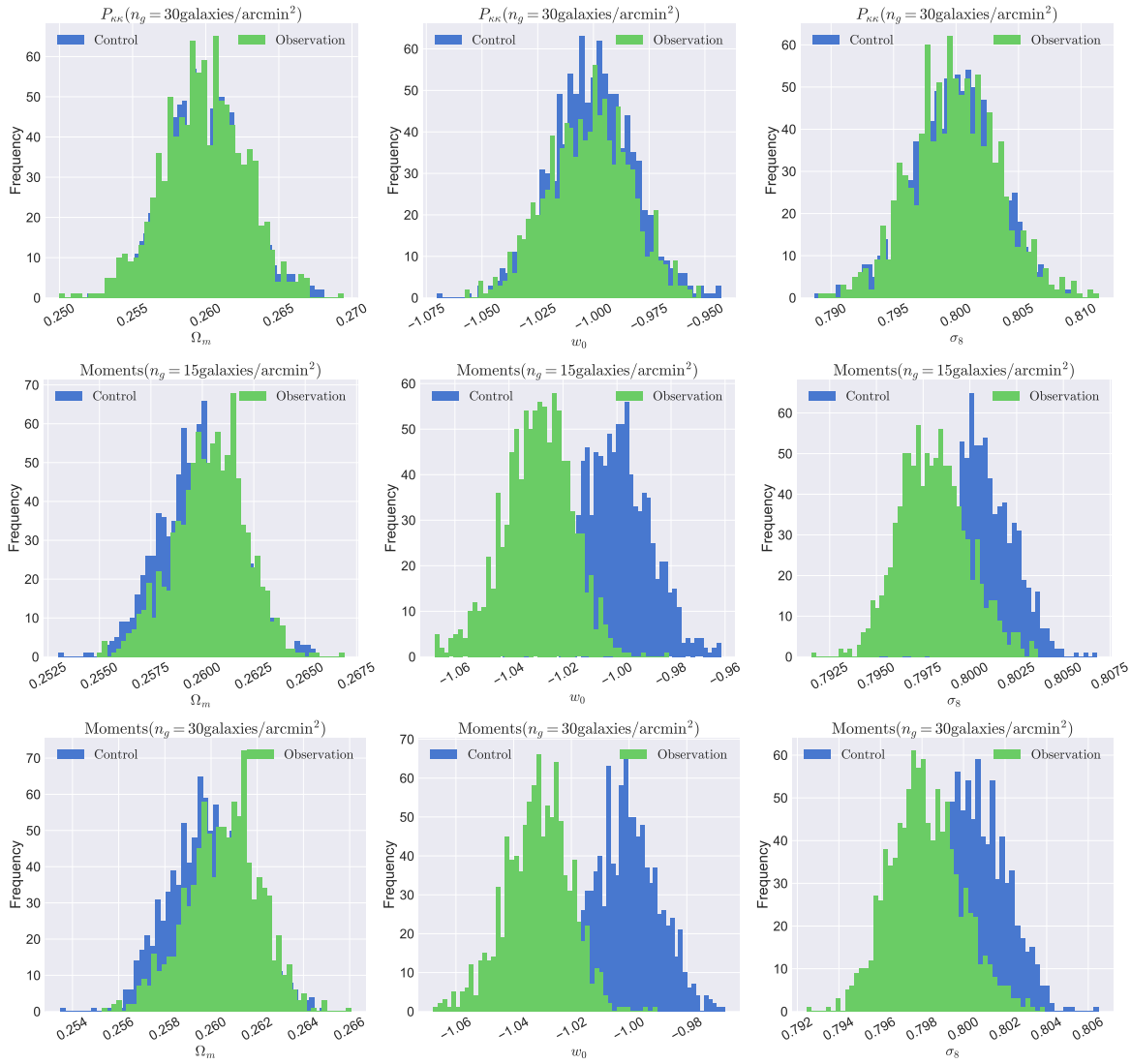

Figure 7.8: Distribution of parameter estimates for the triplet $(\Omega_m, w_0, \sigma_8)$, obtained with (5.1.7) using a variety of κ features which include the power spectrum and higher moments in real space. The observation to fit has been generated with full ray–tracing and the forward model, based on the feature derivatives $\mathbf{M}$, has been obtained with both the Born approximation (green bars), and exact ray–tracing (for the sake of null testing, blue bars). Forward models and covariance matrices have been estimated from ensembles of 8192 κ realizations, and mock measured features have been generated averaging over 1000 realizations, to mimic the area of an LSST–like survey. The $\hat{\mathbf{p}}_0$ samples were drawn with a bootstrapping procedure. The WL ensembles on which this study is based are taken from the `DEBatch` simulation suite (see Appendix).

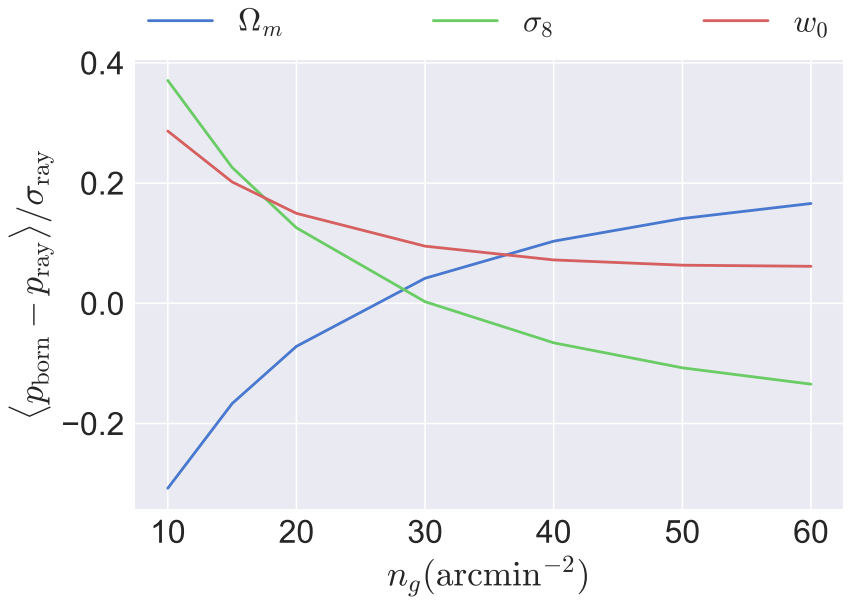

Figure 7.9: Statistical significance of the bias induced by the Born approximation on the Ω_m(blue), w_0(red) and σ_8 (green) inferences obtained from the κ power spectrum, as a function of the survey galaxy angular density n_g. The averaged results refer to an ensemble of 1000 bootstrapped realizations of an LSST–like galaxy survey.

parameters. This possibility was studied in [66], from which we take Figure 7.8. The plot shows the distribution of parameter estimates $\hat{\mathbf{p}}_0$ obtained with exact and Born approximated forward models. We can clearly see that inaccuracies due to the Born approximation do not lead to significant bias in the constraints obtained from the κ power spectrum. This conclusion is valid for an LSST like survey with a galaxy density of $30\,\mathrm{galaxies/arcmin}^2$ and holds for densities as high as $60\,\mathrm{galaxies/arcmin}^2$, as suggested by Figure 7.9. Figure 7.8 also shows that the Born approximation does not predict κ moments with sufficient accuracy, because the induced bias in w_0 and σ_8 is significant. The bias persists even when Gaussian shape noise is added to the images: higher κ moments are sensitive to non–Gaussian statistical information in the κ field, which has a distinct signature even when Gaussian shape noise is introduced. As we conclude in § 6.3.2, κ moments contain significant cosmological information. Because of this, in the analysis of a WL survey with the statistical power of LSST, the Born approximation does not predict κ higher moments to sufficient accuracy, and an exact approach based on ray–tracing is needed.

7.5 Other systematic effects

In this section we briefly overview some of the systematic effects that we did have the chance to investigate in this work, but that might be important for future analysis of WL observations. In § 7.2 we discussed how CCD imperfections generate spurious contributions to the convergence and we isolated two effects, the tree rings and the variations of pixel sizes, which have negligible impact on parameter inference. There is another effect which influences CCD operations and is worth mentioning: the so called *brighter–fatter* effect [67]. The response of CCD sensors to the flux of source galaxies is not linear: charge

accumulation on the surface of the CCD induces artificial distortions in the images, which have a net effect on the κ reconstruction procedure. These artificial deformations are more severe when observing brighter sources.

Another systematic effect worth mentioning has to do with the way one interprets the correlations between the shapes of nearby galaxies: κ is inferred with the KS inversion procedure (2.2.28) under the assumption that the ellipticity of the image is caused by cosmic shear. Intrinsic galaxy ellipticity is taken into account adding a white noise component to κ using equation (2.2.31). This treatment, however, completely ignores the fact that galaxies are partially aligned by the Large Scale Structure of the universe, and hence their shapes present *intrinsic alignments* (see [68] for a review on the effect). This alignment is usually modeled as an additive contribution $\boldsymbol{\gamma}^I$ to the WL shear but, contrary to shape noise, $\boldsymbol{\gamma}^I$ is spatially correlated. Analytical models for $\boldsymbol{\gamma}^I$ based on the tidal gravitational field have been explored in the literature [69]. The effect of ignoring intrinsic alignment on ΛCDM inferences using power spectra has also been explored by [70] and has been proven to be non negligible for large surveys such as LSST. The effects of intrinsic alignments hence need to be mitigated in order to avoid bias.

The last effect we mention in this section has to do with baryon effects. The κ forward modeling pipeline we made use of relies on Dark Matter only N–body simulations, which are relatively straightforward to run thanks to the collision–free nature of Dark Matter particles. In the real Universe, however, baryons with non zero pressure have non negligible effects on small scales. A variety of studies on the effects of baryon physics can be found in the literature. These include investigations of baryon physics on matter power spectra [71, 72], WL power spectra [73, 74], two and three–point shear statistics [75] and WL peak counts [76]. Forward modeling pipelines that include baryons add additional computational

complexity to the N–body simulations, as hydrodynamic approaches need do be adopted in order to model pressure effects correctly. Effects due to AGN and Supernovae feedback are currently under theoretical investigation and pose additional challenges.

Chapter 8

Conclusions

As a conclusion of this thesis, we give a summary the results we obtained and discuss possible future developments of cosmology with WL.

8.1 Overview of the results

8.1.1 Forward modeling

Inference of cosmological parameters from WL observations require a forward model that maps the ΛCDM parameter space onto the space of observations (or features). Although analytical forward models exist for the κ power spectrum [38, 39, 56], when considering higher order κ features one must rely on numerical simulations. In this work we presented a WL simulation pipeline which is capable of producing multiple realizations of κ images in a given cosmology. This pipeline (published in [24]), combined with image feature extraction techniques, provides the forward model capabilities needed in the analysis of WL observations.

8.1.2 Parameter constraints

The main goal of this thesis was to study the cosmological information carried by higher order κ features. We also wanted to see if this new information complements the one already supplied by the angular power spectrum. Although a precise quantification of the additional information depends on the details of the analysis such as the survey area, galaxy distribution in redshift and feature binning choices, we can safely conclude that the higher order statistics considered in this work contain a significant amount of information that quadratic κ descriptors ignore. We can see this in § 5.5 where we examine constraint forecasts on the $(\Omega_m, w_0, \sigma_8)$ parameter triplet: under the assumption that all source galaxies lie at a single redshift, higher κ moments, morphological descriptors and peak counts can deliver constraints which are 1.5 to 2 times tighter than the ones delivered by the power spectrum alone. When we use higher order features to constrain cosmology from CFHTLenS data in Chapter 6, we conclude that, although w_0 remains essentially unconstrained, κ moments deliver a constraint on (Ω_m, σ_8) which is much tighter than the one provided by the power spectrum alone. Although the CFHTLenS constraints obtained with the κ power spectrum and moments are compatible with the ones obtained with Planck, the same is not true for confidence intervals inferred with Minkowski functionals, which are affected by residual uncorrected systematics in the CFHTLenS data.

8.1.3 Noise in simulations

In this work we observed how higher order statistics tighten the constraints on ΛCDM parameters. Because forward modeling these statistics is done with the use of numerical simulations, sample variance is introduced in the models which are then used to fit the data.

We investigated this issue in Chapter 5, where we studied parameter error bar degradations due to noise in the covariance matrix. We verified that, when N_r realizations are used to estimate a $N_d \times N_d$ feature covariance matrix, error bars are enlarged by a factor which scales roughly as $1 + O(N_d/N_r)$, with $O((N_d/N_r)^2)$ terms becoming non–negligible for high N_d. We indicated dimensionality reduction techniques such as PCA as possible methods to make this issue less severe. We also found that only few N–body simulations with boxes of size $L_b = 240\,\mathrm{Mpc}/h$ (which is big enough to cover a $(3.5\,\mathrm{deg})^2$ field of view at $z_s = 2$) are needed for unbiased modeling of feature cosmic variance.

8.1.4 Weak Lensing systematics

In Chapter 7 we confirmed that a large survey such as LSST has the statistical power to constrain the Dark Energy equation of state w_0 to a percent level and hence has the potential to answer the long standing question whether w_0 is equal or not to -1. With this increased precision in measurements, though, stricter requirements on the accuracy of WL forward models must be enforced in order to avoid bias in parameter constraints. We studied different contamination sources to the WL signal and evaluated their effects on ΛCDM constraints. We found that, although CCD imperfections such as the tree ring effect and the variation of pixel sizes are a completely negligible effect, the same is not true for atmospheric spurious shear contaminations and photometric redshift errors. We found that, if left uncorrected, both of these systematic effects affect higher order κ features and lead to biases with a significance level bigger than 1σ. As a consequence, in upcoming galaxy surveys, these systematics must be either mitigated or modeled and marginalized over. We also concluded that, while the Born approximation is accurate enough to model the κ power spectrum, full ray–tracing needs to be employed for higher order κ moments.

8.2 Future prospects

8.2.1 Curse of dimensionality

Accurate detection of structures in feature space is crucial for obtaining better parameter constraints from WL. With the increased area and resolution of future surveys and with the advent of WL tomography, the typical dimensionality of the feature space is expected to increase significantly compared to previous generation experiments. Along with the possibility of tighter confidence intervals, this brings along a series of numerical challenges involved with high dimensionality, the most serious of which involves the estimation of feature covariance matrices. A possible solution to the constraint degradation described in § 5.2 is to reduce the dimensionality of the feature space while preserving the cosmological information contained in it. Although PCA offers a possibility in this sense, this is not the only way to go. Projections onto feature sub–spaces defined by orthonormal vectors (such as PCA) are not the most general. Non orthonormal projectors might be explored in the future as means of obtaining tighter constraints on ΛCDM. Moreover, physical insight in the Standard Model of cosmology could lead to scale invariant techniques for dimensionality reduction, thus removing the arbitrarity associated with feature whitening procedures. Another intriguing direction of investigation is to consider non linear techniques such as Locally Linear Embedding [46]. Although promising, these techniques require much bigger simulated datasets in order to be trained. Better estimators of the feature covariance matrix, which do not suffer from the numerical issues illustrated in § 5.2, can also be employed. Shrinkage [77] is one of such techniques, in which the specification of a theory–motivated target covariance leads to an estimator that, although slightly biased, degrades less severely with N_d.

8.2.2 Weak Lensing of the CMB

Background source galaxies are not only tracers of the WL effect: an intriguing possibility for an independent observable is the CMB [78]. Background photons that originate from the surface of last scattering situated at $z_* \approx 1100$ undergo lensing from Large Scale Structure as well. The primary CMB temperature anisotropy profile $T(\boldsymbol{\theta})$ is lensed by LSS, which yields a modified profile $T_{\rm lensed}(\boldsymbol{\theta})$. Lensing does not change the surface brightness of the sources, but only alters their shapes (see equation (2.2.4)). This consideration, applied to the CMB temperature profile, translates to

$$T_{\rm lensed}(\boldsymbol{\theta}) = T(\boldsymbol{\theta} + \nabla\psi_{\rm lens}(\boldsymbol{\theta})), \tag{8.2.1}$$

where the lensing potential $\psi_{\rm lens}$ is related to κ via the Poisson equation $\nabla^2\psi_{\rm lens} = -2\kappa$. Since the non–lensed CMB temperature T is a Gaussian field, spatial correlations that probe non–Gaussianities in $T_{\rm lensed}$ can be used to estimate κ [78, 79]. The same methods described in this work can then be used to extract features from the CMB–estimated κ and to infer ΛCDM parameters. CMB lensing provides a powerful probe for the Standard Model of cosmology when combined with galaxy lensing, because the systematic effects involved in the reconstruction of κ are independent in the two cases. [80] for example proposed a method for cross–correlating galaxy and CMB lensing observations in order to mitigate intrinsic alignment effects. Our `LensTools` pipeline can be adapted to study higher order image features and non–Gaussianities in CMB–reconstructed κ images (see [81] for a first application). Future prospects in this field include the study of the performance of the Born approximation in constructing CMB κ maps, both in feature accuracy [82, 83] and parameter constraints. Combination of galaxy and CMB lensing observations

have the potential of significantly improving constraints on the Dark Energy equation of state and on the neutrino masses.

Bibliography

[1] A. Friedman. Über die krümmung des raumes. *Zeitschrift für Physik*, 10(1):377–386, 1922.

[2] Scott Dodelson. 1 - the standard model and beyond. In Scott Dodelson, editor, *Modern Cosmology*, pages 1 – I. Academic Press, Burlington, 2003.

[3] LSST Dark Energy Science Collaboration. Large Synoptic Survey Telescope: Dark Energy Science Collaboration. *ArXiv e-prints*, November 2012.

[4] M. Levi, C. Bebek, T. Beers, R. Blum, R. Cahn, D. Eisenstein, B. Flaugher, K. Honscheid, R. Kron, O. Lahav, P. McDonald, N. Roe, D. Schlegel, and representing the DESI collaboration. The DESI Experiment, a whitepaper for Snowmass 2013. *ArXiv e-prints*, August 2013.

[5] E. V. Linder and A. Jenkins. Cosmic structure growth and dark energy. MNRAS, 346:573–583, December 2003.

[6] S. Perlmutter and B. P. Schmidt. Measuring Cosmology with Supernovae. In K. Weiler, editor, *Supernovae and Gamma-Ray Bursters*, volume 598 of *Lecture Notes in Physics, Berlin Springer Verlag*, pages 195–217, 2003.

[7] Scott Dodelson. 4 - the boltzmann equations. In Scott Dodelson, editor, *Modern Cosmology*, pages 84 – 116. Academic Press, Burlington, 2003.

[8] G. Chacón-Acosta, L. Dagdug, and H. A. Morales-Técotl. Manifestly covariant Jüttner distribution and equipartition theorem. Phys. Rev. E, 81(2):021126, February 2010.

[9] V. Springel. The cosmological simulation code GADGET-2. MNRAS, 364:1105–1134, December 2005.

[10] A. Cooray and R. Sheth. Halo models of large scale structure. Phys. Rep., 372:1–129, December 2002.

[11] Scott Dodelson. 5 - einstein equations. In Scott Dodelson, editor, *Modern Cosmology*, pages 117 – 138. Academic Press, Burlington, 2003.

[12] R. A. Vanderveld, R. R. Caldwell, and J. Rhodes. Second-order weak lensing from modified gravity. Phys. Rev. D, 84(12):123510, December 2011.

[13] A. R. Liddle. An Introduction to Cosmological Inflation. In A. Masiero, G. Senjanovic, and A. Smirnov, editors, *High Energy Physics and Cosmology, 1998 Summer School*, page 260, 1999.

[14] Planck Collaboration, P. A. R. Ade, N. Aghanim, M. Arnaud, M. Ashdown, J. Aumont, C. Baccigalupi, A. J. Banday, R. B. Barreiro, J. G. Bartlett, and et al. Planck 2015 results. XIII. Cosmological parameters. A&A, 594:A13, September 2016.

[15] Scott Dodelson. 10 - weak lensing and polarization. In Scott Dodelson, editor, *Modern Cosmology*, pages 292 – III. Academic Press, Burlington, 2003.

[16] B. M. Schäfer, L. Heisenberg, A. F. Kalovidouris, and D. J. Bacon. On the validity of the Born approximation for weak cosmic flexions. MNRAS, 420:455–467, February 2012.

[17] B. Jain, U. Seljak, and S. White. Ray-tracing Simulations of Weak Lensing by Large-Scale Structure. ApJ, 530:547–577, February 2000.

[18] S. Hilbert, J. Hartlap, S. D. M. White, and P. Schneider. Ray-tracing through the Millennium Simulation: Born corrections and lens-lens coupling in cosmic shear and galaxy-galaxy lensing. A&A, 499:31–43, May 2009.

[19] N. Kaiser and G. Squires. Mapping the dark matter with weak gravitational lensing. ApJ, 404:441–450, February 1993.

[20] A. Petri, M. May, Z. Haiman, and J. M. Kratochvil. Impact of spurious shear on cosmological parameter estimates from weak lensing observables. Phys. Rev. D, 90(12):123015, December 2014.

[21] Y.-S. Song and L. Knox. Determination of cosmological parameters from cosmic shear data. Phys. Rev. D, 70(6):063510, September 2004.

[22] M. White. The Zel'dovich approximation. MNRAS, 439:3630–3640, April 2014.

[23] Antony Lewis, Anthony Challinor, and Anthony Lasenby. Efficient computation of CMB anisotropies in closed FRW models. *Astrophys. J.*, 538:473–476, 2000.

[24] A. Petri. Mocking the weak lensing universe: The LensTools Python computing

package. *Astronomy and Computing*, 17:73–79, October 2016.

[25] Andrea Petri, Zoltán Haiman, and Morgan May. Sample variance in weak lensing: How many simulations are required? *Phys. Rev. D*, 93:063524, Mar 2016.

[26] Eric Jones, Travis Oliphant, Pearu Peterson, et al. SciPy: Open source scientific tools for Python, 2001–.

[27] Lisandro Dalcn, Rodrigo Paz, and Mario Storti. {MPI} for python. *Journal of Parallel and Distributed Computing*, 65(9):1108 – 1115, 2005.

[28] Message P Forum. Mpi: A message-passing interface standard. Technical report, Knoxville, TN, USA, 1994.

[29] Takahiko Matsubara. Statistics of smoothed cosmic fields in perturbation theory. i. formulation and useful formulae in second-order perturbation theory. *The Astrophysical Journal*, 584(1):1, 2003.

[30] H. Tomita. Curvature Invariants of Random Interface Generated by Gaussian Fields. *Progress of Theoretical Physics*, 76:952–955, October 1986.

[31] A. Petri, Z. Haiman, L. Hui, M. May, and J. M. Kratochvil. Cosmology with Minkowski functionals and moments of the weak lensing convergence field. Phys. Rev. D, 88(12):123002, December 2013.

[32] J. M. Kratochvil, E. A. Lim, S. Wang, Z. Haiman, M. May, and K. Huffenberger. Probing cosmology with weak lensing Minkowski functionals. Phys. Rev. D, 85(10):103513, May 2012.

[33] M. Shirasaki and N. Yoshida. Statistical and Systematic Errors in the Measurement of Weak-Lensing Minkowski Functionals: Application to the Canada-France-Hawaii Lensing Survey. ApJ, 786:43, May 2014.

[34] D. Munshi, L. van Waerbeke, J. Smidt, and P. Coles. From weak lensing to non-Gaussianity via Minkowski functionals. MNRAS, 419:536–555, January 2012.

[35] J. R. Bond and G. Efstathiou. The statistics of cosmic background radiation fluctuations. MNRAS, 226:655–687, June 1987.

[36] M. Sato, T. Hamana, R. Takahashi, M. Takada, N. Yoshida, T. Matsubara, and N. Sugiyama. Simulations of Wide-Field Weak Lensing Surveys. I. Basic Statistics and Non-Gaussian Effects. ApJ, 701:945–954, August 2009.

[37] E. Krause and C. M. Hirata. Weak lensing power spectra for precision cosmology.

Multiple-deflection, reduced shear, and lensing bias corrections. A&A, 523:A28, November 2010.

[38] M. Kilbinger, K. Benabed, J. Guy, P. Astier, I. Tereno, L. Fu, D. Wraith, J. Coupon, Y. Mellier, C. Balland, F. R. Bouchet, T. Hamana, D. Hardin, H. J. McCracken, R. Pain, N. Regnault, M. Schultheis, and H. Yahagi. Dark-energy constraints and correlations with systematics from CFHTLS weak lensing, SNLS supernovae Ia and WMAP5. A&A, 497:677–688, April 2009.

[39] M. Kilbinger, C. Heymans, M. Asgari, S. Joudaki, P. Schneider, P. Simon, L. Van Waerbeke, J. Harnois-Déraps, H. Hildebrandt, F. Köhlinger, K. Kuijken, and M. Viola. Precision calculations of the cosmic shear power spectrum projection. *ArXiv e-prints*, February 2017.

[40] D. Foreman-Mackey, D. W. Hogg, D. Lang, and J. Goodman. emcee: The mcmc hammer. *PASP*, 125:306–312, 2013.

[41] A. Taylor, B. Joachimi, and T. Kitching. Putting the precision in precision cosmology: How accurate should your data covariance matrix be? MNRAS, 432:1928–1946, July 2013.

[42] A. Taylor and B. Joachimi. Estimating cosmological parameter covariance. MNRAS, 442:2728–2738, August 2014.

[43] S. Matsumoto. General moments of the inverse real Wishart distribution and orthogonal Weingarten functions. *ArXiv e-prints*, April 2010.

[44] S. Dodelson and M. D. Schneider. The effect of covariance estimator error on cosmological parameter constraints. Phys. Rev. D, 88(6):063537, September 2013.

[45] L. Casarini, O. F. Piattella, S. A. Bonometto, and M. Mezzetti. Sample Variance in N-body Simulations and Impact on Tomographic Shear Predictions. ApJ, 812:16, October 2015.

[46] Ž. Ivezić, A.J. Connolly, J.T. Vanderplas, and A. Gray. *Statistics, Data Mining and Machine Learning in Astronomy*. Princeton University Press, 2014.

[47] A. Petri, M. May, and Z. Haiman. Cosmology with photometric weak lensing surveys: Constraints with redshift tomography of convergence peaks and moments. Phys. Rev. D, 94(6):063534, September 2016.

[48] C. Heymans, L. Van Waerbeke, L. Miller, T. Erben, H. Hildebrandt, H. Hoekstra, T. D. Kitching, Y. Mellier, P. Simon, C. Bonnett, J. Coupon, L. Fu, J. Harnois Déraps,

M. J. Hudson, M. Kilbinger, K. Kuijken, B. Rowe, T. Schrabback, E. Semboloni, E. van Uitert, S. Vafaei, and M. Velander. CFHTLenS: the Canada-France-Hawaii Telescope Lensing Survey. MNRAS, 427:146–166, November 2012.

[49] L. Miller, C. Heymans, T. D. Kitching, L. van Waerbeke, T. Erben, H. Hildebrandt, H. Hoekstra, Y. Mellier, B. T. P. Rowe, J. Coupon, J. P. Dietrich, L. Fu, J. Harnois-Déraps, M. J. Hudson, M. Kilbinger, K. Kuijken, T. Schrabback, E. Semboloni, S. Vafaei, and M. Velander. Bayesian galaxy shape measurement for weak lensing surveys - III. Application to the Canada-France-Hawaii Telescope Lensing Survey. MNRAS, 429:2858–2880, March 2013.

[50] M. Kilbinger, L. Fu, C. Heymans, F. Simpson, J. Benjamin, T. Erben, J. Harnois-Déraps, H. Hoekstra, H. Hildebrandt, T. D. Kitching, Y. Mellier, L. Miller, L. Van Waerbeke, K. Benabed, C. Bonnett, J. Coupon, M. J. Hudson, K. Kuijken, B. Rowe, T. Schrabback, E. Semboloni, S. Vafaei, and M. Velander. CFHTLenS: combined probe cosmological model comparison using 2D weak gravitational lensing. MNRAS, 430:2200–2220, April 2013.

[51] T. Erben, H. Hildebrandt, L. Miller, L. van Waerbeke, C. Heymans, H. Hoekstra, T. D. Kitching, Y. Mellier, J. Benjamin, C. Blake, C. Bonnett, O. Cordes, J. Coupon, L. Fu, R. Gavazzi, B. Gillis, E. Grocutt, S. D. J. Gwyn, K. Holhjem, M. J. Hudson, M. Kilbinger, K. Kuijken, M. Milkeraitis, B. T. P. Rowe, T. Schrabback, E. Semboloni, P. Simon, M. Smit, O. Toader, S. Vafaei, E. van Uitert, and M. Velander. CFHTLenS: the Canada-France-Hawaii Telescope Lensing Survey - imaging data and catalogue products. MNRAS, 433:2545–2563, August 2013.

[52] H. Hildebrandt, T. Erben, K. Kuijken, L. van Waerbeke, C. Heymans, J. Coupon, J. Benjamin, C. Bonnett, L. Fu, H. Hoekstra, T. D. Kitching, Y. Mellier, L. Miller, M. Velander, M. J. Hudson, B. T. P. Rowe, T. Schrabback, E. Semboloni, and N. Benítez. CFHTLenS: improving the quality of photometric redshifts with precision photometry. MNRAS, 421:2355–2367, April 2012.

[53] L. Fu, M. Kilbinger, T. Erben, C. Heymans, H. Hildebrandt, H. Hoekstra, T. D. Kitching, Y. Mellier, L. Miller, E. Semboloni, P. Simon, L. Van Waerbeke, J. Coupon, J. Harnois-Déraps, M. J. Hudson, K. Kuijken, B. Rowe, T. Schrabback, S. Vafaei, and M. Velander. CFHTLenS: cosmological constraints from a combination of cosmic shear two-point and three-point correlations. MNRAS, 441:2725–2743, July 2014.

[54] A. Petri, J. Liu, Z. Haiman, M. May, L. Hui, and J. M. Kratochvil. Emulating the CFHTLenS weak lensing data: Cosmological constraints from moments and Minkowski functionals. Phys. Rev. D, 91(10):103511, May 2015.

[55] J. Liu, A. Petri, Z. Haiman, L. Hui, J. M. Kratochvil, and M. May. Cosmology constraints from the weak lensing peak counts and the power spectrum in CFHTLenS data. Phys. Rev. D, 91(6):063507, March 2015.

[56] K. Heitmann, D. Higdon, M. White, S. Habib, B. J. Williams, E. Lawrence, and C. Wagner. The Coyote Universe. II. Cosmological Models and Precision Emulation of the Nonlinear Matter Power Spectrum. ApJ, 705:156–174, November 2009.

[57] Steven S. Skiena. *The Algorithm Design Manual*. Springer Publishing Company, Incorporated, 2nd edition, 2008.

[58] M. Takada and B. Jain. The kurtosis of the cosmic shear field. MNRAS, 337:875–894, December 2002.

[59] V. Krabbendam, S. Chandrasekharan, K. Cook, Z. Ivezic, R. L. Jones, K. S. Krughoff, M. Miller, C. Petry, P. A. Pinto, S. T. Ridgway, and A. Saha. LSST Operations Simulator. In *American Astronomical Society Meeting Abstracts #215*, volume 42 of *Bulletin of the American Astronomical Society*, page 401.05, January 2010.

[60] C. Chang, S. M. Kahn, J. G. Jernigan, J. R. Peterson, Y. AlSayyad, Z. Ahmad, J. Bankert, D. Bard, A. Connolly, R. R. Gibson, K. Gilmore, E. Grace, M. Hannel, M. A. Hodge, M. J. Jee, L. Jones, S. Krughoff, S. Lorenz, P. J. Marshall, S. Marshall, A. Meert, S. Nagarajan, E. Peng, A. P. Rasmussen, M. Shmakova, N. Sylvestre, N. Todd, and M. Young. Spurious shear in weak lensing with the Large Synoptic Survey Telescope. MNRAS, 428:2695–2713, January 2013.

[61] A. Amara and A. Réfrégier. Systematic bias in cosmic shear: extending the Fisher matrix. MNRAS, 391:228–236, November 2008.

[62] J.R. Janesick. *Scientific Charge-coupled Devices*. Press Monograph Series. Society of Photo Optical, 2001.

[63] Y. Okura, A. Petri, M. May, A. A. Plazas, and T. Tamagawa. Consequences of CCD Imperfections for Cosmology Determined by Weak Lensing Surveys: From Laboratory Measurements to Cosmological Parameter Bias. ApJ, 825:61, July 2016.

[64] LSST Science Collaboration, P. A. Abell, J. Allison, S. F. Anderson, J. R. Andrew, J. R. P. Angel, L. Armus, D. Arnett, S. J. Asztalos, T. S. Axelrod, and et al. LSST Science Book, Version 2.0. *ArXiv e-prints*, December 2009.

[65] D. Huterer, M. Takada, G. Bernstein, and B. Jain. Systematic errors in future weak-lensing surveys: requirements and prospects for self-calibration. MNRAS, 366:101–114, February 2006.

[66] A. Petri, Z. Haiman, and M. May. On the validity of the Born approximation for beyond-Gaussian weak lensing observables. *ArXiv e-prints*, December 2016.

[67] P. Antilogus, P. Astier, P. Doherty, A. Guyonnet, and N. Regnault. The brighter-fatter effect and pixel correlations in CCD sensors. *Journal of Instrumentation*, 9:C03048, March 2014.

[68] M. A. Troxel and M. Ishak. The intrinsic alignment of galaxies and its impact on weak gravitational lensing in an era of precision cosmology. Phys. Rep., 558:1–59, February 2015.

[69] J. Blazek, Z. Vlah, and U. Seljak. Tidal alignment of galaxies. *JCAP*, 8:015, August 2015.

[70] E. Krause, T. Eifler, and J. Blazek. The impact of intrinsic alignment on current and future cosmic shear surveys. MNRAS, 456:207–222, February 2016.

[71] Andrew R. Zentner, Douglas H. Rudd, and Wayne Hu. Self-calibration of tomographic weak lensing for the physics of baryons to constrain dark energy. *Phys. Rev. D*, 77:043507, Feb 2008.

[72] D. H. Rudd, A. R. Zentner, and A. V. Kravtsov. Effects of Baryons and Dissipation on the Matter Power Spectrum. ApJ, 672:19–32, January 2008.

[73] M. White. Baryons and weak lensing power spectra. *Astroparticle Physics*, 22:211–217, November 2004.

[74] H. Zhan and L. Knox. Effect of Hot Baryons on the Weak-Lensing Shear Power Spectrum. ApJ, 616:L75–L78, December 2004.

[75] E. Semboloni, H. Hoekstra, and J. Schaye. Effect of baryonic feedback on two- and three-point shear statistics: prospects for detection and improved modelling. MNRAS, 434:148–162, September 2013.

[76] X. Yang, J. M. Kratochvil, K. Huffenberger, Z. Haiman, and M. May. Baryon impact on weak lensing peaks and power spectrum: Low-bias statistics and self-calibration in future surveys. Phys. Rev. D, 87(2):023511, January 2013.

[77] A. C. Pope and I. Szapudi. Shrinkage estimation of the power spectrum covariance matrix. MNRAS, 389:766–774, September 2008.

[78] A. Lewis and A. Challinor. Weak gravitational lensing of the CMB. Phys. Rep., 429:1–65, June 2006.

[79] W. Hu and T. Okamoto. Mass Reconstruction with Cosmic Microwave Background Polarization. ApJ, 574:566–574, August 2002.

[80] M. A. Troxel and M. Ishak. Cross-correlation between cosmic microwave background lensing and galaxy intrinsic alignment as a contaminant to gravitational lensing cross-correlated probes of the Universe. Phys. Rev. D, 89(6):063528, March 2014.

[81] J. Liu, J. C. Hill, B. D. Sherwin, A. Petri, V. Böhm, and Z. Haiman. CMB lensing beyond the power spectrum: Cosmological constraints from the one-point probability distribution function and peak counts. Phys. Rev. D, 94(10):103501, November 2016.

[82] M. Calabrese, C. Carbone, G. Fabbian, M. Baldi, and C. Baccigalupi. Multiple lensing of the cosmic microwave background anisotropies. *JCAP*, 3:049, March 2015.

[83] G. Pratten and A. Lewis. Impact of post-Born lensing on the CMB. *JCAP*, 8:047, August 2016.

Appendix

Simulation sets used in this work

Table A.1 lists the WL simulation suites used in this work. The `IGS1` simulations have been generated with code written by Jan M. Kratochvil. `CFHTxxx` simulations have been generated by this research group with the ray–tracing code of Dr. Kratochvil. The remaining simulation sets have been generated with `LensTools`. The github links contain information about the simulation products. To retrieve such products the reader can email me at `ap3020@columbia.edu`.

Name	N_M	$L_b, N_p^{1/3}$	**Chapters**	**Publications**	**Link**
`IGS1`	9	240 Mpc$/h$,512	4,7	[31, 20, 32]	–
`CFHTemu1`	91	240 Mpc$/h$,512	6	[54, 55]	–
`CFHTcov`	1	240 Mpc$/h$,512	6	[54, 55]	–
`CovarianceBatch`	7	240 Mpc$/h$,512	5	[25]	github
`LSST100Parameters`	100	260 Mpc$/h$,512	5,7	[47]	github
`DEBatch`	7	260 Mpc$/h$,512	4,7	[66]	github

Table A.1: Simulation sets used in this work